RESONANT LIGHT-MATTER INTERACTION FOR ENHANCED CONTROL OF EXOTIC PROPAGATION OF LIGHT

BY

AKBAR SAFARI, PhD

A THESIS BY ARTICLES
SUBMITTED IN PARTIAL FULFILLMENT OF THE REQUIREMENTS FOR THE
DOCTORATE IN PHILOSOPHY DEGREE IN PHYSICS

Doctor of Philisophy (2019)	University of Ottawa
(Physics)	Ottawa, Ontario, Canada

TITLE:	Resonant Light-Matter Interaction for Enhanced Control of Exotic Propagation of Light
AUTHOR:	Akbar Safari PhD, University of Ottawa, Ottawa, ON, Canada
SUPERVISOR:	Dr. Robert W. Boyd

To Mobina,

for her endless support and encouragement

Abstract

We investigate the propagation of light in different conditions that lead to exotic propagation of photons and use near-resonant light-matter interactions to enhance these effects. First, we study the propagation of light in a moving highly dispersive medium, namely rubidium atoms. Based on the special relativity the speed of light changes with the speed of the medium. However, this drag effect in a non-dispersive medium is very small and thus difficult to measure. We show that the drag effect is enhanced significantly when the moving medium is highly dispersive. Thus, with this enhancement even a slow motion can be detected. Next, we employ the large nonlinear response of rubidium atoms to accentuate the formation of optical caustics. Caustics are important as nature uses caustics to concentrate the energy of waves. Moreover, caustics can be formed in many physical systems such as water waves in oceans to amplify tsunamis or generate rogue waves. The connection of our study to these giant water waves is discussed. Finally, we explore light-matter interactions in plasmonic systems. We show that photons experience a significant phase jump as they couple into and out of a plasmonic structure. This coupling phase, also known as the scattering phase shift, is generic to all scattering events. We measure this coupling phase with a triple-slit plasmonic structure. Moreover, we use the near-field enhancement of the plasmonic structure to enhance the coupling between the slits. Consequently, the photons can take non-trivial trajectories that pass through all three slits. We measure such exotic trajectories for the first time that are seemingly in violation of the superposition principle. The application of the superposition principle and the validity of Born's rule is discussed.

Acknowledgements

First, I would like to express my sincere gratitude to my supervisor Prof. Robert Boyd for providing me with this unique opportunity. Over the past five years, I have had the privilege of working alongside and learning from brilliant scientists; an opportunity made possible only because of you, Bob, and your drive and enthusiasm.

After I joined the CERC team, I converted from theory to experiment. Especial thanks to Israel De Leon for helping me with my first experiment, and thanks to Robert Fickler for his generous help. Also, credit goes to Filippo Miatto for being always available and eager to discuss physics, and to Jeremy Upham for his help and support. I would also like to thank the professors in the department, especially Jeff Lundeen and Gerd Leuchs from whom I learned a lot.

I enjoyed my years at uOttawa because of the wonderful community of people who made a friendly environment at work, especially my friends and colleagues with whom I interacted the most: Zahirul Alam, Enno Giese, Saumya Choudhary, Samuel Lemieux, Guillaume Thekkadath, Orad Reshef, Payman Rasekh, Boris Braverman, Hugo Begin, Gloria Kaneza and others I may have forgotten at this moment.

Last, and by no means least, I am incredibly grateful to my family whom I cannot acknowledge enough: my parents, for always understanding me; and my wife, Mobina - thank you for your love and dedication to our little family of three.

Contents

List of Figures

List of Tables

Chapter 1

Introduction

The propagation of light in different media and under different conditions has fascinated scientists for centuries. In the absence of a medium, photons are essentially noninteracting particles travelling at a constant speed of c. This is a desirable property for some applications such as communicating information. However, light-matter interaction is an integral part of nature and pervades a vast realm of physical phenomena from optics and atomic physics to condensed matter physics and astrophysics. In the presence of a strongly polarizable medium, photon-photon interaction is possible which facilitates information processing and computations with photons. The interaction of photons with a medium not only provides information about the nature of the interaction and the structure of the medium, but also provides the possibility to control the properties of the photons. For example, it has been established in the past couple of decades that it is possible to control the speed of propagation of a pulse of light in a medium to achieve speeds as slow as a few meters per second [1, 2, 3] or much faster than the speed of light in vacuum [4, 5, 6]. In addition, the propagation of light in a material system can be used to study and simulate other physical phenomena such as the event horizon of a black hole [7, 8], and the formation of giant waves in oceans [9].

In this article-based thesis, we consider a few applications of near-resonant light-matter interaction in two different systems: rubidium atomic vapour and plasmonic structures. The propagation of electromagnetic fields in plasmonic systems is well explained in many references, see for example Ref. [10], and different commercial packages are available for numerical simulation of plasmonic systems. In contrast, the light-matter interaction in atomic vapour is more involved. Although the principles are explained in great detail in numerous textbooks, calculation of the optical response of the atoms requires careful attention to the different conventions and definitions that may have been used in difference references. Therefore, in the remainder of this chapter we briefly explain how we calculate the optical response of rubidium atoms. Interested readers can refer to the references for more theoretical details.

Chapter 2 describes how we enhance the light-drag effect by moving highly dispersive atomic vapours. This experiment was in fact a repetition of the seminal work by Fizeau in 1850, but performed with atomic vapours as the moving medium instead of water. Fizeau's experiment influenced Einstein the most in his theory of special relativity. Peter Zeeman repeated the experiment with moving glass rods and flowing water. He also anticipated that the effect can be enhanced by using alkali vapours. However, the expected results were never observed. We show that the change in the speed of light inside a moving highly dispersive rubidium vapour is proportional to the group index of the medium, in great agreement with the theoretical prediction.

In Chapter 3 we report the first observation of caustics formed from a nonlinear phase shift. Caustics involve an important type of singularity, a ray catastrophe, in which the rays become infinitely intense. We employ rubidium atomic vapour as the nonlinear medium in which the nonlinear Schrödinger equation governs the propagation of the electromagnetic wave. Remarkably, the same theoretical framework is used to describe the nonlinear propagation of water waves in oceans. Therefore, our results are also helpful to understand the formation of caustics in ocean waves which can amplify tsunamis or generate rogue waves in oceans.

Chapter 4 describes the exotic trajectories of photons in a triple-slit structure imposed by the near-field enhancement of a plasmonic system. We show that photons can take looped trajectories that pass through all the three slits. It was postulated that such trajectories might violate Born's rule, one of the main axioms of quantum mechanics. Therefore, the application of the superposition principle and the validity of Born's rule is discussed.

In Chapter 5 we show that photons experience a phase jump as they couple in and out of a plasmonic structure. We measure this phase jump by incorporating the unique interference pattern of a triple-slit geometry on a plasmonic layer. We model each plasmonic slit as a tritter, i.e. a beamsplitter with three input and three output ports, and infer the coupling phase from our simple and accurate theoretical model. This coupling phase, also known as the scattering phase shift, is intrinsic to any scattering phenomena. Therefore, our approach provides a simple method to characterize this scattering phase and its dependence on different parameters.

In the appendix we present a side project that is not part of the main body of the thesis. This theoretical work studies the photon number discrimination with Baysian analysis. We use spatial demultiplexing of photons to split them into multiple channels with on/off detectors and arrive at an explicit formula for the number of photons in terms of the number of counts. Our analysis takes into account the dark counts due to noise, quantum efficiency less than unity, and also the probability of coincidence where more than one photon falls on the same detector. We discuss a few examples for the application of our method.

1.1 Rubidium atoms

Alkali metals in the first group of the periodic table have the simplest structure of all atoms. They have been studied very well and their properties can be calculated either analytically or numerically with an extremely high precision. In the solid phase, alkali metals have the simplest band structure and the Drude-Sommerfeld model is adequate to explain the majority of their electronic properties [11]. In the gas phase, alkali atoms are widely used for fundamental studies and precision measurements. For example, the unit of time is defined in terms of a transition frequency in atomic cesium. Moreover, alkali atoms were the first ones to be cooled and trapped [12]. Warm atomic vapours, in particular rubidium atoms, are used extensively for multiple reasons. Most important is that the excitation frequency from the lowest energy level to the first excited state lies in the visible region for which narrowband tunable diode lasers are available. Another reason for their popularity is their large vapour pressure at a modest temperature close to the room temperature. Therefore, it is not surprising that the main body of most textbooks in atomic physics and solid state physics is devoted to the elements in the first group of the periodic table.

Atomic vapours have a narrow transition line and can couple to resonant photons very efficiently. This has been employed, for example, to control the group velocity of a pulse of light and achieve velocities less than 100 m/s [2], or even stop the photons completely [13, 14, 15]. Moreover, atomic vapours are easy to saturate. Therefore, they exhibit an extremely large nonlinear effects such as the optical Kerr effect [1, 16, 17] or third harmonic generation [18].

1.2 Atomic structure of rubidium

1.2.1 Gross energy levels

Rubidium (Rb) comes next to krypton (Kr) in the periodic table with ground state electronic configuration [Kr]$5s^1$. The valence electron in the $5s$ orbital is the only electron participating in most interactions and the other 36 electrons form a closed shell around the nucleus. Hence, Rb is a hydrogen-like atom and the valence electron experiences a central potential. In a central potential proportional to $1/r$, there is an accidental degeneracy where the gross energy of the electron is independent of its orbital angular momentum (L). In this case, the s and p orbitals would have the same energy. However, this degeneracy is broken in alkali atoms due to the quantum defect; the wavefunction of the s electrons penetrates through the shell and has a significant overlap with the wavefunction of the core. Therefore, the $5s$ level has a lower energy than $5p$ in Rb. A widely used empirical formula to find the gross energy levels of alkalis is a modified form of Bohr's formula [19]

$$E(n,l) = -\frac{e^2}{8\pi\epsilon_0 a_0}\frac{1}{(n-\eta)^2}, \tag{1.1}$$

where a_0 is the Bohr radius, and the quantum defect η is subtracted from the principal quantum number n. The quantum defect depends on the principal quantum number and the orbital angular momentum L as can be seen from the Rydberg-Ritz formula [20]

$$\eta = \alpha(L) + \frac{\beta(L)}{n^2}. \tag{1.2}$$

Table 1.1 lists the values of the quantum defect for a few low-lying energy levels of Rb atoms. The transitions from the ground state $5S_{1/2}$ to the excited states $5P_{1/2}$ and $5P_{3/2}$ are called D_1 and D_2 lines, respectively. Using Eq. (1.1) and Table 1.1

the transition wavelengths are calculated to be 792 nm and 777 nm for the D_1 and D_2 transitions, which are close to the experimentally measured wavelengths of 795 nm and 780 nm, respectively. Note that the effect of spin-orbit interaction which further affects the excited states $5P_{1/2}$ and $5P_{3/2}$ is not included yet. Also note that without the quantum defect, there would be no D_1 or D_2 transition in alkali atoms.

1.2.2 Fine and hyperfine structures

The valence electron carries a spin angular momentum $\boldsymbol{S}$ and an orbital angular momentum $\boldsymbol{L}$. The total angular momentum of the electron is then given by $\boldsymbol{J} = \boldsymbol{L} + \boldsymbol{S}$ which can take the quantized values in the range $| L - S |\leq J \leq L + S$. The electron in the ground state ($S-$term) is characterized by $S = 1/2$ and $L = 0$, thus $J = 1/2$. The electron in the excited state ($P-$term) carries $L = 1$ and thus J can take two values of $1/2$ and $3/2$. We denote these energy levels with the spectroscopic notation

$$n^{(2S+1)}L_J \tag{1.3}$$

where L is a letter from the list S, P, D, F, $\cdots$, corresponding to the orbital angular momentum of L =0, 1, 2, 3, $\cdots$, respectively. Since Rb has a single valence electron, the spin multiplicity is always $2S$+1=2, and we drop that from

TABLE 1.1: Quantum defect η of a few low-lying energy levels of Rb, taken from Ref. [20]. Note that as the energy of a level increases, its quantum defect decreases.

$S-$terms	η	$P-$terms	η
$5S$	3.195	$5P_{1/2}$	2.720
		$5P_{3/2}$	2.707
$6S$	3.154	$6P_{1/2}$	2.683
		$6P_{3/2}$	2.669

our notation.

The most important interaction, after the effect of quantum defect discussed in the previous section, that shifts the energy levels of Rb atoms and leads to the fine structure is the spin-orbit interaction. This can be understood simply as the interaction between the magnetic dipole moment associated to the spin of the electron and the magnetic field generated by the orbital angular momentum of the electron. Therefore, the energy shift can be calculated from the interaction Hamiltonian $H_{so} = C\boldsymbol{L}.\boldsymbol{S}$. Evaluating the constant C requires the knowledge about the radial part of the electronic wavefunction which demands extensive numerical calculations. However, an empirical formula by Landé predicts that the spin-orbit interaction scales as Z^2 with Z being the atomic number. This explains why the D_1 and D_2 spectral lines are well separated in Rb (795 nm and 780 nm) and even more in cesium (894 nm and 852 nm).

In analogy to the spin of the electron, the nucleus of the atom also carries an angular momentum $\boldsymbol{I}$. Similar to the spin-orbit interaction, the angular momentum of the nucleus interacts with the total angular momentum of the electron and results in the hyperfine splitting of the energy levels. The Hamiltonian of this interaction can be written as $H_{hf} = \frac{A}{\hbar^2}\boldsymbol{I}.\boldsymbol{J}$, where A is a constant that depends on the electron wavefunction at the position of the nucleus. The total angular momentum of the atom is given by $\boldsymbol{F} = \boldsymbol{I} + \boldsymbol{J}$. Therefore, using the fact that the magnitude of an arbitrary angular momentum $\boldsymbol{K}$ is $\hbar\sqrt{K(K+1)}$, the expectation value of the hyperfine interaction can be expressed as

$$\begin{aligned} E_{hf} &= \frac{A}{\hbar^2}\left\langle \boldsymbol{I}.\boldsymbol{J} \right\rangle = \frac{A}{2\hbar^2}\left\langle \boldsymbol{F}^2 - \boldsymbol{I}^2 - \boldsymbol{J}^2 \right\rangle \\ &= \frac{A}{2}\{F(F+1) - I(I+1) - J(J+1)\}. \end{aligned} \tag{1.4}$$

Natural rubidium consists of two isotopes with mass numbers 85 and 87 with

Table 1.2: Magnetic dipole constant A used in Eq. (1.4) to calculate the hyperfine splitting for different levels of ^{85}Rb and ^{87}Rb (taken from Refs. [23, 24, 25]).

^{85}Rb levels	A	^{87}Rb levels	A
$5S_{1/2}$	$h \times 1011\,\mathrm{MHz}$	$5S_{1/2}$	$h \times 3417\,\mathrm{MHz}$
$5P_{1/2}$	$h \times 120.5\,\mathrm{MHz}$	$5P_{1/2}$	$h \times 406.2\,\mathrm{MHz}$
$5P_{3/2}$	$h \times 25.0\,\mathrm{MHz}$	$5P_{3/2}$	$h \times 84.8\,\mathrm{MHz}$

abundances 72.17% and 27.83%, respectively. The two isotopes have different hyperfine structures mainly due to the different nuclear angular momentum that they possess. The nuclear spin angular momentum of ^{85}Rb and ^{87}Rb are $I = 5/2$ and $I = 3/2$, respectively. The constant A for a few levels of both isotopes are listed in Table 1.2. The experimentally measured energy levels for ^{85}Rb and ^{87}Rb are sketched in Fig. 1.1. The hyperfine intervals from Eq. (1.4) fall within 5% accuracy of the experimental data shown in Fig. 1.1. For a more accurate theoretical approach, one has to include the higher order effects such as the electric quadrupole hyperfine interaction, isotope shift, etc [19, 21, 22].

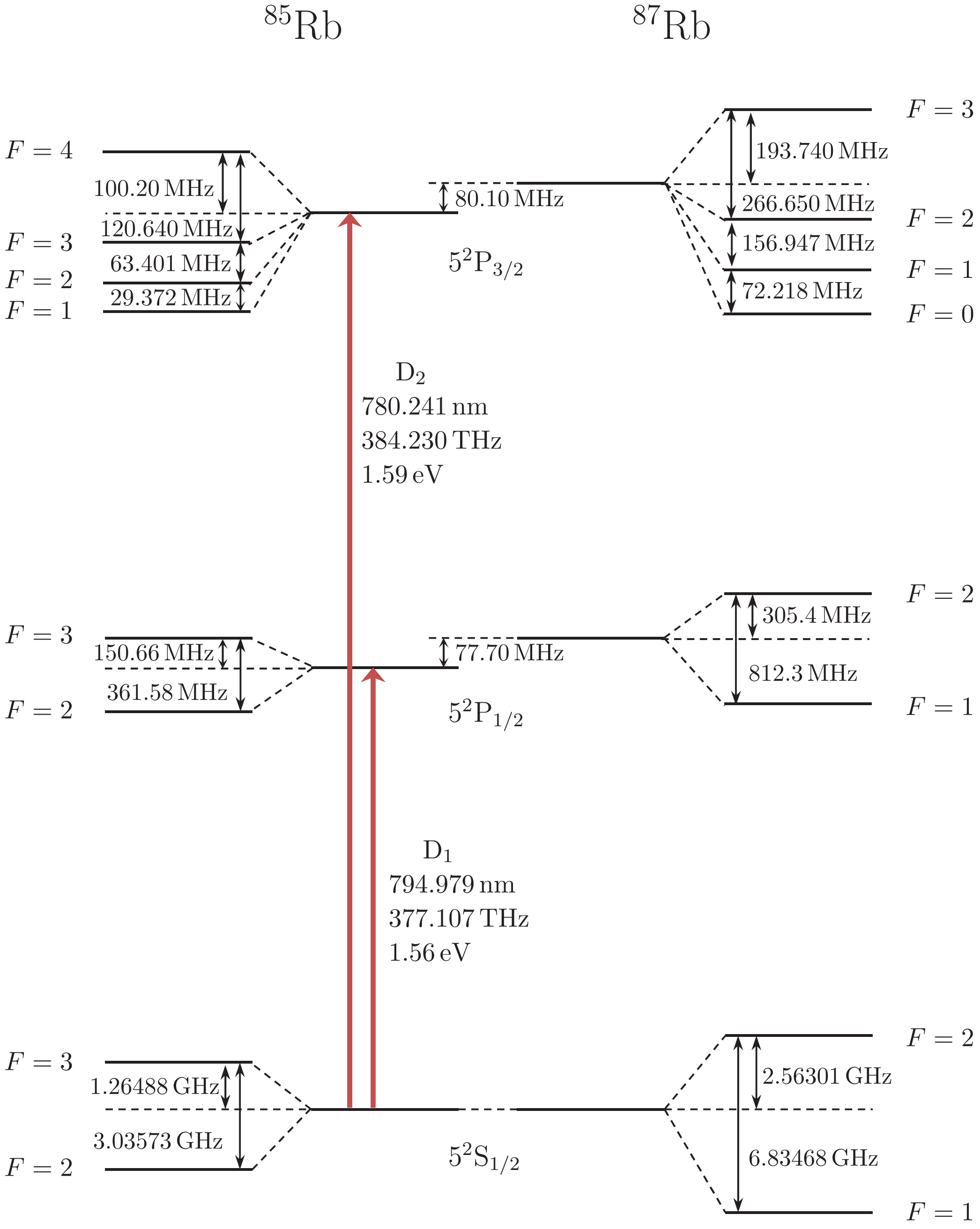

FIGURE 1.1: Hyperfine structure of ^{85}Rb and ^{87}Rb for the D_1 and D_2 transition lines from Refs. [23, 24, 25]

1.3 Light-matter interaction in Rb

Optical susceptibility of Rb atoms can be found from the density matrix approach. Although, as shown in the previous section, Rb atoms contain many different energy levels, a two-level system approximation is good enough to derive many of the optical properties of the atoms. In a two-level system, an external electromagnetic field can place the atoms in a superposition of the two levels

$$|\Psi\rangle = c_1 |g\rangle + c_2 |e\rangle , \tag{1.5}$$

where $|g\rangle$ and $|e\rangle$ are the ground and the excited states of the atom, respectively. Therefore, the density matrix is expressed as

$$\rho = \begin{pmatrix} \left\langle |c_1|^2 \right\rangle & \langle c_1 c_2^* \rangle \\ \langle c_1^* c_2 \rangle & \left\langle |c_2|^2 \right\rangle \end{pmatrix} . \tag{1.6}$$

The symbol $\langle \ldots \rangle$ indicates the average value for the ensemble. The Hamiltonian of the system can be written as $H = H_0 + V(t)$, where H_0 is the atomic Hamiltonian and $V(t)$ is the perturbation due to the light-matter interaction. In the semi-classical approach and within the electric dipole approximation, the perturbation is given by

$$V(t) = -\boldsymbol{\mu} . \boldsymbol{E}(t), \tag{1.7}$$

where $\boldsymbol{\mu} = -e\boldsymbol{r}$ is the electric dipole moment, and $\boldsymbol{E}(t)$ is the electric field of the applied laser light. Using the Heisenberg equation of motion $\dot{\rho} = -\frac{i}{\hbar}[H, \rho]$, we arrive at the following equations for the time evolution of the elements of the density matrix [26]

$$\dot{\rho}_{eg} = -\left(i\omega_0 + \frac{1}{T_2}\right)\rho_{eg} + \frac{i}{\hbar}V_{eg}(\rho_{ee} - \rho_{gg}), \tag{1.8}$$

$$\dot{\rho}_{ee} = -\frac{\rho_{ee}}{T_1} - \frac{i}{\hbar}(V_{eg}\rho_{ge} - \rho_{eg}V_{ge}), \tag{1.9}$$

$$\dot{\rho}_{gg} = \frac{\rho_{ee}}{T_1} + \frac{i}{\hbar}(V_{eg}\rho_{ge} - \rho_{eg}V_{ge}). \tag{1.10}$$

Here, ω_0 is the resonant frequency of the two-level atoms, $\rho_{ee}-\rho_{gg}$ is the population inversion, and ρ_{eg} is the coherence. T_1 is the lifetime of the excited state and T_2 is the total dephasing time, discussed in more detail in the following section. We assume that the applied laser field is linearly polarized along the $\hat{x}$ direction. Thus, the electric field of the laser is $E(t) = \mathcal{E}e^{-i\omega t}\hat{x}+$ c.c.. In the rotating-wave approximation (i.e. ignoring the c.c. part of the electric field) the matrix element of the interaction Hamiltonian can be expressed as $V_{eg} = -\mu_{eg}\mathcal{E}e^{-i\omega t}$, where $\mu_{eg} = -e\langle e|x|g\rangle$ is the matrix element of the electric dipole moment, sometimes called the transition dipole moment for short.

The response of the atoms to a monochromatic field can be found by solving Eqs. (1.8) to (1.10) in steady-state. The electric dipole moment per unit volume is called the atomic polarization and is given by

$$P(t) = N\langle\mu\rangle = N\mathrm{Tr}(\rho\mu) = N(\mu_{eg}\rho_{ge} + \mu_{ge}\rho_{eg}), \tag{1.11}$$

where N is the number density of the atoms. We introduce the relation $P(t) = \mathcal{P}e^{-i\omega t}+$ c.c. to separate the fast oscillating part of the polarization from its complex amplitude $\mathcal{P}$. Therefore, the optical susceptibility can be found from

$$\mathcal{P} = \epsilon_0\chi\mathcal{E}. \tag{1.12}$$

Finally, the optical susceptibility is found to be [26]

$$\chi = \frac{N|\mu_{eg}|^2 T_2}{\epsilon_0 \hbar} \frac{\delta T_2 - i}{1 + \delta^2 T_2^2 + \Omega^2 T_1 T_2}. \tag{1.13}$$

We have defined the Rabi frequency as $\Omega = 2|\mu_{eg}||\mathcal{E}|/\hbar$ and the frequency detuning by $\delta = \omega - \omega_0$. One should note that Eq. (1.13) gives the total susceptibility that includes linear and nonlinear susceptibilities such as $\chi^{(3)}$ and $\chi^{(5)}$. To obtain the form of the linear susceptibility one can take the limit $\mathcal{E} \to 0$. The derivation of the density matrix equations (1.10) and their solutions are explained in great detail in Chapters 3 and 6 of Ref. [26].

In order to calculate the susceptibility of Rb atoms, we need to find the quantities appearing in Eq. (1.13); in section 1.3.1 we explain how to calculate the transition dipole moment μ_{eg} of the hyperfine transitions; the number density N is explained in section 1.3.2; finally, in section 1.3.3 we explain T_1 and T_2 and how to incorporate line broadening mechanisms such as the Doppler shift and the effect of Rb-Rb collision.

1.3.1 Rb hyperfine transition strengths

As discussed in section 1.2.2, Rb atoms contain several hyperfine energy levels. Furthermore, each hyperfine level F splits into $2F + 1$ magnetic sublevels m_F. We consider a transition between two magnetic sublevels with the electric dipole moment $\mu_{eg} = -e\langle g|x|e\rangle = -e\left\langle F_g, m_{F_g}\middle|x\middle|F_e, m_{F_e}\right\rangle$. We decompose this matrix element into two parts: the first part depends only on the angular part of the wavefunction and can be evaluated by employing the Wigner-Eckart theorem [27]. The second part (the reduced matrix element - see below) contains the radial component of the wavefunction, and of course, some angular dependence. In this way, the electric dipole moment for transition between $\left|F_g, m_{F_g}\right\rangle$ and $|F_e, m_{F_e}\rangle$ can be written as [12]

$$
\begin{aligned}
\left\langle F_g, m_{F_g} \middle| e r_q \middle| F_e, m_{F_e} \right\rangle =& (-1)^{L_e+S+J_g+J_e+I-m_{F_e}+1} \\
& \times \sqrt{(2J_g+1)(2J_e+1)(2F_g+1)(2F_e+1)} \\
& \times \begin{pmatrix} F_g & 1 & F_e \\ m_{F_g} & q & -m_{F_e} \end{pmatrix} \begin{Bmatrix} J_e & F_e & I \\ F_g & J_g & 1 \end{Bmatrix} \begin{Bmatrix} L_e & J_e & S \\ J_g & J_g & 1 \end{Bmatrix} \\
& \times \langle \alpha_g L_g || e r_q || \alpha_e L_e \rangle \, .
\end{aligned}
\tag{1.14}
$$

The round and curly brackets are Wigner-3j and Wigner-6j symbols respectively. $q \in \{-1, 0, 1\}$ indices the component of the position $\boldsymbol{r}$ in the spherical basis [27, 12]. Since each photon carries $\hbar$ spin angular momentum, q is also equal to the integer change in m_F upon the transition. Here we consider excitation with linearly polarized light for which we set $q = 0$. $\langle \alpha_g L_g || e r_q || \alpha_e L_e \rangle$ is called the reduced matrix element and is the only part that depends on the radial wavefunction. α_g and α_e represent all the other parameters of the states besides their orbital angular momentum. Note that the selection rules for the transition are essentially contained in the Wigner coefficients in Eq. (1.14).

For all atoms, except hydrogen, the radial part of the atomic wavefunction can only be calculated approximately. However, one can use the decay rate of the excited state to calculate the reduced matrix element $\langle \alpha_g L_g || e r_q || \alpha_e L_e \rangle$. It can be shown that the spontaneous decay rate is given by [28, 29]

$$
\Gamma = \frac{\omega_0^3}{3\pi\epsilon_0 \hbar c^3} \frac{2J_g+1}{2J_e+1} \left| \langle J_g || e\boldsymbol{r} || J_e \rangle \right|^2 . \tag{1.15}
$$

Again, by using the Wigner-Eckart theorem, $\langle J_g||e\boldsymbol{r}||J_e\rangle$ can be connected to $\langle L_g||e\boldsymbol{r}||L_e\rangle$ by the relation

$$\begin{aligned}\langle J_g||e\boldsymbol{r}||J_e\rangle =&(-1)^{J_e+L_g+S+1}\sqrt{(2J_e+1)(2L_g+1)}\begin{Bmatrix} L_g & L_e & 1 \\ J_e & J_g & S \end{Bmatrix} \\ &\times \langle L_g||e\boldsymbol{r}||L_e\rangle\,.\end{aligned} \tag{1.16}$$

For the D_2 line, the transition occurs between $|g\rangle = |L_g = 0, J_g = 1/2\rangle$ and $|e\rangle = |L_e = 1, J_e = 3/2\rangle$. Therefore, Eq. (1.16) reduces to

$$\langle J_g||e\boldsymbol{r}||J_e\rangle = \sqrt{\frac{2}{3}}\,\langle L_g||e\boldsymbol{r}||L_e\rangle\,. \tag{1.17}$$

The spontaneous decay rate is given by $\Gamma = 1/\tau$, where $\tau = 26.24\,\text{ns}$ ($27.70\,\text{ns}$) is the lifetime of the excited state of the $D_2(D_1)$ line [30]. Thus, we use Eqs. (1.16) and (1.17) along with these experimental values of the decay rates to calculate $\langle L_g||e\boldsymbol{r}||L_e\rangle$. Hence, the dipole moment for each hyperfine transition can be calculated from Eq. (1.14).

The square of the prefactor that is multiplied to the reduced matrix element in Eq. (1.14) (the first three lines on the right hand side) is called the transition strength and can be evaluated easily. The Wigner-3j and Wigner-6j symbols can be calculated by Mathematica using the commands *ThreeJSymbol* and *SixJSymbol*, respectively. In Fig. 1.2 we show the transition strengths for the D_2 transition line of ^{85}Rb and ^{87}Rb.

1.3.2 Rb number density

Rubidium has a low temperature melting point at 39.31°C. Therefore, the vapour pressure at moderate temperatures is significant. However, measuring the vapour

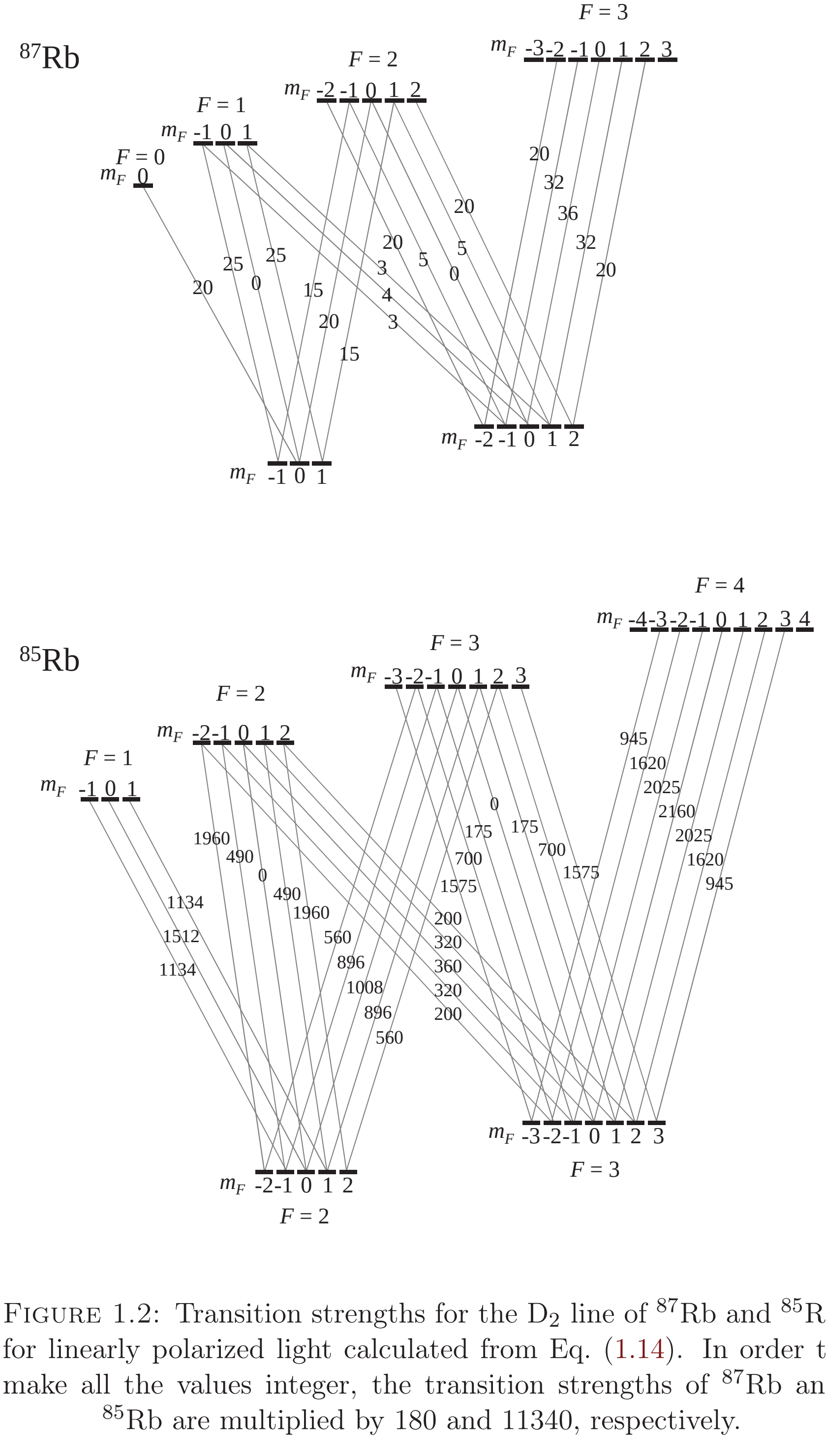

FIGURE 1.2: Transition strengths for the D_2 line of ^{87}Rb and ^{85}Rb for linearly polarized light calculated from Eq. (1.14). In order to make all the values integer, the transition strengths of ^{87}Rb and ^{85}Rb are multiplied by 180 and 11340, respectively.

pressure as a function of temperature is difficult and different empirical formulas are used in the literature:

$$\log_{10} p = 11.722 - \frac{4302}{T} - 1.5 \log_{10} T. \quad \text{Ref.[31]} \tag{1.18}$$

$$\log_{e} p = 16.063 - \frac{9140}{T}, \quad \text{Ref.[18]} \tag{1.19}$$

$$\log_{10} p = 7.193 - \frac{4040}{T}, \quad \text{Ref.[24]} \tag{1.20}$$

$$\log_{10} p = 15.883 - \frac{4529}{T} + 0.000587\, T - 2.99 \log_{10} T, \quad \text{Ref.[32]} \tag{1.21}$$

These equations provide the vapour pressure p of liquid Rb in Torr. The number density (atoms/m^3) can be calculated by

$$N = \frac{133.323}{k_B T}\, p, \tag{1.22}$$

where k_B is the Boltzman constant. Fig. 1.3 plots the number density of Rb atoms in liquid phase based on Eqs. (1.18) to (1.21). Similar formulas with different predictions are also available for the vapour pressure in the solid phase, i.e. for the temperatures below the melting point. However, since the majority of experiments are performed at temperature above the melting point, we merely provide the formula from Ref. [32]:

$$\log_{10} p = -94.048 - \frac{1961}{T} - 0.0377\, T + 42.575 \log_{10} T. \tag{1.23}$$

We should also emphasise that there are some subtleties in measuring the temperature of the atomic ensemble. In our laboratory, we used a 75-mm-long Rb cell and wrapped a heating wire around the two ends of the cell. We measured the temperature of the cell with a thermocouple attached to the centre of the cell, far

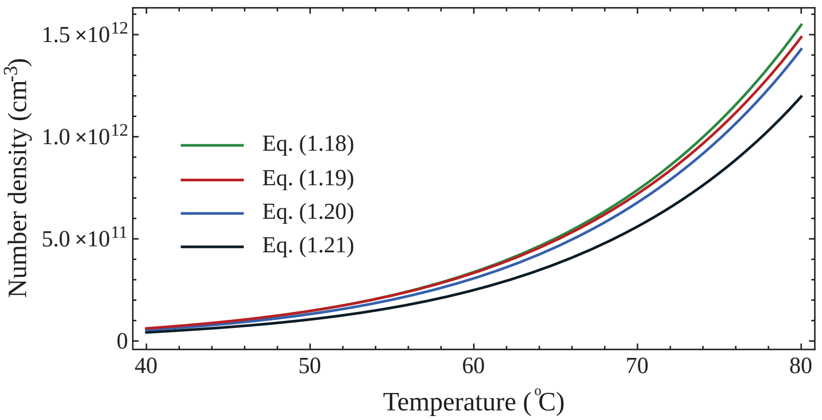

FIGURE 1.3: Number density of Rb atoms as a function of temperature. Different empirical formulas are used in the literature that predict different number densities at a given temperature.

from the heating wire. When we set the temperature to, let us say, 150°C, the reading from the thermocouple reaches the set point in a few minutes. However, by observing the transmission spectrum of the Rb cell, we realized that the number density is still rising gradually, even after several hours. Therefore, it takes several hours for the temperature of the atoms to reach the set point, although we had thermally insulated the cell. Hence, the actual temperature of the atoms is often lower than the reading of the thermocouple.

1.3.3 Line broadening mechanisms

In the weak field regime, i.e. when $\Omega^2 T_1 T_2 \ll 1$, the imaginary part of the susceptibility in Eq. (1.13) has a Lorentzian lineshape of width $\Delta\omega = 2/T_2$. At higher intensities, the lineshape retains its form, but its width increases to

$$\Delta\omega = \frac{2}{T_2}\sqrt{1+\Omega^2 T_1 T_2}. \tag{1.24}$$

This is known as the power broadening [28].

The atomic coherence ρ_{eg} and consequently the atomic polarization decay in a time scale T_2 given by

$$\frac{1}{T_2} = \frac{1}{2T_1} + \gamma_c. \tag{1.25}$$

The first term on the right hand side shows the decoherence (dephasing) rate due to the decay of the excited state population. γ_c is the pure dephasing rate due to the collision of the atoms and can be calculated from

$$\gamma_c = 2\pi\delta\nu_s \frac{N}{N_0}, \tag{1.26}$$

where $N_0 = 2.69 \times 10^{25}$ atoms/m^3 is the Loschmidt constant. The collisional broadening linewidth of the D_2 transition of Rb atoms at standard temperature and pressure is $\delta\nu_s \simeq 10^{12}$ Hz [18]. At temperatures above $\sim 120°\text{C}$ the collisional broadening becomes comparable to the natural linewidth of the transition and needs to be accounted for.

Another important mechanism that leads to the broadening of the transition line is the Doppler shift of the atomic transition frequency due to the thermal motion of the atoms. Unlike the other broadening effects discussed so far, the Doppler effect results in an inhomogeneous broadening which means that all the atoms are not equally affected. Therefore, the Doppler broadening cannot be incorporated directly into Eq. (1.13). To consider the effect of the Doppler shift, we take the convolution of the susceptibility in Eq. (1.13) with the Gaussian distribution of the atomic velocity. Therefore, the Doppler broadened susceptibility is given by

$$\chi_D(\omega) = \int_{-\infty}^{\infty} g(\omega')\chi(\omega - \omega')d\omega', \tag{1.27}$$

where the weight factor

$$g(\omega) = \frac{1}{\sqrt{\pi\sigma^2}} \exp\left[-\left(\frac{\omega}{\sigma}\right)^2\right], \tag{1.28}$$

is a normalized Gaussian distribution with $\sigma = \omega_0 u/c$, where $u = \sqrt{2k_B T/m}$ is the most probable speed in the distribution. If the susceptibility of an atom at rest has a Lorentzian lineshape, the Doppler broadened susceptibility will be given by the well known Voigt profile, which can be written in terms of the complementary error function. For a more general case where the susceptibility does not have a Lorentzian lineshape, the effect of the Doppler broadening must be calculated numerically.

1.3.4 Results

Each hyperfine transition depicted in Fig. 1.1 has a Voigt profile with an amplitude that depends on the strength of that particular transition as shown in Fig. 1.2. In the weak field regime, the total susceptibility is calculated by adding the susceptibility of each hyperfine transition. Hence, the transmission spectrum is given by $\exp(-\alpha L)$, where $\alpha = k\text{Im}\chi$ is the absorption coefficient and $L = 75\,\text{mm}$ is the length of our Rb cell. Fig. 1.4(a) shows the theoretical transmission spectrum of the D_2 line of natural Rb in the linear (weak field) regime for two different temperatures. The results are in agreement with the experimental results reported in Chapter 2. This comprehensive model of absolute transmission has been shown to predict the absolute absorption of the Rb vapour to better than 0.5% [32].

The transmission spectrum in Fig 2.1 was measured after setting the temperature of the cell to 160°C and waiting for one hour. However, later on, by tracking the transmission spectrum for a longer time we noticed that it takes more than eight hours for the temperature of the atoms to reach the the set point, as pointed out in

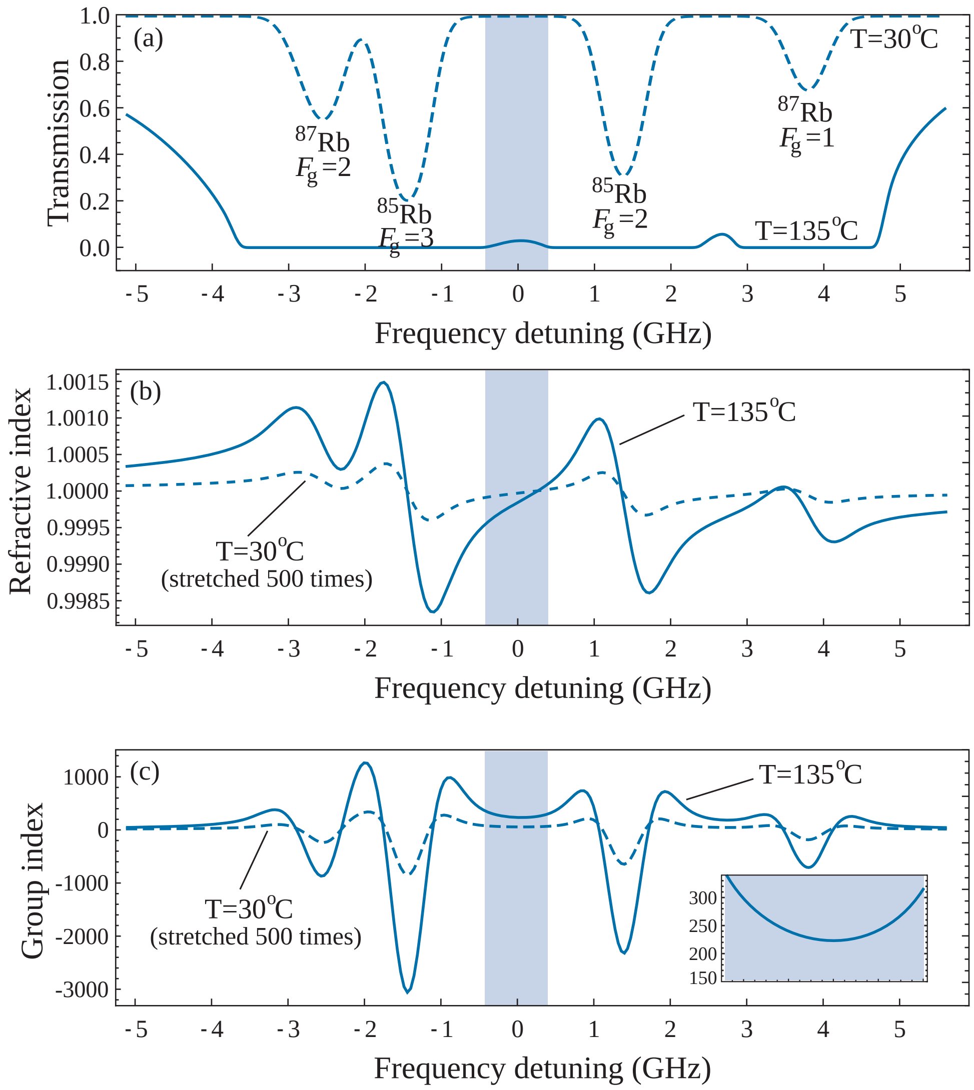

FIGURE 1.4: Theoretical calculation of (a) transmission spectrum (b) refractive index and (c) group index of the D_2 line for a Rb cell of length 75 mm filled with natural Rb. Zero detuning is set to the centre of the left transmission peak observed at 135°C. The shaded area shows the region of interest where our experiments are performed. The refractive and the group index at $T = 30°\text{C}$ are very close to unity. Thus, we have stretched the dashed lines in parts (b) and (c) by a factor of 500 to make the variations visible. The inset in (c) shows the group index in the region of interest at $T = 135°\text{C}$.

section 1.3.2. Therefore, we conclude that the actual temperature of the atoms in the experiment reported in Chapter 2 is about 15% lower than the reported values.

The refractive index $n \simeq 1 + \mathrm{Re}\chi/2$ and the group index $n_g = n + \omega dn/d\omega$ of the D_2 line in the linear regime are shown in Fig. 1.4(b) and (c), respectively. The experiment reported in Chapter 2 is performed in the transmission window shown in Fig. 1.4 by the shaded area. As shown in the inset of Fig. 1.4 (c), the group index in the region of interest is between 200 to 300 depending on the frequency detuning. This theoretical calculation of group index is also in excellent agreement with the experimental measurement reported in Chapter 2 (see Fig. 2.1).

In the nonlinear (strong field) regime, we define the saturation intensity I_s by

$$\frac{I}{I_s} = \Omega^2 T_1 T_2. \tag{1.29}$$

Thus, the susceptibility can be written as

$$\chi = \frac{N|\mu_{ba}|^2 T_2}{\epsilon_0 \hbar} \frac{\delta T_2 - i}{1 + \delta^2 T_2^2 + I/I_s}. \tag{1.30}$$

Each hyperfine transition has a different saturation intensity, depending on its transition strength. However, the saturation intensity for the cyclic transition between $|F = 2, m_F = 2\rangle$ and $|F = 3, m_F = 3\rangle$ of ^{87}Rb is often quoted as *the* saturation intensity of Rb atoms, which is $I_s = 1.67\,\mathrm{mW/cm^2} = 16.7\,\mathrm{W/m^2}$. Figure 1.5 shows the refractive index $n = \sqrt{1 + \mathrm{Re}\chi} \simeq 1 + \mathrm{Re}\chi/2$ of natural Rb at the D_2 transition line for three different laser intensities, calculated from Eq. (1.30). Our experiment with Rb in the nonlinear regime (Chapter 3) was performed at the frequency detuning shown by the dashed line in Fig. 1.5. At this wavelength, the refractive index is larger at higher laser intensities. Therefore, the laser beam experiences self-focusing.

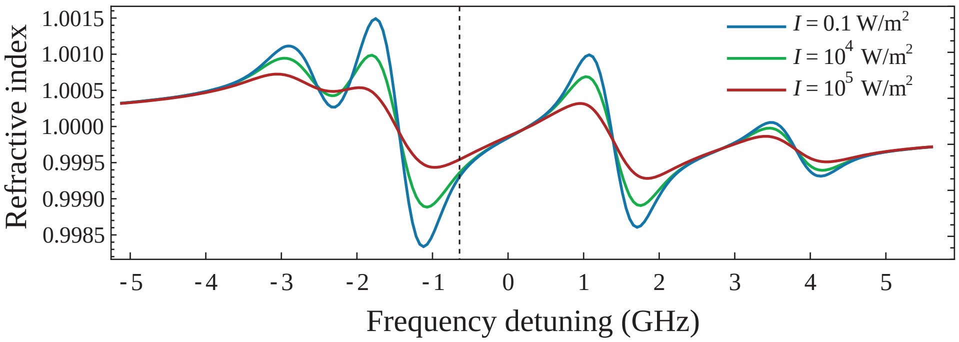

Figure 1.5: Refractive index of natural Rb at D_2 line in the nonlinear regime calculated from Eq. (1.30). Our nonlinear experiment presented in Chapter 3 was performed at the frequency detuning shown by the dashed line. At this wavelength, the refractive index is larger at higher laser intensities, resulting in self-focusing of the laser beam.

Equation (1.30) gives the total susceptibility of Rb atoms in two-level system approximation. However, Rb atoms are not truly two-level and the effect of optical pumping has to be considered. Rubidium atoms in the excited state can decay to either of the ground states that satisfy the selection rules and transfer the population to the state that is far detuned from the laser frequency. The optically pumped state relaxes to equilibrium by collisions. A rigorous treatment of optical pumping has to include the pumping rate and the relaxation due to collisions. Since the relaxation time scale is typically longer than the transit time through the laser beam, the atoms do not reach equilibrium during the interaction time and one has to average over a range of transit times [33]. Moreover, at high laser powers, optical pumping can align the Rb atoms. Therefore, calculating the exact response of the atoms in the nonlinear regime can be heavily involved. The interested reader can refer to Refs. [33, 34] for details. However, the effect of optical pumping in the steady state (which is of our interest) can be accounted for by replacing the saturation intensity with an effective saturation intensity [22]. In our experiment presented in Chapter 3, the laser frequency was blue detuned by 840 MHz from

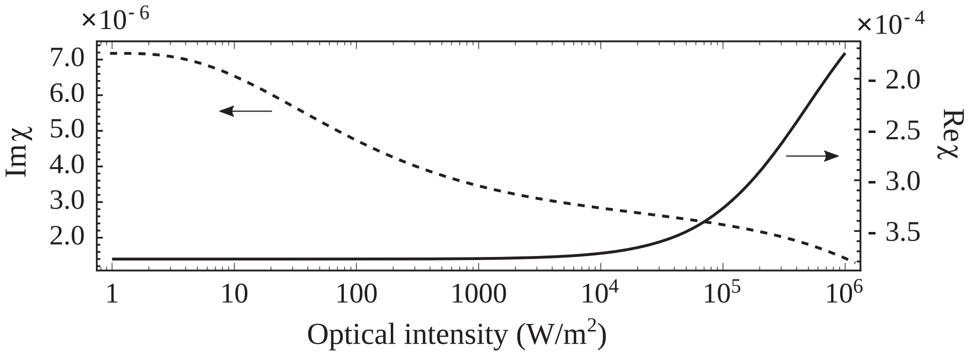

Figure 1.6: Real and imaginary parts of the total susceptibility of Rb vapour at the frequency detuning shown by the dashed line in Fig. 1.5. The effect of optical pumping is incorporated by employing an effective saturation intensity. Reχ and thus the refractive index increase with the intensity, indicating nonlinear focusing. Due to the saturation of absorption, Imχ and thus the absorption decreases with the laser intensity.

the $5^2S_{1/2}$, $F = 3 \rightarrow 5^2P_{3/2}$, $F = 4$ transition in ^{85}Rb. For this transition we use an effective saturation intensity of $3.1 \times I_s$ [35]. In Fig. 1.6 we plot the real and imaginary parts of the total susceptibility at this frequency detuning as a function of the laser intensity for a Rb cell at $T = 115$°C. The refractive index can be evaluated by $n = \sqrt{1 + \mathrm{Re}\chi} \simeq 1 + \mathrm{Re}\chi/2$ and the absorption coefficient by $\alpha = k\mathrm{Im}\chi$. Figure 1.6 shows that the high intensity region of a laser beam experiences a larger refractive index and also less absorption due to the saturation of absorption. In Chapter 3 we discuss an experiment where we use this nonlinear response of Rb atoms to generate and enhance the formation of caustics and rogue events.

Chapter 2

Light-Drag Enhancement by a Highly Dispersive Rubidium Vapour

This chapter is based on the following paper [36]:

A. Safari, I. De Leon, M. Mirhosseini, O. S. Magaña-Loaiza and R. W. Boyd, Phys. Rev. Lett. **116**, 013601 (2016). DOI:10.1103/PhysRevLett.116.013601.

Author contributions: R. W. Boyd conceived the idea. A. Safari conducted the experiment with assistance from I. De Leon, O. S. Magaña-Loaiza and M. Mirhosseini. A. Safari analyzed the data and wrote the manuscript. All authors discussed the results and commented on the manuscript. I. De Leon and R. W. Boyd supervised the project.

2.1 Abstract

The change in the speed of light as it propagates through a moving material has been a subject of study for almost two centuries. This phenomenon, known as the Fresnel light drag effect, is quite small and usually requires a large interaction path length and/or a large velocity of the moving medium to be observed. Here, we show experimentally that the observed drag effect can be enhanced by over two

orders of magnitude when the light beam propagates through a moving slow-light medium. Our results are in good agreement with the theoretical prediction, which indicates that, in the limit of large group indices, the strength of the light drag effect is proportional to the group index of the moving medium.

2.2 Introduction

The phenomenon of light dragging by a moving host medium has been known for many years. It was first predicted by Fresnel [37]on the basis of an elastic aether theory and was observed experimentally by Fizeau [38]. This effect, sometimes called Fresnel drag, can be explained by the special theory of relativity. Fresnel's theory ignores the effect of dispersion of the refractive index of the medium. The influence of dispersion on the light-drag effect was first predicted by Lorentz [39]. Zeeman and his collaborators performed a series of experiments over a period of more than 10 years [40, 41, 42, 43, 44, 45, 46] to measure the drag effect accurately. They observed the predicted contribution of dispersion on the light-drag effect by moving a 1.2-m-long glass rod at speed 10 m/s. However, in normal materials with low dispersive properties, the effect of dispersion is so small that the magnitude of this contribution can be disputed [47]. In the intervening years the Fresnel drag effect has been investigated many times for different purposes, for instance, for improving the measurement's accuracy [48, 49], differentiating it from competing effects such as the Sagnac effect [50, 51], dragging massive particles such as neutrons [52], and proposing dielectric analogs of gravitational effects [8].

Highly dispersive materials, including alkali atomic vapours, can enable the propagation of light pulses with extremely small group velocities [1, 2, 3]. This phenomenon, known as the slow-light effect, has received much attention in the past two decades [53]. Special relativity implies that the group velocity of light changes as one moves the slow-light material through which light propagates. This effect can be used to control the group velocity of laser pulses in a slow-light medium [14, 54]. It has also been shown theoretically that the light-drag effect can be significantly enhanced using a slow-light material [55, 56]. Moreover, a recent experiment demonstrated that spinning a slow-light material enhances the image rotation induced by rotary photon drag effect [57].

In this chapter we investigate the change in phase velocity of a light beam propagating through a slow-light material that results from moving the material along the direction of propagation. In our experiment, the slow-light material is a hot rubidium (Rb) vapour. We show experimentally that the dispersive contribution to the drag effect (which is usually considered to be a correction term for low-dispersion materials) is the dominant contribution in our case. Our results indicate an enhancement of the drag effect proportional to the group index of the medium, which in our case is $n_g \approx 330$.

2.3 Theory

As light enters a nondispersive medium with refractive index n, its phase velocity with respect to the reference frame attached to the medium changes to c/n. If the medium moves at speed v, light is dragged in the direction of motion. In effect, the phase velocity of light u with respect to the stationary laboratory frame is given by the relativistic addition of the two velocities v and c/n [58],

$$u = \frac{c/n \pm v}{1 + v/nc} \simeq \frac{c}{n} \pm v \left(1 - \frac{1}{n^2}\right), \tag{2.1}$$

where n is the refractive index of the moving medium. Throughout this chapter, we follow the convention that the upper and lower signs correspond to the medium moving along the direction of propagation and opposite to it, respectively. The approximation in Eq. (2.1) is valid for $v \ll c$. Equation (2.1) also assumes that the medium moves parallel to the light beam.

In a dispersive medium, the formula above has to be modified. Because of the Doppler effect, the frequency of the light ν as measured in the laboratory frame becomes $\nu' \simeq \nu\,(1 \mp v/c)$ as measured in the frame of the moving medium. Then, to first order in v/c, the refractive index for the moving medium is found to be

$$n(\nu') \simeq n(\nu) \mp \nu \frac{dn}{d\nu}\frac{v}{c}, \tag{2.2}$$

where $n(\nu)$ is the refractive index measured when the medium is at rest. By substituting $n(\nu')$ from Eq. (2.2) into Eq. (2.1), and keeping terms to first order in v/c, one obtains for the phase velocity in the moving medium

$$\begin{aligned} u &\simeq \frac{c}{n(\nu)} \pm v\left(1 - \frac{1}{n(\nu)^2} + \frac{n_g - n(\nu)}{n(\nu)^2}\right) \\ &\equiv \frac{c}{n(\nu)} \pm \Delta u, \end{aligned} \tag{2.3}$$

where Δu is the change in the phase velocity of light due to the drag effect. Here n_g is the group index defined as $n_g = n(\nu) + \nu dn/d\nu$. It follows that the phase shift induced by moving the medium with velocity v is given by

$$\Delta\phi \simeq \frac{2\pi v L n^2}{\lambda c}\left(\frac{1}{n} - \frac{1}{n^2} + \frac{n_g - n}{n^2}\right), \tag{2.4}$$

where $\lambda = c/\nu$ is the wavelength of light in vacuum, L is the length of the medium, and $n = n(\nu)$ for brevity. Laub [59] derived this formula for a medium with moving boundaries such as a glass rod. However, the first treatment of the light drag effect including the dispersion of the medium was due to Lorentz [39]. Following Fizeau's experiment, where water flows inside a fixed glass tube, Lorentz derived a slightly

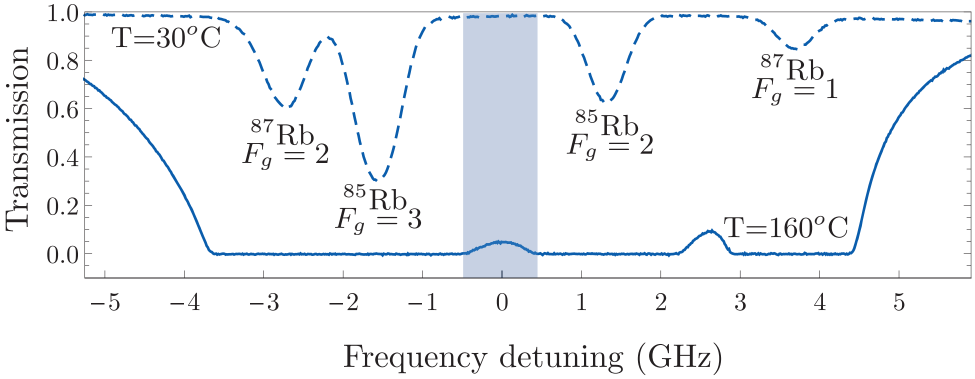

Figure 2.1: Experimental transmission spectra of natural Rb near the D_2 transition measured at two different temperatures. Zero detuning is set to the centre of the left transmission peak observed at 160°C. The label beneath each spectral feature gives the isotope and ground state hyperfine level responsible for that feature [32]. The shaded area shows the region where the experiment is performed (see Fig. 2.3).

different expression for the dragged velocity for fixed boundaries.

Slow-light materials, such as Rb atomic vapour, are known to have large group indices. Then, Eq. (2.3) indicates a large enhancement in the light drag effect, as compared to Eq. (2.1), for a highly dispersive medium. In the experiment reported below, n is nearly equal to unity. Therefore, $\Delta u \simeq \pm n_g v$, and also the difference between Laub and Lorentz's formulae is negligible.

2.4 Experiment

In our experiment, the moving medium is a glass cell of length $L = 7.5\,\mathrm{cm}$ filled with natural Rb. No buffer gas was added to the cell. Natural Rb consists of ^{85}Rb and ^{87}Rb with abundances 72% and 28%, respectively. Rb atoms represent a resonant atomic system and show large group indices near resonance [60].

Heating the Rb cell increases the number density of the atomic vapour, which enables us to achieve large group indices. Fig. 2.1 shows the transmission spectrum

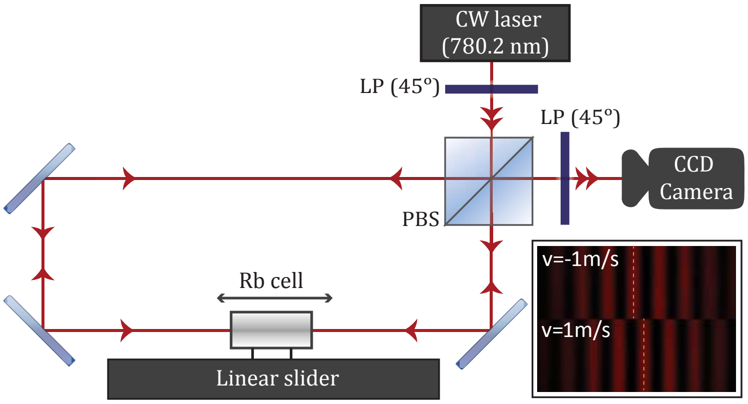

FIGURE 2.2: Ring interferometer used to measure the phase shift induced by light drag. LP is a linear polarizer and PBS is a polarizing beam splitter. The laser is operated at the Rb D_2 transition line, around zero frequency detuning shown in Fig. 2.1. The inset shows a sample fringe pattern with the maximum fringe displacement observed at 160°C. The upper and lower fringes are the fringe patterns as the cell moves to the left and right, respectively.

around the D_2 line of natural Rb measured at two different temperatures. A tunable continuous wave (CW) diode laser (Toptica DL Pro) with wavelength near 780.2 nm (Rb D_2 transition line) and the linewidth of less than 1 MHz is used. The laser operates with power 4.2 mW.

To observe the phase shift induced by the light drag effect, we use a ring interferometer (also known as a Sagnac interferometer) with the Rb cell moving within one arm as shown in Fig. 2.2. The two clockwise and counter-clockwise beams have the same power with orthogonal polarizations. Thus, they interfere only after the second polarizer. Since the two counter-propagating beams overlap, any phase shift induced by jitters or other noise is applied to both beams and does not influence the interference pattern that reveals the phase shift due to drag. The Rb cell is enclosed in an aluminium box with two glass windows with anti-reflection coating. To reduce heat dissipation and air turbulence around the box, the box is thermally insulated with a layer of cork sheet. A heating wire wrapped around the cell and

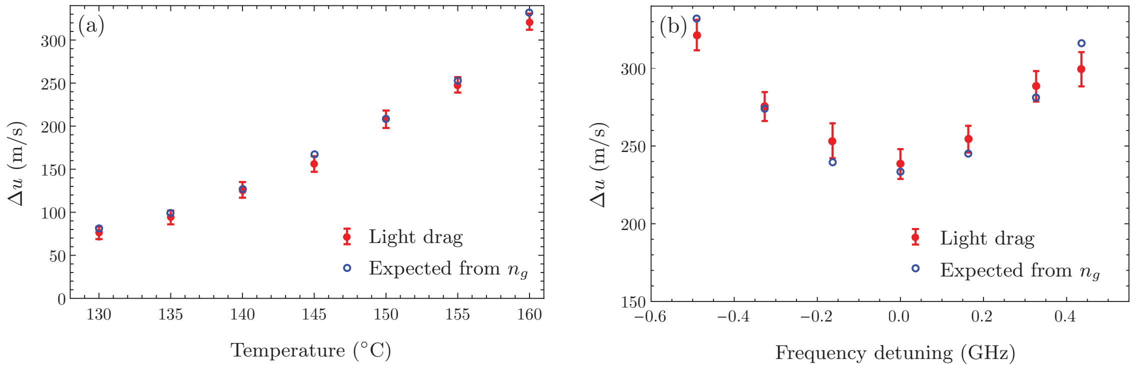

Figure 2.3: Change in phase velocity due to light drag, Δu, as a function of a) temperature and b) frequency detuning at a Rb temperature of 160°C, when the speed of the Rb cell is at maximum of $v = 1\,\mathrm{m/s}$. The contribution of dispersion $n_g v$ is shown with blue hollow circles. In (a) the laser is operated at -0.49 GHz frequency detuning (see Fig. 2.1).

a thermocouple attached to the cell control the temperature of the cell with an accuracy of ±1°C. The aluminium box is mounted on a motor-controlled linear slider that moves right and left at maximum speed of $v = 1\,\mathrm{m/s}$. A charge-coupled device (CCD) camera is triggered to capture an image of the fringe pattern when the cell is moving at maximum speed.

We measure the displacement of the interference fringes. For accurate measurement we misalign the interferometer by only a small amount to image a few fringe lines onto the camera. To increase accuracy, the fringes are recorded and averaged over 50 cycles. The main source of error is air turbulence around the Rb cell.

The phase difference between the two beams at the output of the interferometer, induced by the drag effect, is given in Table 2.1. The laser operates at -0.49 GHz frequency detuning (see Fig. 2.1), and the effect of dragging is measured at seven different temperatures from 130°C to 160°C at 5°C interval. Thermal equilibrium was reached between the readings. Uncertainties in Table 2.1 are the standard error of the mean of 50 different trials for each temperature.

The displacement of the fringe patterns normalized to the distance between the

Table 2.1: The observed phase shift in the light drag experiment at the output of the interferometer, $4\times\Delta\phi$, and the change in phase velocity, Δu, at different temperatures. The third column is the result of the drag experiment, and the last column shows the expected contribution of n_g.

Temperature (^{o}C)	$4 \times \Delta\phi$ (Rad)	Δu (Drag) (m/s)	Δu (Expected) (m/s)
130	0.60 ± 0.06	75 ± 7	81 ± 1
135	0.75 ± 0.06	93 ± 8	98 ± 1
140	1.01 ± 0.07	125 ± 9	126 ± 1
145	1.25 ± 0.07	155 ± 9	166 ± 1
150	1.67 ± 0.08	207 ± 10	208 ± 2
155	1.99 ± 0.07	247 ± 9	252 ± 2
160	2.58 ± 0.08	320 ± 9	331 ± 2

fringes at the output of the interferometer is given by $\Delta Z = 4 \times \Delta\phi/2\pi$, where $\Delta\phi$ is given in Eq. (2.4). The factor 4 comes from the fact that there are two counter-propagating beams going through the cell and we compare the left moving fringes with the right moving ones. The change in phase velocity due to light drag, Δu, is given in the third column of Table 2.1. It is obtained from Eq. (2.3) with the help of Eq. (2.4) and the fact that the refractive index of Rb vapour $n(\nu)$ is equal to unity to good approximation [60]. Fig. 2.3(a) plots the change in phase velocity Δu as a function of temperature.

To confirm that the observed effect is in fact the consequence of dispersion and comes from the group index in Eq. (2.3), we measured the group index directly for the same wavelength and temperatures. The experimental setup for this measurement is shown in Fig. 2.4. An electro-optic modulator (EOM) fed by a signal generator is used to produce pulses of 10 ns duration. The group velocity of the laser pulses inside the stationary Rb cell is given by c/n_g. The group delay experienced by the laser pulses is measured by an oscilloscope. The group indices thus obtained are used in Eq. (2.3) to calculate the expected change in phase velocity.

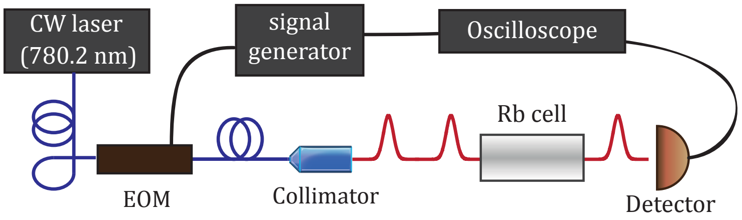

Figure 2.4: Experimental setup to measure the group index of the Rb vapour. An electro-optic modulator (EOM) is used to generate laser pulses of 10 ns width, and the time delay is measured by an oscilloscope.

The results are shown in the last column of Table 2.1 and in Fig. 2.3 with blue hollow circles. The uncertainty is determined by repeating the measurements several times and taking the standard error of the mean. It can be seen that the observed drag effect is in very good agreement with the prediction of theory.

For further confirmation of the understanding of the light drag effect we also measured the light drag as a function of the frequency detuning at a Rb temperature of 160°C. The measurement is performed in the spectral region shown in Fig. 2.1 with shaded area. The results are shown in Fig. 2.3(b), along with the expected effect of the group index.

At high optical powers one might expect to see the effects of optical pumping and saturation [61]. However, in the temperature range used in this work, we did not see any appreciable change in the transmission spectrum when we increased the power from a few microwatts to a few milliwatts. Since the laser frequency is about 1 GHz away from resonances, only the small fraction of atoms that are Doppler shifted into resonance are saturated. Optical hyperfine pumping reduces the absorption by transferring atoms from one hyperfine ground level to another level. Nevertheless, at high temperatures, atom-atom collisions quickly redistribute population among the hyperfine ground levels. Thus, the effect of optical pumping is diminished by the short relaxation time at high temperatures.

The refractive index of the Rb gas inside the cell is very close to unity ($n \simeq 1$). Thus, the non-dispersive contribution to the light drag effect is due only to the four glass windows fixed to the Rb cell assembly, which have a combined thickness of 2 cm. According to Eq. (2.4), the contribution of the moving windows in the observed phase shift is about 0.001 rads., which is much smaller than the uncertainty of $\Delta\phi$ in Table 2.1. Therefore, the observed drag effect is due primarily to the dispersion of the Rb vapour. We verified this conclusion by performing additional measurements far from the atomic resonances (where $n_g \approx 1$), and noting that no net displacement of the fringe pattern is detected as the cell was moved (data not shown).

In typical materials with low dispersive properties, the contribution of dispersion in light drag is almost negligible. Zeeman and his colleagues [45] used a 1.2-m-long glass cylinder moving at speed 10 m/s. They observed the phase shift $\Delta\phi = 0.38$ radians out of which 0.04 radians was the contribution of dispersion.

In a non-dispersive medium, Eq. (2.1) implies that the speed of light cannot be changed by more than the translational speed of the medium. However, one sees from Eq. (2.3) that by using a highly dispersive medium, one can exceed this limit. In our experiment, the speed of light is changed by $n_g \times v \simeq 330\,\mathrm{m/s}$, where v is 1 m/s, indicating an enhancement of more than two orders of magnitude as compared to dragging light with a low-dispersive medium. The enhancement observed in this work is in fact a manifestation of the Doppler shift and can also be called the enhanced Doppler effect. Therefore, a highly dispersive medium moving in an interferometer provides a sensitive method to detect linear motions.

With the technique of electromagnetically induced transparency (EIT), group indices as large as 10^7 are achievable [1]. Therefore, one can enhance the observed effect by an even larger factor, which could enable accurate detection of extremely slow speeds [55]. Note, however, that for very large group indices one has to keep higher-order corrections in Eq. (2.3), which cause the effect to saturate for large speeds.

2.5 Conclusion

In summary, we investigated the change in phase velocity of light propagating through a moving slow-light medium. We moved a warm Rb cell at speed 1 m/s and observed a maximum change of 330 m/s in the phase velocity of light. The enhancement observed in the Fresnel light-drag effect is proportional to the group index of the moving medium. This enhancement is due to the large group index of a Rb vapour and can be understood by means of the Doppler effect. By using techniques such as EIT, one can achieve very large group indices. Then, this immensely enhanced effect could be employed to increase the sensitivity of devices that work based on the Doppler effect.

Chapter 3

Generation of Caustics and Rogue Waves from Nonlinear Instability

This chapter is based on the following paper [62]:

A. Safari, R. Fickler, M. J. Padgett and R. W. Boyd, Phys. Rev. Lett. **119**, 203901 (2017). DOI:10.1103/PhysRevLett.119.203901.

Author contributions: R. W. Boyd and M. J. Padgett conceived the idea. A. Safari and R. Fickler conducted the experiment. A. Safari performed the simulation with substantial help from R. Fickler and M. J. Padgett. A. Safari analyzed the data and wrote the manuscript. All authors discussed the results and commented on the manuscript. R. W. Boyd supervised all aspects the project.

3.1 Abstract

Caustics are phenomena in which nature concentrates the energy of waves and may exhibit rogue-type behaviour. Although they are known mostly in optics, caustics are intrinsic to all wave phenomena. As we demonstrate in this chapter, the formation of caustics and consequently rogue events in linear systems requires strong phase fluctuations. We show that nonlinear phase shifts can generate sharp

caustics from even small fluctuations. Moreover, in that the wave amplitude increases dramatically in caustics, nonlinearity is usually inevitable. We performed an experiment in an optical system with Kerr nonlinearity and simulated the results based on the nonlinear Schrödinger equation and achieved perfect agreement. As the same theoretical framework is used to describe other wave systems such as large-scale water waves, our results may also aid the understanding of ocean phenomena.

3.2 Introduction

Caustics can be defined as the envelope of a family of rays that define the flow of energy [63]. The energy of a wave field increases significantly on caustics compared to the adjacent space. When a wave acquires random phase fluctuations with correlation length larger than the wavelength of the wave, random caustics are formed upon linear propagation. Such random caustics are related to the phenomenon of branched flow observed in electron gases [64] and in microwaves [65]. A familiar example of random optical caustics is the bright pattern appearing on the bottom of a swimming pool on a sunny day. Moreover, caustics are also found in large-scale wave systems such as oceans. It has been shown that a large underwater island can act as a lens and focus the energy of tsunami waves into caustics [66]. Subsequently, recent studies show that a small uncertainty in the profile of an ocean floor can change the caustic pattern and lead to an unexpectedly large variation in the wave height of tsunamis [67].

Although caustics can develop from Gaussian fluctuations, they have non-Gaussian statistics with a very long tail, meaning that waves with extremely large amplitudes appear more often than predicted from a normal distribution. The long-tailed distribution is an indication of rogue-type waves, initially studied in the context of giant waves in oceans [68]. Rogue-type events are observed in various systems including optics [69, 9, 70, 71]. The formation of rogue events in (1D+1) waves (one spatial dimension plus time) has been extensively studied. Nonlinearity, namely modulational instability, is commonly used to explain how rogue waves develop in these (1D+1) systems such as unidirectional water waves and optical fibers. However, the dynamics of waves is richer in higher spatial dimensions where rogue waves can form from spatial focusing of waves (due to different propagation directions) without the aid of nonlinearity. In fact, numerous studies have shown that concentration of waves in caustics is a linear mechanism that can generate rogue waves in oceans [72, 73, 74, 75] and also in optics [76]. However, the role of nonlinearity in the formation of rogue waves is still under debate. In optical systems, nonlinearity can either trigger [77] or destroy [78] rogue events. Similarly, recent studies explain oceanic rogue waves without modulational instability [79] or any type of nonlinearity [80].

In this chapter, we investigate the effect of nonlinearity on the formation of optical caustics in (2D+1), where light propagates in two transverse directions plus one longitudinal direction along the beam axis, z. This effect has been studied previously in the context of nonlinear wave-current interactions in oceans [75, 81], and it has been stated that nonlinearity may wash out caustics and decreases the amplitude of extreme waves by destroying the phase coherence [68]. However, to our knowledge, the effect of nonlinear instability on the formation of caustics is not well examined. We show that in contrast to linear propagation where relatively large fluctuations are required [76], even small phase fluctuations can generate sharp caustics with the aid of nonlinear instability in the spatial propagation. Our experiment shows that while rogue waves can form in linear systems, nonlinearity facilitates the formation of rogue waves by removing the requirement of large fluctuations in the system.

3.3 Experiment

We first study caustic formation for the case of linear propagation through free space. In order to generate optical caustics in the laboratory, we use collimated continuous wave (cw) laser light with a beam waist of $w_0 \simeq 1\,\mathrm{mm}$, and modulate its phase front with a smooth random phase mask. We implement this random phase modulation by forming a computer-generated hologram on a spatial light modulator (SLM) to create a phase mask. The hologram is blazed to maximize the efficiency of the first diffracted order, which is separated from the other orders by use of an aperture. The random phase across the mask has a Gaussian distribution with correlation length $\delta = 150\ \mu\mathrm{m}$ and an amplitude Δ that can vary up to 16π (Fig. 3.1). An imaging system is used to image the SLM plane and expand the beam by a factor of two. Upon propagation in free space, an intensity pattern is formed that is imaged onto a CCD camera (640×640 pixels and 8-bit depth) with another imaging system. The recorded structure of the pattern depends on the random phase mask displayed on the SLM. The amplitude of the imprinted phase determines the strength of the intensity maxima in the caustics and the distance l at which the sharpest pattern is formed. The degree of sharpness can be quantified by the scintillation index defined by [82, 83]

$$\beta^2 = \frac{\langle I^2 \rangle - \langle I \rangle^2}{\langle I \rangle^2}, \tag{3.1}$$

where $\langle ... \rangle$ indicates the spatial average over the transverse plane. Speckle patterns that obey Gaussian statistics, for example, have a scintillation index of unity. A scintillation index above unity indicates the strength of concentration of light with respect to the adjacent space. Thus, the sharper the caustic, the higher the scintillation index. For our system, we found out that when Δ is greater than 6π, the scintillation index goes above unity after 7.5 cm (the length of our nonlinear medium employed later) of propagation in linear space. Therefore, we take this value as the caustic threshold in our experiment. One should note that this threshold is not universal and depends on parameters such as the wavelength and the correlation length, δ.

Figure 3.2(a), (b) and (c) show the sharpest patterns formed from three different phase masks with amplitudes $\Delta = 2\pi$, 8π and 16π, after propagation distances of $l = 27.5$ cm, 10.5 cm and 7.5 cm, respectively. This figure clearly shows that a sharp caustic is formed only if the phase variations are large. When the phase variations are small compared to the caustic threshold, 6π, the power of the caustic focus is weak, the pattern is blurred and is formed at a longer distance. To verify that this observation holds in general and not only for the patterns shown, we generated a set of 1000 uncorrelated phase masks for each amplitude Δ, and evaluated the statistical distribution of intensities in the final patterns. Since the Gaussian transverse profile of the laser beam is superimposed on the patterns, one does not obtain an unbiased intensity distribution within each pattern. Therefore, we considered the intensities of pixels along a circular annulus centred on the beam axis. As shown in Fig. 3.2(d) (blue circles) when the phase modulation is weak ($\Delta = 2\pi$) the statistical distribution closely follows an exponential decay. However, as mentioned earlier, caustic patterns have heavy-tailed statistics [84, 85]. This is confirmed in our measurements, Fig. 3.2(d); as the phase variations get stronger, so do the intensity fluctuations and the statistics become non-Gaussian. Note that the histograms in Fig. 3.2(d) are plotted in logarithmic scales and the intensities are normalized to the average intensity in each histogram. Thus, strong phase fluctuations can generate rogue events with intensities up to 45 times larger than the average intensity.

In order to quantify the heavy-tailed behaviour we have used a least-square

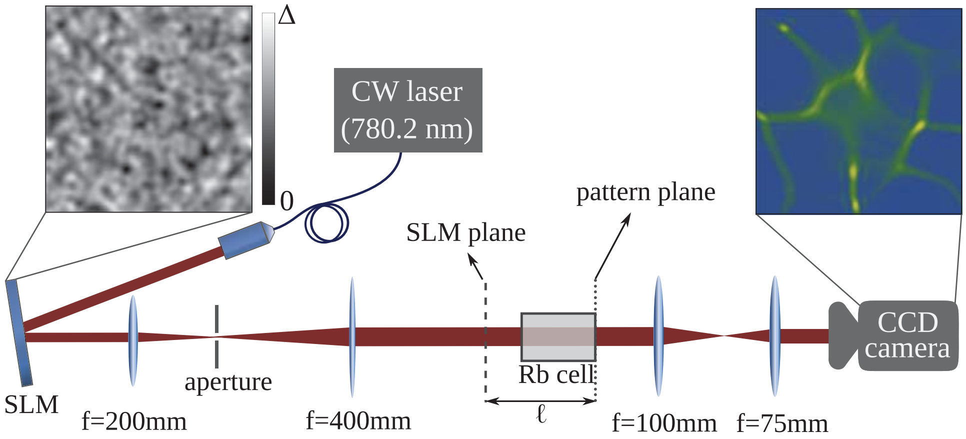

FIGURE 3.1: Scheme of the experimental setup. The spatial light modulator (SLM) imprints a random phase mask (upper-left inset) onto the transverse profile of a cw laser beam. The first imaging system images the SLM onto the plane shown by the dashed line (SLM plane). At this point the transverse intensity distribution of the beam follows the Gaussian profile of the input laser. An intensity pattern develops upon propagation. The distance l, after which the sharpest pattern is formed depends on the amplitude Δ of the phase modulation. Another imaging system is used to image the pattern plane (dotted line) onto the CCD camera. The upper-right inset shows an example pattern generated from $\Delta = 8\pi$. To study nonlinear propagation, the Rb cell is placed in the end of the propagation before the pattern plane.

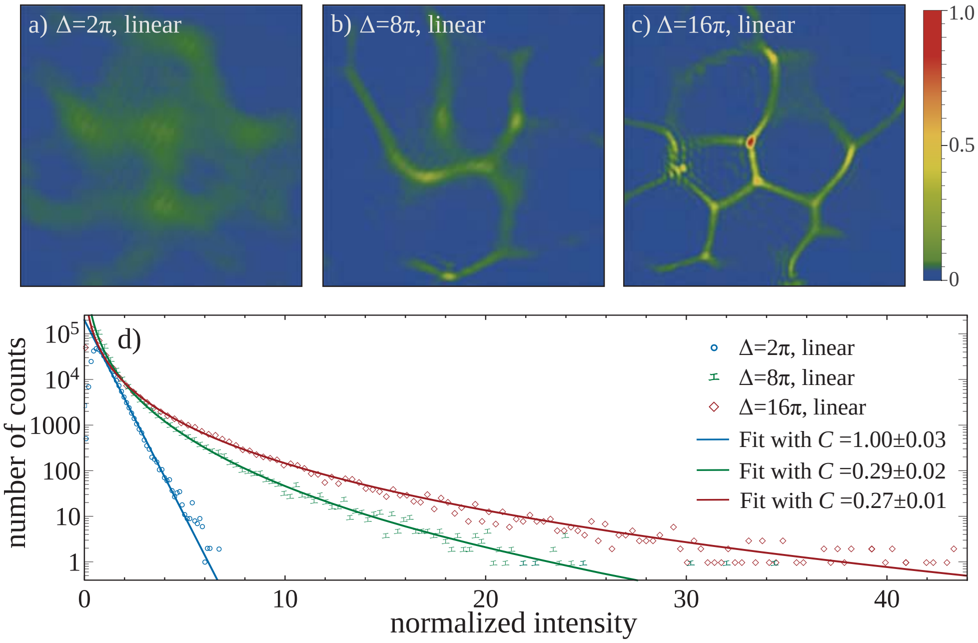

FIGURE 3.2: Generation of caustics upon linear propagation. a, b, c) Examples of patterns formed after propagation in free space from different phase masks with amplitudes $\Delta = 2\pi$, 8π and 16π, respectively. We see that sharp caustics are formed only under strong phase modulation. d) Intensity distributions for the patterns generated upon propagation through free space from three different phase amplitudes Δ. The C-parameter from the fit function characterizes the heavy-tailed behaviour; the lower the C-parameter, the longer the tail of the distribution. Thus, sharp caustics are distinguished by their heavy-tailed statistics.

method to fit the distribution with a stretched exponential function $A\exp\left(-BI^{C}\right)$, where A, B and C are the fitting parameters and I is the normalized intensity [77]. We are interested primarily in the C-parameter as it indicates the curvature of the function and quantifies the heavy-tailed behaviour. In speckle patterns generated from random scatterer, the intensity obeys negative exponential statistics, and thus $C = 1$. As C becomes smaller, the tail of the distribution gets longer. The solid lines in Fig 3.2(d) show the fit functions with the indicated C-parameters. As expected, the patterns generated from strong phase modulations ($\Delta = 16\pi$) have the lowest C-parameters, and thus the strongest rogue-type statistics.

To investigate the effect of nonlinearity on the formation of caustics we use rubidium (Rb) vapour as the nonlinear medium. The motivation for using atomic vapours as the nonlinear medium is that they can be saturated easily and thus show large nonlinearity that can be controlled simply through the laser frequency detuning. The Rb cell is 7.5 cm long and is filled with natural Rb: ^{85}Rb and ^{87}Rb with abundances of 72% and 28%, respectively. The Rb cell is heated to 115 °C. The cw laser with the wavelength of $\sim 780.2\,\mathrm{nm}$ and the linewidth of less than $1\,\mathrm{MHz}$ is blue detuned by 840 MHz from the $5^2S_{1/2}$, $F = 3 \rightarrow 5^2P_{3/2}$, $F = 4$ transition in ^{85}Rb. The cell is placed in the setup (Fig. 3.1) such that the last 7.5 cm of propagation before the caustic pattern is formed in the linear case is now taking place within Rb. The camera images the output of the cell. The laser power at the entrance of the cell is approximately 140 mW. Real (Re) and imaginary (Im) parts of the total susceptibility are calculated from our theoretical model based on Ref. [26]. Doppler broadening is implemented by calculating the convolution of the power broadened lineshape with the Gaussian distribution of the atomic velocities [28]. An effective saturation intensity is incorporated to take into account the effect of optical pumping [86]. As shown in Fig. 3.3(a), Re χ and consequently the refractive index $n \simeq 1+\text{Re }\chi/2$ increases with intensity. Thus, self-focusing is expected at this frequency detuning. The maximum nonlinear phase shift experienced by the laser light in passing through the Rb cell is approximately 4π radians. Im χ and therefore absorption decreases with intensity, indicating saturation of absorption.

For direct demonstration of the effect of nonlinearity, we employed the same sequence of phase masks as for the study of linear propagation. A comparison of the resulting patterns after nonlinear propagation (Fig 3.3) with those of Fig. 3.2 for linear propagation indicates that nonlinear instability in spatial propagation enhances the sharpness of the patterns without changing their overall structure.

This enhancement is more profound when the linear caustic is weak, i.e. when the phase modulation is not strong enough to form sharp caustics upon linear propagation. In the presence of nonlinearity, all patterns have approximately the same maximum intensity which is about 25% of the maximum intensity of the linear case. Although this decrease in intensity, which is due to linear absorption, reduces the strength of nonlinearity, it does not play a central role in our results. Moreover, absorption can be neglected when the laser frequency is far from resonance and a longer nonlinear medium is used [87].

The statistical distribution of intensities after nonlinear propagation (Fig. 3.3(e)) confirms that when the phase modulation is weak ($\Delta = 2\pi$) nonlinearity changes the distribution substantially. Conversely, the effect of nonlinearity on the statistics is negligible for $\Delta = 16\pi$. This is in contrast to the conclusions reached in Ref. [78] where the heavy-tailed distribution is found to be suppressed by nonlinear propagation. Moreover, the statistics in Fig. 3.3(e) indicate that, under nonlinear propagation condition, the smallest phase modulation generates the largest rogue events; up to 75 time larger than the average intensity. Note that the intensities in Fig. 3.3(e) are normalized to the average intensity in each histogram.

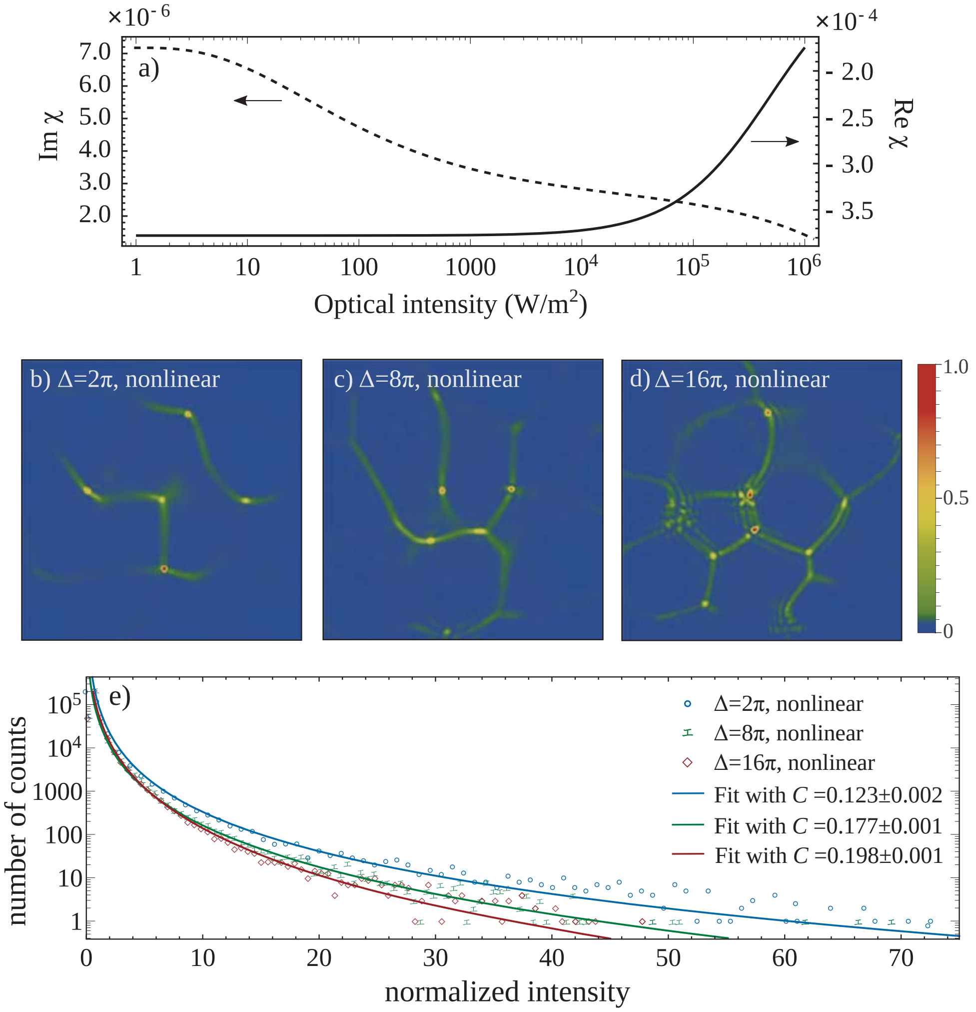

Figure 3.3: Generation of caustics upon nonlinear propagation. a) Real and imaginary parts of the total susceptibility of Rb vapour. Re χ and thus the refractive index increases with intensity, indicating nonlinear focusing. b, c, d) Caustic patterns generated from the same phase masks as in Fig. 3.2, but after the nonlinear propagation in Rb. In contrast to the linear case shown in Fig. 3.2, even small phase modulations, with the aid of nonlinear focusing, can concentrate light into sharp caustics. e) Intensity distributions of the nonlinear caustic patterns generated from three different phase amplitudes Δ.

3.4 Simulation

For further investigations and to test the role of Kerr nonlinearity on the formation of nonlinear caustics, we simulated the results of our experiment numerically using a beam propagation method based on the use of the fast Fourier transform. Similar to the propagation of waves in fluids, the propagation of the laser field through Rb vapour is described by the nonlinear Schrödinger equation (NLSE)

$$\frac{\partial \mathcal{E}}{\partial z} - \frac{i}{2k}\nabla_{\perp}^{2}\mathcal{E} = \frac{ik}{2\epsilon_0}P, \tag{3.2}$$

where $\mathcal{E}$ is the field amplitude defined by $E = \mathcal{E}e^{i(kz-\omega t)}$+c.c. and $\nabla_{\perp}^{2} = \partial^2/\partial x^2 + \partial^2/\partial y^2$ is the transverse Laplacian. For a purely third-order nonlinear medium the atomic polarization is given by $P = 3\epsilon_0\chi^{(3)}|\mathcal{E}|^2\mathcal{E}$. However, to include higher order effects, we use the more general form $P = \epsilon_0\chi_{(\mathcal{E})}\mathcal{E}$. The total susceptibility, $\chi_{(\mathcal{E})}$, is taken from our Rb numerical model, as shown in Fig. 3.3(a), without any adjustable parameters. The split-step method [88] was used to implement nonlinearity in the simulation. To be able to compare the results directly with the experimental patterns, we used the same random phase masks as in the experiment. All simulation results for both linear and nonlinear cases are in extremely good agreement with the experiment (example patterns from the simulation are shown in Fig. 3.4). This excellent matching of the results confirms that Kerr-saturated nonlinearity is the mechanism behind the generation of caustics from small phase fluctuations.

Since experimental imaging techniques are not compatible with nonlinear propagation, we cannot use imaging to determine the patterns within the Rb cell. However, our numerical simulation reproduces the experimental results accurately. We are thus confident in using our numerical method to study the patterns within

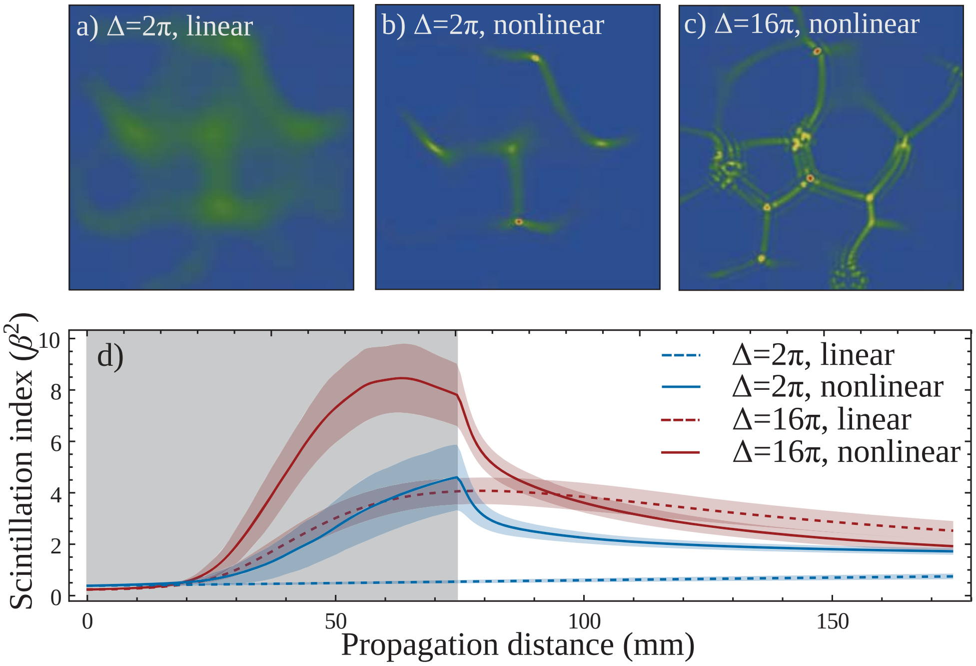

FIGURE 3.4: Intensity patterns and scintillation indices from computer simulation. a, b, c) Patterns obtained from the numerical simulation, which show excellent agreement with the experimental results shown in Figs. 3.2 and 3.3. d) Scintillation indices, β^2, averaged over 1000 patterns, calculated from our numerical simulation, as a function of the propagation distance from the entrance of the Rb cell up to 100 mm after the cell where partial speckles are formed. The grey area indicates the 7.5-cm-long Rb cell for the nonlinear cases and the shaded regions show one standard deviation from the mean. The nonlinear patterns have larger scintillation indices compared to the corresponding linear cases. A scintillation index greater than unity indicates the presence of sharp caustics.

the nonlinear medium. We use the scintillation index (Eq. 3.1) to characterize the sharpness of the caustics. Fig. 3.4(d) shows how the scintillation indices vary in linear and nonlinear propagation from the entrance of the Rb cell up to 100 mm after the cell, where partial speckles are formed. Inside the Rb cell, the nonlinear focusing exceeds diffraction and thus accentuates the caustic focusing. Therefore, the scintillation index tends to be large and to increase with propagation distance. After the cell, the scintillation index drops very quickly as the result of diffraction.

3.5 Conclusion

In conclusion, linear caustics and nonlinear instability are known to be responsible for focusing the energy of waves and for generating rogue-type events in various systems. Here, we experimentally and numerically investigated wave dynamics in the presence of both mechanisms. Our results show that the formation of caustics in Kerr media requires significantly smaller fluctuations compared to linear propagation. Thus, nonlinear instability in spatial propagation amplifies even small phase fluctuations and generates rogue-type waves with very large amplitudes. Therefore, although nonlinearity is not essential for generation of rogue waves, it enhances the strength of the rogue waves with respect to the average intensity and mitigates the requirement of large fluctuations in the medium. Our experiment was performed in a nonlinear optical system, and the NLSE was used to simulate the dynamics. Importantly, the NLSE also describes the nonlinear wave propagation in different physical systems, such as fluids [89] and Bose-Einstein condensates [90], both of which exhibit caustics as well [91]. Therefore, the nonlinear generation and enhancement of caustics and rogue-type events, which we observed, are not limited to optics and might also be realized in other physical systems.

Chapter 4

Exotic Looped Trajectories of Photons in Three-Slit Interference

This chapter is based on the following paper [92]:

O. S. Magaña-Loaiza, I. De Leon, M. Mirhosseini, R. Fickler, A. Safari, U. Mick, B. McIntyre, P. Banzer, B. Rodenburg, G. Leuchs and R. W. Boyd, Nature Communication **7**, 13987 (2016). DOI:10.1038/ncomms13987.

Author contributions: O.S.M.-L. conceived the idea with help from I.D.L and R.W.B. The experiment was designed by I.D.L., O.S.M.-L. and R.W.B. The numerical analysis was carried out by I.D.L. The theoretical description of our work was developed by B.R. and M.M. The experiment was performed by O.S.M.-L., I.D.L, R.F. and A.S., the samples were fabricated by U.M., B.M., P.B., and G.L. The data was analyzed by O.S.M.-L. and I.D.L. with help from B.R. and M.M. The project was supervised by G.L. and R.W.B. All authors contributed to the discussion of the results and to the writing of the manuscript.

4.1 Abstract

The validity of the superposition principle and of Born's rule are well-accepted tenants of quantum mechanics. Surprisingly, it has been predicted that the intensity pattern formed in a three-slit experiment is seemingly in contradiction with the most conventional form of the superposition principle when exotic looped trajectories are taken into account. However, the probability of observing such paths is typically very small, thus rendering them extremely difficult to measure. Here we confirm the validity of Born's rule and present the first experimental observation of exotic trajectories as additional paths for the light by directly measuring their contribution to the formation of optical interference fringes. We accomplish this by enhancing the electromagnetic near-fields in the vicinity of the slits through the excitation of surface plasmons. This process increases the probability of occurrence of these exotic trajectories, demonstrating that they are related to the near-field component of the photon's wavefunction.

4.2 Introduction

The phenomenon of interference has been recognized as "the only mystery" of quantum mechanics [93]. The enormous interest and history of this fundamental effect can be traced back to the two-slit experiment devised by Thomas Young in the early 19th century. Young's experiment is conceptually the simplest method for demonstrating the superposition principle, as the appearance of interference fringes in the far-field is unexplainable unless it is understood that the particle seemingly travels through both slits simultaneously. Such an experiment, originally performed with light, has since been conducted on particles ranging from individual photons, neutrons, and atoms, to large molecules consisting of dozens of atoms [94]. As the superposition principle lies at the core of quantum physics, many of its counterintuitive features such as entanglement, non-locality, wave-particle duality, and delayed-choice concepts can be demonstrated or tested using a two-slit system [95, 96, 97, 98, 99, 100, 101, 102].

The standard interpretation of the two-slit experiment is given by solving the wave equation for an initially prepared complex wavefunction, ψ. For example, if ψ_A represents the wavefunction at the detector for a photon emerging from slit A, and ψ_B is the wavefunction for a photon emerging from slit B, then the implementation of the superposition principle is to assume that the wavefunction is a superposition of the different paths given by $\psi_{AB} = \psi_A + \psi_B$. The probability of detection is given by Born's rule as

$$P_{\mathrm{AB}} \equiv |\psi_{\mathrm{AB}}|^2 = P_{\mathrm{A}} + P_{\mathrm{B}} + (\psi_{\mathrm{A}}^* \psi_{\mathrm{B}} + \psi_{\mathrm{A}} \psi_{\mathrm{B}}^*)\,, \tag{4.1}$$

where $P_{\mathrm{A}} = |\psi_{\mathrm{A}}|^2$ and $P_{\mathrm{B}} = |\psi_{\mathrm{B}}|^2$. From this equation it is clear that the outcome of the two-slit experiment is given by the sum of outcomes from each slit alone, plus an additional interference term.

Due to the inherent structure of any wave theory, Born's rule always bounds the complexity of any effect involving superpositions of an arbitrary number of wavefunctions to a sum of terms denoting the interference between pairs of wavefunctions [103]. For instance, in accordance with Born's rule, the interference pattern obtained in a three-slit experiment can be described by the following probabilities

$$P_{\mathrm{ABC}} = P_{\mathrm{AB}} + P_{\mathrm{BC}} + P_{\mathrm{AC}} - P_{\mathrm{A}} - P_{\mathrm{B}} - P_{\mathrm{C}}. \tag{4.2}$$

Note that this expression does not include a probability term that involves three slits, but is entirely described by probabilities involving only one and two slits. Any possible contribution from higher-order interference terms (i.e., a path involving the three slits) has been quantified by the so-called Sorkin parameter [103, 104]

$$\epsilon = P_{\mathrm{ABC}} - P_{\mathrm{AB}} - P_{\mathrm{BC}} - P_{\mathrm{AC}} + P_{\mathrm{A}} + P_{\mathrm{B}} + P_{\mathrm{C}}, \tag{4.3}$$

which should be identically zero if only the direct paths through the three individual slits are considered. Sinha *et al.* [104] showed that ϵ can be evaluated experimentally by making a set of measurements for each term in Eq. (4.3).

Although it might appear that the measurement of a non-zero ϵ implies a clear violation of quantum mechanics [104], De Raedt *et al.* demonstrated by numerically solving Maxwell's equations that a non-zero value of ϵ can exist without such violation [105]. Later it was found that this result is a consequence of the presence of exotic looped trajectories of light (e.g. red curve in Fig. 4.1a) that arise in the Feynman path integral formulation with extremely low probability of occurrence [106]. This interpretation was subsequently shown to agree with the exact numerical solution of the wave equation [107].

In this work we demonstrate that looped trajectories of photons are physically due to the near-field component of the wavefunction, which leads to an interaction among the three slits. As such, it is possible to increase the probability of occurrence of these trajectories by controlling the strength and spatial distribution of the electromagnetic near-fields around the slits. By a proper control of the conditions in a three-slit experiment, we successfully demonstrate a dramatic increase of the probability of photons to follow looped trajectories, and present the first successful measurement of a non-zero value of ϵ.

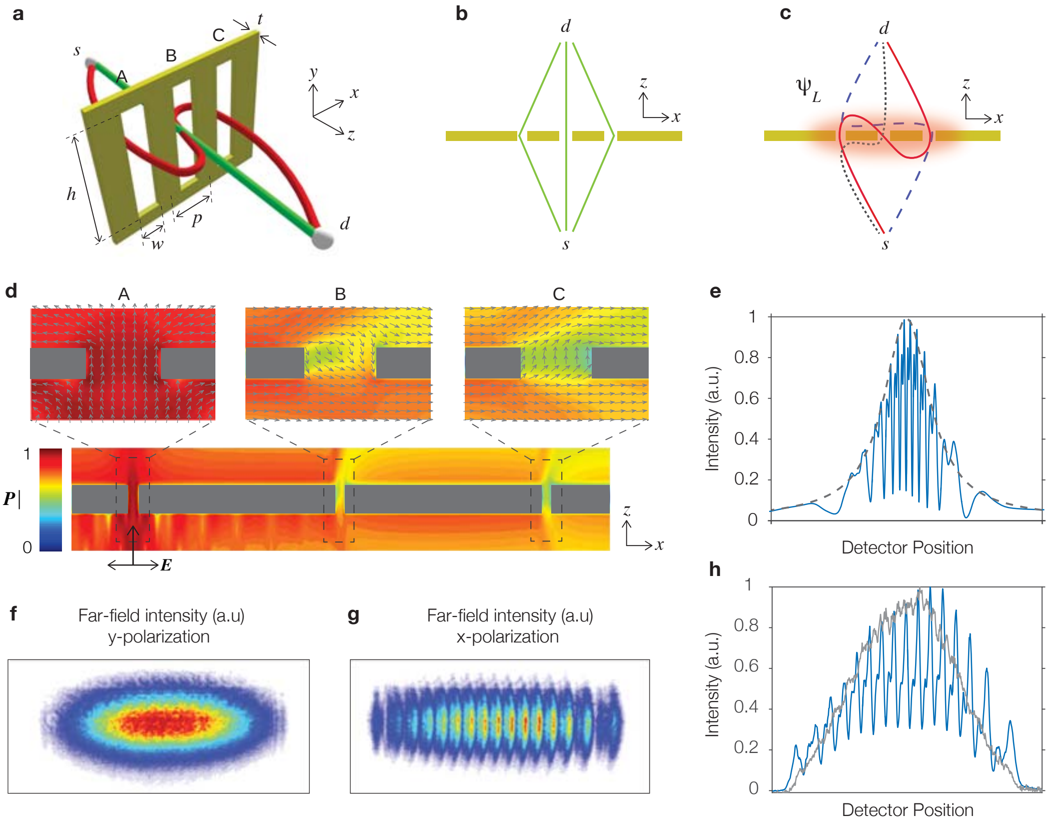

FIGURE 4.1: Trajectories of light in a three-slit interferometer. a) The three-slit structure considered in this study. The red path going from point s to point d illustrates a possible looped trajectory of light. b) Direct trajectories of light resulting from considering only the first term in Eq. (4.8). c) Examples of exotic looped trajectories arising from the higher order terms in Eq. (4.8). The red cloud in the vicinity of the slits depicts the near-field distribution, which increases the probability of photons to follow looped trajectories. d) Normalized Poynting vector $\mathbf{P}$ in the vicinity of the three slits obtained through full wave simulations at a wavelength $\lambda = 810$ nm, using a slit width w equals to 200 nm, slit separation $p = 4.6\ \mu$m, sample thickness $t = 110$ nm, and assuming infinite height, $h = \infty$. The simulations consider a Gaussian beam excitation polarized along x, and focused onto slit A. The Poynting vector clearly exhibits a looped trajectory such as the solid path in (c). e) Far-field interference patterns calculated under x-polarized (solid) and y-polarized (dashed) optical excitation. Interference fringes are formed in the far field only when strong near fields are excited (x-polarization). f) Experimental evidence that shows the far-field pattern for a situation in which only one slit is illuminated with y-polarized heralded single-photons. g) The presence of exotic looped trajectories leads to an increase in the visibility of the far-field pattern. This effect is observed when x-polarized light illuminates one of the slits. **h,** The transverse profile of the patterns shown in (f) and (g).

4.3 Theory

4.3.1 Origin of the looped trajectories of photons

Under the scalar wave approximation, the propagation of light is described by the Helmholtz equation

$$\left(\nabla^2 + k^2\right)\psi(\mathbf{r}) = 0, \tag{4.4}$$

subject to the boundary conditions specifying the physical setup. This equation can be solved by computing the propagation from any point $\mathbf{r}_1$ to any other point $\mathbf{r}_2$ via the Green's function kernel, which according to Rayleigh-Sommerfeld theory is given by

$$K(\mathbf{r}_1, \mathbf{r}_2) = \frac{k}{2\pi i}\,\frac{e^{ik\ |\mathbf{r}_1-\mathbf{r}_2|}}{|\mathbf{r}_1 - \mathbf{r}_2|}\chi, \tag{4.5}$$

where χ is an obliquity factor [108]. This equation satisfies Eq. (4.4) and the Fresnel-Huygens principle in the form of the following propagator relation

$$K(\mathbf{r}_1, \mathbf{r}_3) = \int d\mathbf{r}_2 K(\mathbf{r}_1, \mathbf{r}_2) K(\mathbf{r}_2, \mathbf{r}_3). \tag{4.6}$$

If one repeatedly applies Eq. (4.6), the path-integral formulation of the propagation kernel is obtained in the form [109]

$$K(\mathbf{r}_1, \mathbf{r}_2) = \int \mathcal{D}[x(\mathbf{s})] \exp\left(ik \int d\mathbf{s}\right), \tag{4.7}$$

where $\int \mathcal{D}[x(\mathbf{s})]$ is the functional integration over paths $x(\mathbf{s})$. The boundary conditions can be included by restricting the possible paths $x(\mathbf{s})$. If one is concerned only with diffraction from slits in a single plane, then Eq. (4.7) can be perturbatively expanded as [106]

$$K = K_1 + K_2 + K_3 + \cdots, \tag{4.8}$$

where K_n represents the nth application of Eq. (4.6) and each integration is carried over the plane containing the slits.

Solving the wave equation taking $K = K_1$ is equivalent to considering only direct paths, such as the paths in Fig. 4.1b. These paths propagate from the source and through one of the slits to the detector. We call these wavefunctions ψ_{A}, ψ_{B} and ψ_{C}. The higher-order terms in Eq. (4.8) are responsible for the looped trajectories of photons that propagate from the source to a slit, and to at least one other slit before propagating to the detector (see Fig. 4.1c). It follows that the wavefunction of a photon passing through the three slits is given by

$$\psi_{\mathrm{ABC}} = \psi_{\mathrm{A}} + \psi_{\mathrm{B}} + \psi_{\mathrm{C}} + \psi_{\mathrm{L}}, \tag{4.9}$$

where ψ_{L} represents the contribution of the looped trajectories to the wavefunction ψ_{ABC}. Note that in general ϵ, as defined by Eq. (4.3), is not zero because of the existence of these looped trajectories. Thus, the presence of looped paths leads to an apparent deviation of the superposition principle [106].

4.3.2 Occurrence of looped trajectories of photons

The conclusion that ψ_{ABC} is not simply the superposition of the wavefunctions ψ_{A}, ψ_{B}, and ψ_{C} is a consequence of the actual boundary conditions in a three-slit structure. Changing the boundary conditions affects the near-field components around the slits, but it typically does not affect the far-field distribution because of the short range extension of the near fields [110]. As shown below, the looped trajectories of photons are physically due to the near-field components of the wavefunction. Therefore, by controlling the strengths and the spatial distributions of the near-fields around the slits, it is possible to drastically increase the probability of photons to undergo looped trajectories, thereby allowing a straightforward visualization of their effect in the far-field interference pattern. To demonstrate this phenomenon, a three-slit structure was designed such that it supports surface plasmons, which are strongly confined electromagnetic fields that can exist at the surface of metals [10, 111]. The existence of these surface waves results in near fields that extend over the entire region covering the three slits [112, 98], thereby increasing the probability of looped trajectories.

As a concrete example, we consider the situations depicted in Fig. 4.1d and 4.1e. First, we assume a situation in which the incident optical field is a Gaussian beam polarized along the long axis of the slit (y polarization) and focused to a 400-nm spot size onto the left-most slit. For this polarization, surface plasmons are not appreciably excited and the resulting far-field distribution is the typical envelope, with no fringes, indicated by the dashed curve in Fig. 4.1e. This intensity distribution is described by the quantity $|\psi_{\mathrm{A}}|^2$. The presented results were obtained through a full-wave numerical analysis based on the finite-difference-time-domain (FDTD) method, on a structure with dimensions $w = 200$ nm, $p = 4.6$ μm, and $t = 110$ nm and at a wavelength $\lambda = 810$ nm (see section 4.5). The height of the slit, h, was assumed to be infinite. Interestingly, the situation is very different when the incident optical field is polarized along the x direction. The Poynting vector for this situation is shown in Fig. 4.1d. This result shows that the Poynting vector predominantly follows a looped trajectory such as that schematically represented by the solid path in Fig. 4.1c. The resulting far-field interference pattern, shown as the solid curve in Fig. 4.1e, is an example of the interference between a straight trajectory and a looped trajectory. Thus, it is clear that the naive formulation of the superposition principle does not provide an accurate description for the case where near fields are strongly excited.

4.4 Experimental implementation

First, we experimentally verify the role that looped trajectories have in the formation of interference fringes. For this purpose we exclusively illuminate one of the three slits. This experiment is carried out in the setup shown in Fig. 4.2a. As shown in Fig. 4.1f, no interference fringes are formed when heralded single-photons illuminating the slit are y-polarized. Remarkably, when the illuminating photons are polarized along the x direction the visibility of the far-field pattern is dramatically increased, see Fig. 4.1g and h. This effect unveils the presence of looped trajectories. In our experiment, the contributions from looped trajectories are quantified through the Sorkin parameter by measuring the terms in Eq. (4.3). To this end, we measured the interference patterns resulting from the seven arrangements of slits depicted in Fig. 4.2b, thus the illumination field fills each arrangement of slits. In our experiment we use heralded single-photons with wavelength of 810 nm produced via degenerate parametric down-conversion (see section 4.5). The single photons were weakly focused onto the sample, and the transmitted photons were collected and collimated by an infinity-corrected microscope objective (see Fig. 4.2c). The resulting interference pattern was magnified using a telescope and recorded using an intensified charge-coupled device (ICCD) camera, which was triggered by the detection event of the heralding photon [113]. The strength of the near fields in the vicinity of the slits was controlled by either exciting or not exciting surface plasmons on the structure through proper polarization selection of the incident photons.

The scanning electron microscope images of the fabricated slits are shown in the first row of Fig. 4.3. The dimensions of the slits are the same as those used for the simulation in Fig. 4.1, with $h = 100$ μm being much larger than the beam spot size (~ 15 μm). The interference patterns obtained when the contribution

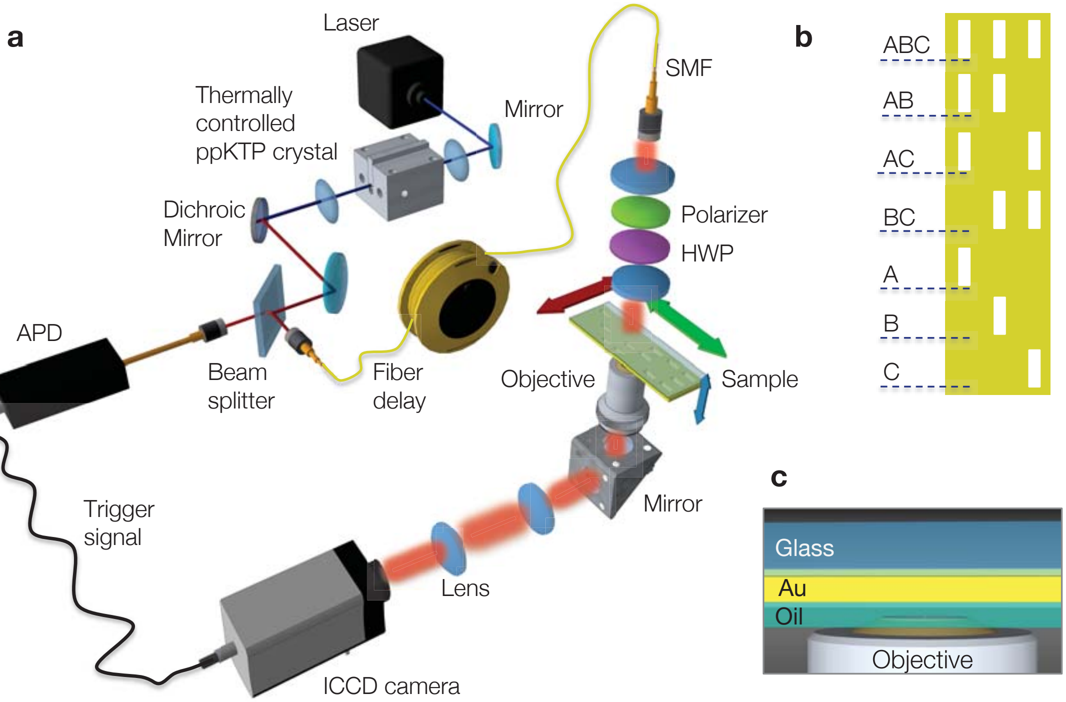

FIGURE 4.2: Experimental setup utilized to measure exotic trajectories of light. a) Sketch of the experimental setup used to measure the far-field interference patterns for the various slit configurations. b) The seven different slit arrangements used in our study. This drawing is not to scale; in the actual experiment each slit structure was well separated from its neighbours to avoid undesired cross talk. c) Detail of the structure mounted on the setup. The refractive index of the immersion oil matches that of the glass substrate creating a symmetric index environment around the gold film.

from near-field effects is negligible (y polarization) are shown in the second row, while those obtained in the presence of a strong near fields in the vicinity of the slits (x polarization) are shown in the third row. These interference patterns are obtained by adding 60 background-subtracted frames, each of which is captured within a coincidence window of 7 nsec over an exposure time of 160 sec (see insets in Fig. 4.3). Only the pattern for P_{AB} is shown in Fig. 4.3 because P_{AB} and P_{BC} produce nearly identical patterns in the far field, a similar situation occurs for P_{A}, P_{B} and P_{C}. The bottom panels show detail views of the interference patterns measured along an horizontal line.

Note that the intensities of the interference patterns (i.e., the probability amplitudes) for the two polarizations scale differently for each arrangement of slits. This is shown by the ratios of the position-averaged probabilities, P_x/P_y, indicated at the bottom of Fig. 4.3. The significant changes in the probabilities obtained with x-polarized photons ultimately lead to a value of ϵ that significantly deviate from zero. This interesting effect is produced by constructive and destructive interference among looped trajectories, whose probability has been increased through the enhancement of the near fields.

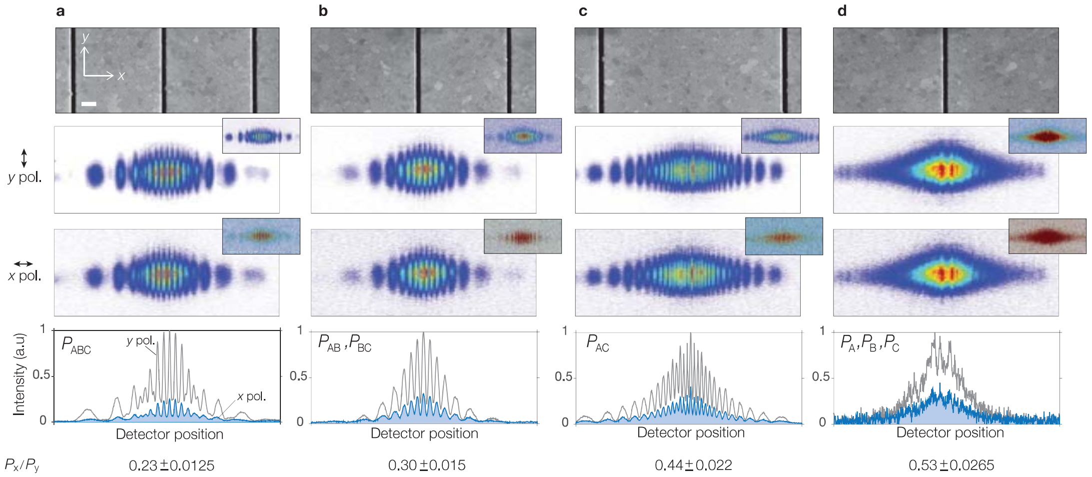

FIGURE 4.3: Experimental results. a-d) Measured interference patterns corresponding to the various probability terms in Eq. (4.3) (indicated as a label within each panel of the bottom). In this case the illumination field fills each arrangement of slits. The first row shows scanning electron microscope images of the slits used for the measurements, the scale bar represents 500 nm. The second and third panels show, respectively, the background-subtracted interference patterns formed when 60 frames, such as those in the insets are added, for the situations in which the probabilities of looped trajectories are negligible (using y-polarized illumination), and when such probabilities are increased due to the enhancement of near fields (using x-polarized illumination). Each of the frames shown in the insets was taken with an ICCD camera using heralded single-photons as a source. The bottom show the intensity dependence of the interference pattern measured along a horizontal line on the second and third panels. The ratio of the average probabilities obtained using x-polarized illumination to those obtained using y-polarized illumination, P_x/P_y, is shown at the bottom. All the measurements are conducted at a wavelength $\lambda = 810$ nm, and using structures with dimensions $w = 200$ nm, $h = 100$ μm and $p = 4.6$ μm

4.5 Methods

4.5.1 Sample design

Full-wave electromagnetic simulations were conducted using a Maxwell's equation solver based on the finite difference time domain method (Lumerical FDTD). The dispersion of the materials composing the structure was taken into account by using their frequency-dependent permittivities. The permittivity of the gold film was obtained from Ref. [114], the permittivity of the glass substrate (BK7) was taken from the manufacturer's specifications, and the permittivity of the index matching fluid (Cargille oil Type B 16484) was obtained by extrapolation from the manufacturer's specification.

4.5.2 Sample fabrication

The glass substrates are standard BK7 cover slips (SCHOTT multipurpose glass D 263 T eco Thin Glass) with a thickness of $\sim 170\mu$m, polished on both sides to optical quality. The substrate was ultrasonically cleaned for 2 hours in 2% Hellmanex III alkaline concentrate solution and subsequently rinsed and sonicated in MEK denatured Ethanol and then in demineralized water. The gold films were evaporated directly onto the clean glass substrates with no additional adhesive layer using a Plassys MEB 550S e-beam evaporation system. The growth of the film thickness was monitored in-situ during the evaporation by a water cooled quartz micro-balance. The slit patterns were structured by Ga ion beam milling using a Tescan Lyra 3 GMU SEM/FIB system with a canion FIB column from Orsay Physics. Each slit pattern consisted of 100μm long slits. While fabricating the different slit sets, proper focusing of the FIB was checked by small test millings and if needed the FIB settings were readjusted accordingly to provide a consistent and reproducible slit quality.

4.5.3 Experimental method

We generate single photons by means of heralding a photon by a "partner" photon detection from a photon pair source. The photon pairs were created in a spontaneous parametric down conversion process using a 2-mm-long type-I nonlinear crystal (periodically poled potassium titanyl phosphate (ppKTP)). We pump the crystal with a blue 405 nm continuous-wave diode laser (∼200 mW), thereby creating degenerate photon pairs at 810 nm wavelength. Both photons are passed through a 3 nm band-pass filter, coupled into a single-mode fibre and split by a 50/50-fibre beams splitter, which led to a coincidence count rate of approximately 40 kHz. The heralding photon is detected with a single-photon avalanche photo diode. Its partner photon is delayed by a 22-m-long fibre, send through the setup and imaged by an ICCD. The ICCD is operated in the external triggering mode (7 nsec coincidence gate time), where the heralding detection signal is used as an external trigger, to ensure that only these single photon events are registered [113]. Note that due to the low coincidence count rate there is only one photon at a time in the experimental setup. For experiments using a weak laser instead of heralded single photons, the ICCD was operated in the continuous mode, where the intensifier is permanently switched on.

For the case in which we used single photons, the idler photons are detected by a single-photon avalanche photo diode (APD) that heralds the detection of signal photons with an ICCD. We used either y- or x-polarized light which is selected by means of a polarizer and half-wave plate. The beam is weakly focused onto the arrangement of slits that is mounted on a motorized three-axis translation stage that can be displaced in small increments of 60 nm. An infinity-corrected oil-immersion microscope objective (NA=1.4, magnification of 60×, working distance of 100 μm) was used to collect the light emerging from the slit patterns. The light collected by the objective was then magnified with a telescope and measured by an ICCD camera.

4.5.4 Data analysis

The background subtracted interference patterns were used to determine the magnitudes of κ shown in Fig. 4.4. In Fig. 4.4a, we show the values of κ, obtained in the single photon regime, for different positions of the detector. The deviation from the theory and the magnitude of the error bars are larger at the edges of the κ profile because the signal is low at the edges of the interference patters, which results in a noisier signal. On the other hand, the central maximum of the interference patterns permits a more reliable characterization of κ. The values of κ obtained for classical light as a function of the wavelength, shown in Fig. 4.4b and 4.4c, were calculated using central maximum of the interference patterns. For these cases, we used only the regions of central fringe having intensities within 70% of the peak value. The data was then used to obtain the mean value and standard deviations for κ.

4.6 Results and discussion

We quantify the contribution from the looped trajectories through the normalized Sorkin parameter, defined as $\kappa \equiv \epsilon/I_{\max}$ with $I_{\max}$ being the intensity at the central maximum of the three-slit interference pattern [106]. Both theoretical and experimental values of this parameter are shown in Fig. 4.4a. The theoretical values were obtained via FDTD simulations, while the experimental values were calculated

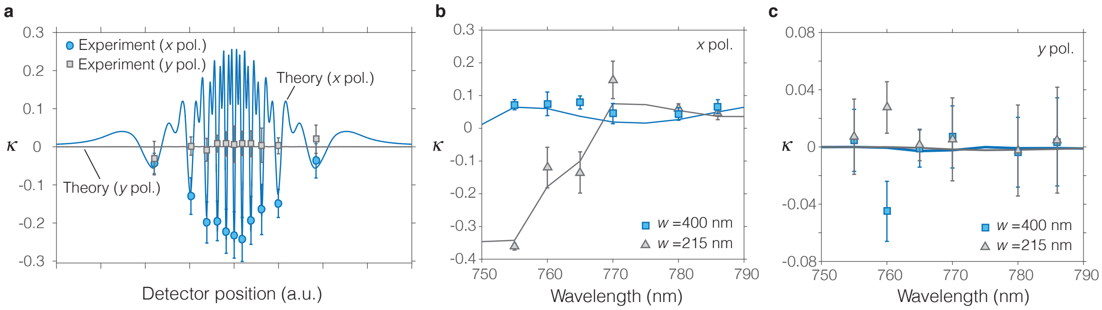

FIGURE 4.4: Quantifying the contribution of looped trajectories through the normalized Sorkin parameter, κ. a) shows numerical and experimental results, for a sample with $w = 200$ nm, $h = 100$ μm and $p = 4.6$ μm and an illuminating field consisting of heralded single-photons at a wavelength of 810 nm. The experimental points are obtained by measuring κ at different peaks of the interference patterns shown in Fig. 3. b) shows theoretical and experimental evidence at the central maximum for different widths and for various wavelengths for an attenuated laser diode, in this case the contributions from looped paths makes the κ different from zero. c) shows a situation in which looped trajectories are not enhanced and consequently κ is almost zero. These results confirm that the strengths of looped trajectories can be controlled by engineering the size of the slits and the wavelength of the illuminating field. These values of κ were measured at the centre of the interference pattern. The error bars represent the standard deviation over the ensemble of measurements. The labels x and y indicate the polarization state of the incident light.

from the results in Fig. 4.3. Clearly, we observe that when the near fields are *not* enhanced, the parameter κ is much smaller than the uncertainty associated with our measurements. However, when the near fields are enhanced, κ is dramatically increased due to the increased probability for the looped trajectories [106], enabling the measurement of this parameter despite experimental uncertainties. Taking as a reference the central maximum of the κ profile, the experimental results indicate that the contribution of looped trajectories has been increased by almost two orders of magnitude.

Finally, we show that it is possible to control the probability of photons undergoing looped trajectories by modifying the dimensions of the three slit structure or by changing the wavelength of the optical excitation. Fig. 4.4b and 4.4c show theoretical predictions and experimental data at the central maximum for different slit parameters and wavelengths. These measurements were taken with classical light from a tunable diode laser. Fig. 4.4b shows the normalized Sorkin parameter for a situation in which looped trajectories significantly contribute to the formation of interference fringes, whereas Fig. 4.4c shows the same parameter for a situation in which near-field effects, and consequently looped trajectories, are negligible. In general, we note that the theoretical and experimental results are in good agreement, with the observed discrepancies being attributed to experimental uncertainties due to imperfections in the fabricated sample and due to the limited dynamic range of the camera.

4.7 Conclusion

We have demonstrated that exotic looped paths occur as a physical consequence of the near-field component of the wave equation. As such, it is possible to control the probability of occurrence of such paths by controlling the strength and spatial distribution of the near-fields around the slits. By doing so, we have shown a drastic increase in the probability of photons to follow looped paths, leading to the first experimental observation of such exotic trajectories in the formation of interference fringes. Our work elucidates new properties of light that could be used to enrich protocols that rely on interference effects such as quantum random walks and quantum simulators [95, 115].

Chapter 5

Measurement of the Photon-Plasmon Coupling Phase Shift

This chapter is based on the following paper:

A. Safari, R. Fickler, E. Giese, O. Magaña-Loaiza, R. W. Boyd and I. De Leon (Accepted in *Physical Review Letters*).

Author contributions: A. Safari and R. Fickler conducted the experiment with initial assistance from I. De Leon and O. Magaña-Loaiza. A. Safari analyzed the data and I. De Leon performed the numerical simulation. The theoretical model was developed by E. Giese and A. Safari. A. Safari wrote the manuscript with help from E. Giese. All authors discussed the results and commented on the manuscript. R. W. Boyd and I. De Leon supervised all aspects of the project.

5.1 Abstract

Scattering processes have played a crucial role in the development of quantum theory. In the field of optics, scattering phase shifts have been utilized to unveil interesting forms of light-matter interactions. Here we investigate the phase shift experienced by a single photon as it scatters into a surface plasmon polariton and vice versa. This coupling phase shift is of particular relevance for quantum plasmonic experiments. Therefore, we demonstrate that the photon-plasmon interaction at a plasmonic slit can be modeled through a quantum-mechanical *tritter*, a six-port scattering element. We show that the visibilities of a double-slit and a triple-slit interference patterns are convenient observables to characterize the interaction at a slit and determine the coupling phase. Our accurate and simple model of the interaction, validated by simulations and experiments, has important implications not only for quantum plasmonic interference effects, but is also advantageous to classical applications.

5.2 Introduction

Light can couple to collective charge oscillations at the interface between a metal and a dielectric, forming surface electromagnetic waves that propagate along the interface [10]. Such surface waves, referred to as surface plasmon-polaritons (SPPs), exhibit remarkable properties that make them suitable for a variety of applications [116, 117, 118, 119, 120]. Since SPPs show intriguing non-classical effects, there is growing interest in the application of SPPs in quantum systems [121]. Since SPPs preserve both entanglement and photon number statistics [122, 123, 124], they constitute an alternative for on-chip quantum circuitry. Although SPPs are formed from photons (bosons) and electrons (fermions), they exhibit a bosonic behavior in the limit of many electrons [125]. Therefore, two indistinguishable SPPs interfering at a plasmonic beam splitter can bunch and show the Hong-Ou-Mandel (HOM) effect [126, 127]. In contrast to their all-optical counterpart, plasmonic beam splitters are lossy. However, these intrinsic losses can be beneficially used to e.g. adjust the phase shift imprinted by a plasmonic beam splitter such that the two SPPs antibunch [128], in contrast to the conventional HOM bunching.

Similar to a scattering process, the electromagnetic field experiences a phase jump during coupling to SPPs. Determining this coupling phase and characterizing the complex photon-plasmon coupling amplitude is of great importance in designing experiments that contain quantum features. In fact, this coupling phase, also known as the scattering phase shift, is intrinsic to any scattering phenomena; a wavepacket scattering off a potential acquires a phase shift, and consequently a time delay known as the Wigner delay [129, 130, 131]. In plasmonic systems, this phase has been measured by employing special techniques to image SPPs directly [132, 133] or using several double-slit structures with different slit separations [134]. However, some inconsistencies can be seen in the literature; while some theoretical models predict a constant scattering phase shift [135, 136, 137], numerical simulations and experimental measurements have shown significant deviations from the predicted phase shift [134, 138, 139, 132, 140].

In this chapter, we show that the visibility of the unique interference pattern of a plasmonic triple-slit is a convenient observable from which the photon-plasmon coupling phase jump can be inferred. The advantage of measuring the visibility is its insensitivity to some experimental errors such as imperfect imaging. However, in a double-slit experiment, the visibility is independent of the coupling phase as it only appears as a transverse shift of the interference pattern. Therefore, we use a combination of double- and triple-slit structures to characterize the complex photon-plasmon coupling amplitude. As for the quantum mechanical description of the structure, we demonstrate that each slit on a plasmonic layer can be modeled by a tritter, i.e. a device that couples three input to three output modes. Finally, we verify the accuracy of our analysis by performing a numerical simulation. Such a simple and accurate model is beneficial for future quantum plasmonic experiments.

5.3 Theory

Multiple-slit experiments lie at the heart of fundamental quantum mechanics. For example, double-slit experiments play an important role in revealing and understanding the wave-particle duality [141]. Triple-slit interference patterns have been used to test the validity of Born's rule [142, 143, 144, 145], one of the foundations of quantum physics. A triple-slit structure on a metallic film reveals that an additional coupling of the slits through the SPP modes leads to exotic trajectories of the pointing vector through the slit configuration and modifies the pattern, still in agreement with Born's rule [92]. Moreover, plasmonic slits are used to perform weak measurements [146] and to control the spatial coherence of light [147, 148, 149, 150]. Therefore, having an accurate and simple model for the coupling process at plasmonic slits can have important fundamental and practical implications.

In contrast to the two-mode coupling typically observed in recent quantum plasmonics experiments [126, 127], illuminating a single slit in a metallic surface can lead to a three-mode interaction, where the light field couples to two SPP modes, each of them on either side of the slit, or is transmitted through the slit, see Fig. **??** (a). For a quantum description, we model each slit by a six-port element, a *tritter* [151, 152, 153], as a generalization of and in analogy to a beam splitter. Such elements play a crucial role for many-particle and high-dimensional quantum communication and computation [154, 155, 156]. In most implementations a tritter is composed of beam splitters within a complex setup [152] or custom-tailored

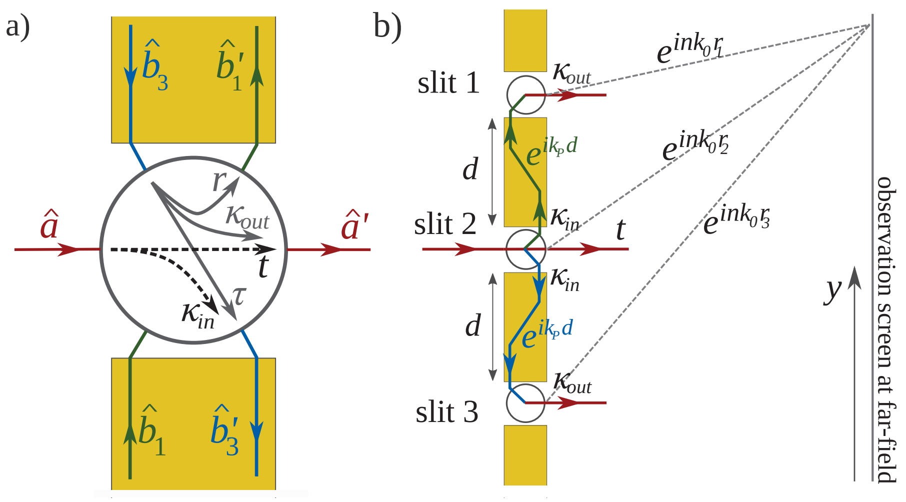

FIGURE 5.1: Illustration of plasmonic tritters. a) Sketch of a slit on a gold film that acts as a tritter. The input field couples into two plasmonic modes each with a complex probability amplitude κ_{in}. A plasmonic mode propagating towards a slit can either reflect back, tunnel through the slit, or scatter into photons with probability amplitudes r, τ, and κ_{out}, respectively. For clarity, we only show the coupling of one plasmonic mode. The other mode couples in a similar manner. b) Schematic diagram of the triple-slit structure where each slit acts as a tritter. The middle-slit is illuminated with single photons. The SPPs propagating from the middle-slit towards the outer slits acquire a factor of e^{ik_Pd}. The distance from slit j to the screen at the far-field is shown by r_j.

with integrated waveguide structures [157, 154, 155, 156], whereas the three-mode interaction at a plasmonic slit happens quite naturally.

We introduce the six-port coupling matrix of a tritter to model the plasmonic slit and denote the input modes through the annihilation operators $\hat{a}$, $\hat{b}_1$, and $\hat{b}_3$ of the light field as well as two SPPs, respectively. We require the annihilation operators to fulfill the bosonic commutation relations. These operators are connected to the respective output modes $\hat{a}'$, $\hat{b}_1'$, and $\hat{b}_3'$ through the transformation

$$\begin{pmatrix} \hat{b}_1' \\ \hat{a}' \\ \hat{b}_3' \end{pmatrix} = \begin{pmatrix} \tau & \kappa_{\text{in}} & r \\ \kappa_{\text{out}} & t & \kappa_{\text{out}} \\ r & \kappa_{\text{in}} & \tau \end{pmatrix} \begin{pmatrix} \hat{b}_1 \\ \hat{a} \\ \hat{b}_3 \end{pmatrix} \tag{5.1}$$

in the Heisenberg picture, see Fig. 5.1 (a). Note that even though the elements of this matrix may be complex, the matrix itself has to be unitary to preserve the bosonic commutation relation and by that to conserve energy. We have also assumed that the coupling of the photon to the two SPP modes is symmetric. We perform our study at a single-photon level to lay the basis for future experiments with plasmonic slits in the quantum regime. We emphasize that at a single-photon level and to observe quantum effects such a description is necessary. However, since we only measure first moments, the same results could be obtained by using a classical light source, i.e. a laser.

To investigate the validity of our description and to determine some of the matrix elements of Eq. (5.1), we use a triple-slit arrangement to make use of all three output channels. In general, the interference pattern generated by a triple-slit, which is essentially generated through three-path interference, can be described by the relation

$$\begin{aligned} I = & I_1 + I_2 + I_3 + 2\sqrt{I_1 I_2}\cos\phi_{12} \\ & + 2\sqrt{I_2 I_3}\cos\phi_{32} + 2\sqrt{I_1 I_3}\cos\phi_{13}, \end{aligned} \tag{5.2}$$

where I_j is the intensity of the light emerging from slit j and ϕ_{ij} is the phase difference between path i and path j, see Fig. 5.1 (b).

We focus on the case where only the middle slit (slit 2) is illuminated by single photons. An interference pattern forms at the far-field which can be understood by the following analysis: The photons are either coupled to two SPP modes or are transmitted through the slit. The transmission probability is $|t|^2 = I_2$ and corresponds to the normalized transmitted intensity of slit 2. The probability to couple to each plasmonic mode is $|\kappa_{\text{in}}|^2$. During the coupling process, the generated SPPs pick up a phase $\phi_{\text{in}} = \arg\kappa_{\text{in}}$. The losses inside the plasmonic material could be modeled by a beam splitter transformation that couples to a vacuum. However, since we are interested only in first-order moments, it is sufficient to multiply each SPP state with a factor $e^{ik_P d}$ to describe the propagation between the slits. Here, d is the shortest distance between the outer slits and the centre slit, and $k_P = k'_P + ik''_P$ is the complex wavenumber of the SPPs. When the SPPs reach the outer two slits, they can be scattered into a photonic mode with a probability of $|\kappa_{out}|^2$ and pick up a phase $\phi_{\text{out}} = \arg\kappa_{\text{out}}$. Hence, we find $I_1 = I_3 = |\kappa_{\text{in}}|^2 \exp(-2k''_P d)|\kappa_{\text{out}}|^2$ for the intensity output of slits 1 and 3. From each slit the photons propagate to the screen, which gives an additional phase factor of $\exp(ink_0 r_j)$, where r_j is the distance from slit j to the observation point on the screen and $n = 1.52$ is the refractive index of the index-matching oil and the glass used in our microscope setup. Hence, the phase differences in Eq. (5.2) are given by

$$\phi_{j2} = k'_P d + \phi_{\text{in}} + \phi_{\text{out}} + nk_0(r_j - r_2) \tag{5.3}$$

for $j = 1, 3$ and

$$\phi_{13} = \phi_{12} - \phi_{32}. \tag{5.4}$$

We demonstrate in the following that we can extract the contribution $\phi_{in} + \phi_{out}$ from the visibility of a triple-slit interference pattern.

5.4 Experimental implementation

As shown in Fig. 5.2, our sample contains two different double-slit structures (A) and (B) with a slit separation of $d = 4.43\,\mu\text{m}$ and $9.05\,\mu\text{m}$, respectively, and a triple-slit structure (C) with a slit separation of $d = 4.43\,\mu\text{m}$. The sample is made of a 110-nm-thick gold film deposited on a glass substrate whose thickness is $\sim 170\,\mu\text{m}$. The complex wavenumber of the SPPs is given by [10]

$$k_P = k'_P + ik''_P = k_0\sqrt{\frac{\epsilon_d \epsilon_m}{\epsilon_d + \epsilon_m}}, \tag{5.5}$$

where k_0 is the photon wavenumber in vacuum, and ϵ_d and ϵ_m are the complex relative dielectric constants of the dielectric and metal, respectively. These values are tabulated in Palik's compendium [158] from which we obtain $k_P = 1.22 \times 10^7 + 3.39 \times 10^4 i$ for gold-glass interface at 810 nm as used in our experiment. Note that the film is thick enough to avoid coupling between the SPP modes excited on the top and bottom surfaces of the film [10]. In our experiments, we illuminate one of the slits with heralded single photons focused by a microscope objective on

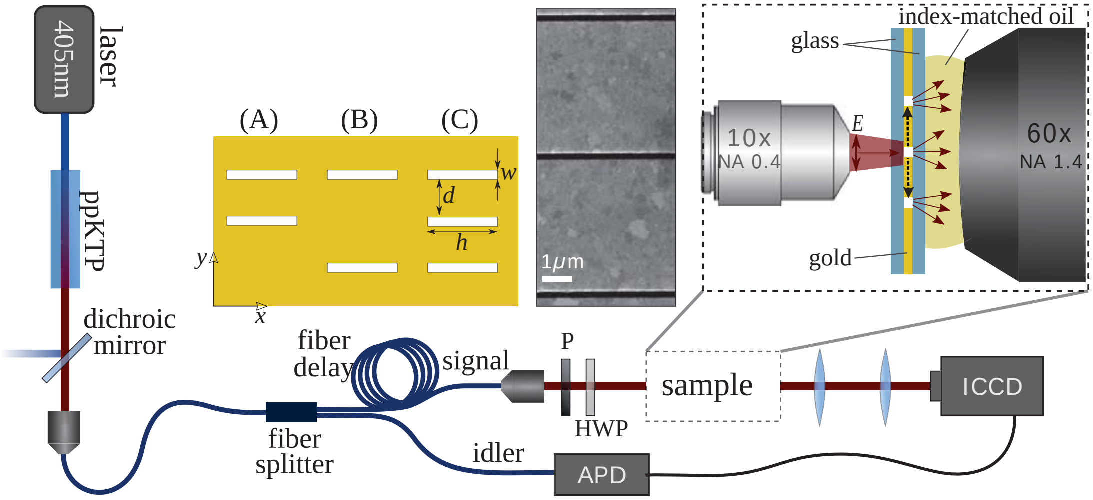

FIGURE 5.2: Scheme of the experimental setup. A 405-nm laser pumps a nonlinear ppKTP crystal to generate the signal-idler pairs through the process of SPDC. The idler photons are used to herald the presence of the signal photons, which are focused onto the sample by means of a microscope objective. A sketch of the sample with different slit arrangements (A), (B), and (C) is shown in the inset along with a scanning electron micrograph of the triple-slit structure of arrangement (C). The dimensions are: $w = 0.20\,\mu\text{m}$, $d = 4.43\,\mu\text{m}$, and $h = 98\,\mu\text{m}$ with an uncertainty of $\pm 0.03\,\mu\text{m}$. The polarization of the signal photons is controlled by a polarizer (P) and a half-waveplate (HWP). Photons at the far field are collected with an oil-immersion objective. A lens system images the far field pattern onto an ICCD camera.

the sample. An index-matching oil-immersion microscope objective is utilized to magnify the field distribution and an imaging system images the far field pattern onto an intensified charge-coupled device (ICCD) camera.

Our heralded single-photon source is realized using spontaneous parametric down-conversion (SPDC) in a 2-mm-long type-I periodically poled potassium titanyl phosphate (ppKTP) nonlinear crystal pumped by a 405 nm continuous wave diode laser (∼200 mW). The pairs are degenerate at a wavelength of 810 nm and pass through a 3-nm-band-pass filter before they couple into a single-mode fiber. The idler and the signal photons are separated probabilistically by means of a 50/50 fibre beam splitter. A coincidence count rate of ∼36 kHz is obtained. We detect the idler photons with a single-photon avalanche photo diode (APD) that is used to trigger the ICCD camera that registers the detection of the signal photons. To compensate for the electronic delay of the camera, we delay the signal photons by passing them through a 22-m-long fibre before we send them through the sample. The ICCD (with a 7-ns-gate-time) registers the signal photons in the far field of the slits.

The excitation of SPPs at a slit requires a transverse magnetic polarization. If the photons are polarized along the long axis of the slit (x-polarization), there is no coupling to plasmonic modes and the far-field pattern does not show any interference; see the red patterns in Fig. 5.3. However, upon rotation of the polarization of the input photons by 90 degrees an interference pattern is formed even though only one slit is illuminated [159, 160, 161]. Multiple-slit interference occurs because the SPPs excited at the illuminated slit propagate to the neighbouring slits where they scatter into photons. The measurements depicted in green in Fig. 5.3 show the interference pattern for the polarization perpendicular to the long axis of the slit (y-polarization). For the rest of the experiment we perform the measurements with y-polarized photons to excite SPPs and use the x-polarized photons only to calibrate the far field pattern.

To obtain the modulus of the photon-plasmon coupling constant of Eq. (5.1), we first measure the visibility of the double-slit structure (A). We analyze our data with Eq. (5.2) and set $I_3 = 0$. Equation (5.2) therefore reduces to a simple double-slit pattern $I = I_1 + I_2 + 2\sqrt{I_1 I_2}\cos\phi_{12}$ with a visibility of $V = 2\sqrt{I_1 I_2}/(I_1 + I_2)$. Since $I_2 = |t|^2$ and $I_1 = |\kappa_{\mathrm{in}}|^2 \exp(-2k''_P d)|\kappa_{\mathrm{out}}|^2$ with $d = 4.43\,\mu\mathrm{m}$, the visibility depends on the three coupling parameters $|t|$, $|\kappa_{in}|$, and $|\kappa_{out}|$. However, because of the unitarity of the tritter matrix we have $|t|^2 = 1 - 2|\kappa_{\mathrm{in}}|^2$. If we additionally assume reciprocity of the coupling process [153], we find $|\kappa_{\mathrm{in}}| = |\kappa_{\mathrm{out}}|$ and the visibility depends only on one free parameter.

We measure a visibility $V = 0.41 \pm 0.01$ for slit structure (A) from the interference in Fig. 5.3(A) and extract $|t| = 0.78 \pm 0.01$ and $|\kappa_{in}| = |\kappa_{out}| = 0.44 \pm 0.01$. For a consistency check, we measure the visibility of the double-slit structure (B) from the pattern shown in Fig. 5.3(B) and we obtain $V = 0.35 \pm 0.01$. The theoretical prediction based on the values determined above and with $d = 9.05\,\mu\mathrm{m}$ is $V = 0.34 \pm 0.01$, which shows a prefect agreement to our experimental result.

In a double-slit experiment, the visibility is independent of the coupling phases ϕ_{in} and ϕ_{out}, since they only appear as a transverse shift of the far-field interference pattern. Finding the zero-fringe to obtain these coupling phases in a double-slit experiment would require a perfect alignment of the camera to the centre of the structure. To avoid this difficulty and use only the visibility as an observable, we turn to a triple-slit structure (C) to measure the coupling phases. The visibility of the triple-slit pattern depends on the coupling phases because the far-field intensity has three interference contributions, as demonstrated by Eq. (5.2). We assume that the device is symmetric so that $I_1 = I_3 < I_2$, and, through use of a trigonometric

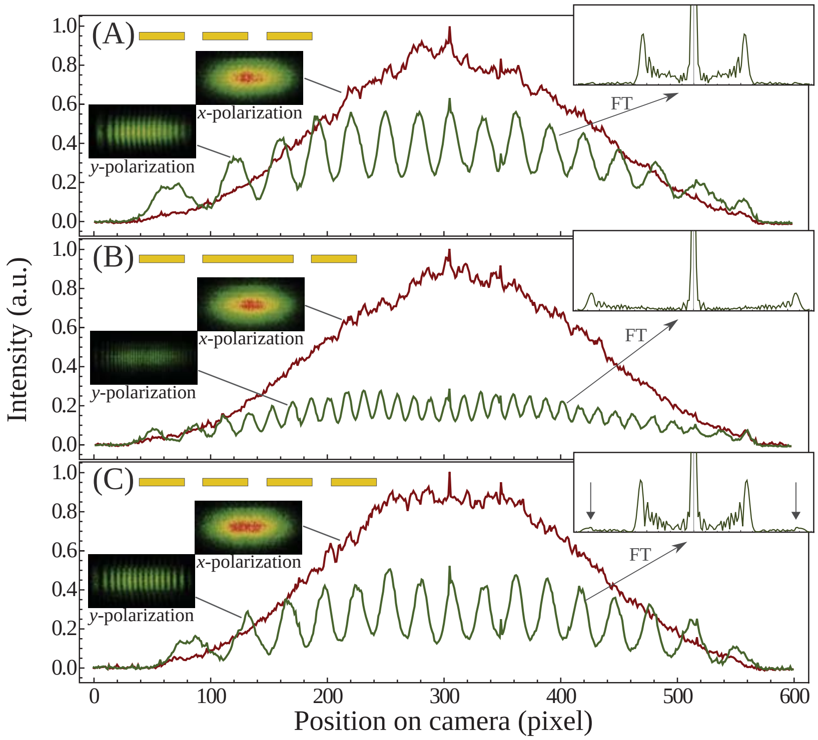

Figure 5.3: Far-field interference patterns from the three different slit structures labeled in Fig. 5.2. Only the photons with y-polarization excite SPPs (green), no interference occurs for x-polarization (red). The Fourier transforms (FT) in each part show the spatial frequency of the fringes. Since the slit separation is larger in (B) its fringe pattern has a higher spatial frequency than (A). In (C), the interference of the two modes emerging from the two outer slits has a small contribution in the triple-slit pattern as shown with the arrows on the Fourier transform.

identity, Eq. (5.2) reduces to

$$I = 2I_1 + I_2 + 4\sqrt{I_1 I_2} \cos\frac{\phi_{12}+\phi_{32}}{2} \cos\frac{\phi_{13}}{2} + 2I_1 \cos\phi_{13}, \tag{5.6}$$

where we used the definition of ϕ_{13} from Eq. (5.4). Since $\phi_{12}+\phi_{32}$ depends only weakly on the transverse position in the far-field, the first cosine in Eq. (5.6) does not vary significantly over the interference pattern. Also, the last term in Eq. (5.6) makes a small contribution as $I_1 \ll 2\sqrt{I_1 I_2}$. This conclusion can be drawn by looking at the Fourier transform of the experimental interference pattern shown in the inset of Fig. 5.3 (C); the dominant spatial frequency comes from $\cos(\phi_{13}/2)$, and the contribution of $\cos\phi_{13}$, which oscillates at twice this frequency, is negligible. Hence, the visibility is determined by $\phi_{12}+\phi_{32}$, which includes the coupling phases as well as the phase $k'_P d$.

By matching the visibility of our model to the visibility of the experimental pattern shown in Fig. 5.3 (C), we find the coupling phases to be $\phi_{\text{in}} + \phi_{\text{out}} = 5.4 \pm 0.4$ radians. Note that the main source of uncertainty comes from the measurement of the slit separation from the scanning electron micrograph in Fig. 5.2.

To test the accuracy of our theoretical model and its results, we perform a finite-difference time-domain (FDTD) simulation of the triple-slit experiment. Since the visibility of the interference pattern depends on the exact size of the beam on the illuminated slit and absolute coupling efficiencies, the visibility of the simulated pattern cannot be compared directly with that of the experiment. Therefore, we plot the far-field pattern for different slit separations d, from 4.3 µm to 4.8 µm. By comparing the results of the FDTD simulation and our theoretical model shown in Fig. 5.4, we find that the coupling phase is $\phi_{\text{in}} + \phi_{\text{out}} = 5.8 \pm 0.1$ radians. This value is in complete agreement with the coupling phase obtained from the experimental data. If we were to use a different coupling phase in our theoretical model, the

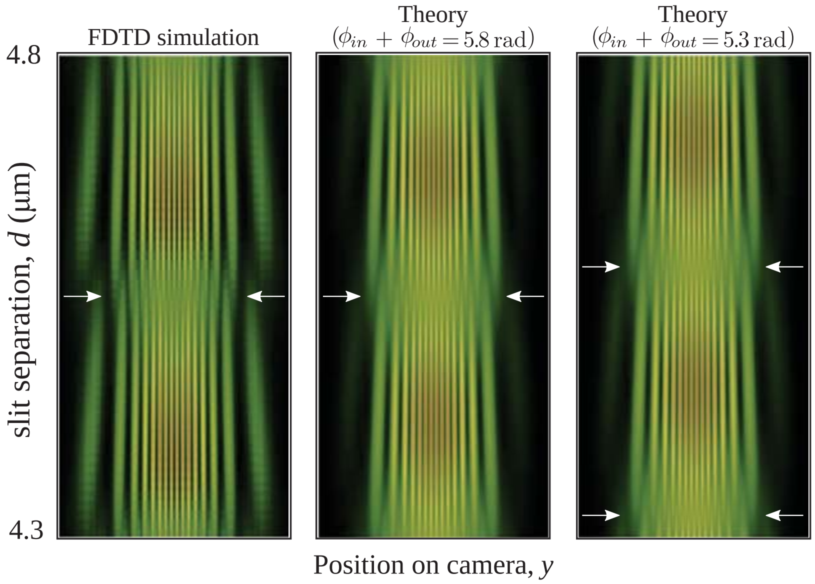

FIGURE 5.4: Far-field interference pattern for different slit separations from 4.3 μm to 4.8 μm obtained from FDTD simulation and from our theoretical model. For the theoretical plots Eq. (5.2) is multiplied by a sinc function to account for the finite width of the slits. The theoretical result matches to the numerical simulation when we incorporate a coupling phase of $\phi_{in} + \phi_{out} = 5.8$ radians. With other values of the coupling phase the position of the minimum visibility (indicated by the arrows) shifts, as shown in the rightmost plot. The excellent agreement between the simulation and the theoretical results confirms the validity of our theoretical model. The outer fringes in the theoretical plots are faint due to the deviation from the small angle approximation used for the sinc function.

position of the minimum of visibility would be shifted. As an example, Fig. 5.4 also shows the theoretical pattern with a wrong coupling phase of 5.3 radians. The minimum visibility is clearly shifted upwards and another minimum appears from the bottom of the pattern.

5.5 Conclusion

In summary, we have characterized three-mode photon-plasmon coupling phenomena at a slit by employing a simple but accurate quantum-mechanical description of a tritter. We showed that a triple-slit arrangement constitutes a convenient structure to analyze the six-port coupling matrix, and in particular to measure the phase of the coupling process. This phase jump is a generic physical phenomenon and occurs in any scattering event. Thus, our approach of directly measuring it will be of particular importance for nearly all quantum interference effects and as such important for future quantum-plasmonic experiments. In addition, the complex nature of the multi-mode photon-plasmon coupling at a slit might lead to the investigation of unique properties of multi-particle interactions [154]. In our experiments, the distance between the slits is large enough to suppress the coupling between the slits through localized modes [162]. Therefore, we only studied the coupling phase of propagating modes. However, interference between localized and propagating modes would affect the transmission spectrum of 2D arrays of holes [163]. Therefore, a measurement of the coupling phase is important to characterize the extraordinary transmission of light through 2D arrays. In this case, one has to consider in addition the SPP-SPP scattering at the holes [164, 165].

Chapter 6

Conclusion

We described a few experiments in which near-resonant light-matter interactions have been employed to enhance some effects that are typically negligible or very small. Two different material systems have been used in this thesis; rubidium atomic vapour and plasmonic structures. First we studied the propagation of light in a moving medium. As light propagates inside a moving a medium its speed changes with respect to the stationary laboratory frame according to the theory of special relativity. This effect, known as the Fizeau drag effect, is typically very small and requires the medium to be moved with a large velocity in order to be detected. For example, to observe this effect in glass P. Zeeman used a 1.2-m-long glass rod moving at 10 m/s [43]. However, a particular aspect of this phenomenon, first described by H. A. Lorentz [39], is the influence of the medium's dispersion. For a typical low-dispersion material such as glass the dispersive contribution of the drag effect is almost negligible and is considered to be a correction to the non-dispersive contribution. Using a highly dispersive material, the effect of dispersion can be orders of magnitude larger than the non-dispersive contribution. By using rubidium atoms and tuning the laser frequency between two resonances we achieved a very large dispersion (a group index as large as $n_g = 330$). Thus, by moving the vapour cell at a speed of 1 m/s we observed a change in the phase velocity of light inside the cell as large as 330 m/s. This dramatic change in the speed of light scales linearly with the group index of the medium and can be understood as the manifestation of the Doppler shift in a highly dispersive material. When the medium moves, the resonance frequency of the atomic transition shifts with respect to the frequency of the input photons. If the medium is highly dispersive, the refractive index of the medium changes significantly with the shifted frequency. Therefore, the phase velocity of the photons inside the medium depends on the speed of the medium.

An extremely large group index (even larger than one million) can be obtained using techniques such as electromagnetically induced transparency (EIT) [16, 1, 14]. Therefore, with this enhancement even a slow motion can be detected. This technique has been implemented in cold rubidium atoms to measure the speed of the atomic ensemble falling due to the gravity [166]. In a follow up experiment we are investigating the transverse light-drag effect in EIT condition. In this case, the medium moves perpendicular to the propagation direction of the laser beam and the photons are expected to experience a lateral shift. In addition, we use electromagnetically induced absorption to achieve a large negative group index. Hence, the photons are expected to move opposite to the motion of the atoms. We investigate the possibility of this upstream motion of photons for the first time.

Next we investigated the formation of caustics upon nonlinear propagation. Caustics are important as they occur naturally in all wave systems and localize the energy of waves. Formation of caustics under linear propagation condition has been the subject of study for more than two centuries. Although a simple ray picture gives the overall shape of the patterns, caustics are singularities of rays and the appropriate theory had to await the mathematics of catastrophe theory developed in 1970s [167, 168]. Despite the importance of caustics, the effect of nonlinearity on the formation of caustics is overlooked in literature. As a wave acquires a random phase fluctuation, a caustic pattern develops after some propagation distance. To develop caustics under linear propagation condition, the phase fluctuations have to be relatively large. We demonstrated that in the presence of nonlinear instability, even small fluctuations are accentuated and generate sharp caustics. This is in contrast to the claim that nonlinearity may wash out caustics by destroying the phase coherence [68].

Our results can also help with understanding some ocean phenomena such as rogue waves and tsunamis. Recent studies show that caustic focusing plays a significant role in the formation of giant oceanic waves such as tsunamis and rogue waves. Moreover, the dynamics of water waves in oceans is well described by a nonlinear Schrödinger equation similar to our system described in Chapter 3. Hence, our experiment provides a crucial step towards understanding the role of nonlinearity in the formation of these giant waves which is still under debate.

In Chapter 4 we described the first observation of looped trajectories in a multiple slit experiment in which the photons can take a path that passes through all the slits. In a multiple slit (such as double-slit and triple-slit) interference experiments it is often assumed that the wave function at the screen with all slits open is equal to the sum of the wave functions with the slits individually open one at a time. This assumption rules out the possibility of trajectories that pass through all three slits in a triple-slit arrangement. Such looped trajectories, seemingly in contradiction with the superposition principle, has been predicted previously [104], but had not been observed experimentally. In a typical multiple slit experiment the slits are not coupled and thus closing or opening a slit does not affect the field emerging from the other slits. Therefore, we implemented a triple-slit arrangement on a plasmonic layer where the slits are coupled by surface plasmon polaritons. We showed that the near-field enhancement in the vicinity of the plasmonic structure increases the probability of these looped trajectories significantly. Nonetheless, the superposition principle is not violated; one has to note that closing or opening a slit changes the boundary condition. Thus, a naive application of the superposition principle and Born's rule is insufficient.

Finally, in Chapter 5 we investigated the phase evolution of photons as they scatter into surface plasmon polaritons and vice versa. For almost a century, outstanding classical properties of plasmonic systems have been a subject of interest to many physicists. In the past few years, there has been a rapid expansion of research into the non-classical features of plasmonic systems. However, an important aspect of the coupling process regarding the phase evolution of the photons has been overlooked in the literature. We showed that photons experience a phase jump during coupling into and decoupling out of a plasmonic structure. We used the visibility of the unique interference pattern of a triple-slit structure and modeled each plasmonic slit as a quantum tritter, i.e. a beamsplitter with three input and three output ports, and measured a coupling phase jump of 5.4 ± 0.4 radians. Characterization of this coupling phase is of great importance in designing quantum plasmonic experiments. Moreover, this coupling phase, also known as the scattering phase is a generic phenomenon in all scattering events; a wavepacket scattering off a potential acquires a phase shift. Therefore, our approach allows one to characterize the scattering phase shift and its dependence on different parameters. In addition, our simple but very accurate quantum treatment of plasmonic slits can be extended to other plasmonic structures and provides an accurate theoretical model for future quantum palsmonic experiments.

Appendix A

Explicit formulas for photon number discrimination with on/off detectors

Here we describe a side project that was not part of the main body of the thesis. This appendix is based on the following paper [169]:

F. M. Miatto, A. Safari and R. W. Boyd, Applied Optics **57**, 6750 (2018). DOI:10.1364/AO.57.006750.

Author contributions: F. M. Miatto initiated the work. F. M. Miatto and A. Safari developed the theory. F. M. Miatto wrote the manuscript. All authors discussed the results and commented on the manuscript. R. W. Boyd supervised the project.

A.1 Abstract

Discriminating between Fock states with a high degree of accuracy is a desirable feature for modern applications of optical quantum information processing. A well-known alternative to sophisticated photon number discriminating detectors is to split the field among a number of simple on/off detectors and infer the desired

quantity from the measurement results. In this work we find an explicit analytical expression of the detection probability for any number of input photons, any number of on/off detectors, and we include quantum efficiency and a false count probability. This allows us to explicitly invert the conditional probability using Bayes' theorem and express the number of photons that we had at the input in the most unbiased way possible with ready-to-use formulas. We conclude with some examples.

A.2 Introduction

For practical applications of optical quantum information processing, it would be a great advantage to have a detector that can discriminate between different photon number states [170, 171]. There are currently several different solutions that allow one to achieve this to some extent [172, 173, 174, 175, 176], but the resources that such detectors require (such as very low temperatures, particular materials, and/or optical configurations) may make them costly to obtain and not straightforward to operate. There are workarounds that involve squeezing more information out of the conventional detectors [177, 178], or by demultiplexing the photons in time or space and directing them toward one or multiple single-photon detectors [179, 180, 181, 182, 183, 184, 185, 186].

The most common single-photon detectors are only able to tell us whether they detected "zero photons" or "more than zero photons." Furthermore, they are subject to noise and a sub-optimal efficiency, which means that sometimes they click when they should not have or that they do not click when they should have [187].

In this work we study photon-number discrimination by demultiplexing, and our novel contribution is explicit formulas that are straightforward to implement and that take into account quantum efficiency and noise, as well as any number of detectors.

A.3 Discrimination probability

We consider a balanced linear device that converts D inputs into D outputs. A single-mode input then becomes

$$\hat{a}^{\dagger}_{\text{in}} \rightarrow \sum_{j=1}^{D} \frac{b^{\dagger}_{j}}{\sqrt{D}}, \tag{A.1}$$

A possible physical model for this device can be a cascaded sequence of $D-1$ conventional beam splitters, with reflectivities $\frac{1}{D}$, $\frac{1}{D-1}$ $\ldots$ $\frac{1}{2}$, but other possibilities exist; for example, using a top-hat pulse with uniform spatial intensity [188], followed by an array of detectors. We note that all-optical solutions are just one area of applicability of our results, which can be applied to any demultiplexer with a final set of detectors, which can be even as large as the set of pixels in an electron multiplying charge-coupled device (EMCCD) or an intensified charge-coupled device (ICCD).

Note that a demultiplexer should avoid closed paths, because photons, being bosons, would undergo the Hong–Ou–Mandel effect and bunch together instead of spreading out into the available modes, which defeats the purpose of the demultiplexer. Furthermore, in the absence of closed paths we are not required to take phases into account and the problem reduces to a classical counting problem.

The demultiplexer finally couples to a set of on/off single photon detectors. We wish to calculate the probability of observing C clicks, given an initial photon number state of N photons and given that all D detectors have a quantum efficiency η and a dark count probability ε. We start from the ideal case $\eta = 1,\ \varepsilon = 0$ and then move on to the general case $0 \leq \eta \leq 1,\ 0 \leq \varepsilon \leq 1$ and from the general case we retrieve a simple corollary that holds for $0 \leq \eta \leq 1,\ \varepsilon \ll N/D$.

A.3.1 Ideal detectors

The fundamental ingredient for our analysis is the probability of distributing N photons into exactly C out of D detectors. We start by numbering the detectors from 1 to D, then a certain string of numbers will describe an event, where the detectors numbered in the string are the ones that clicked. Note that in absence of noise the number of clicks cannot exceed the number of input photons, i.e. $C \leq N$.

Lemma (Ideal detection). *The probability of observing C clicks by distributing a Fock state of N photons evenly amongst D ideal (i.e. noiseless and with 100% quantum efficiency) on/off detectors is given by*

$$P_D(C|N) = \binom{D}{C} \frac{C!}{D^N} \mathcal{S}_N^C, \tag{A.2}$$

where $\mathcal{S}$ is the Stirling number of second kind.

Proof. Our goal is to compute the fraction of detection strings (i.e. the strings of numbers describing a detection event, as described above) that include exactly C out of D detectors, modulo reorderings. Call S_i the set of strings corresponding to N input photons that do not include the i-th detector. Then select a specific subset $\mathcal{K}$ of cardinality $|\mathcal{K}| = k$ from the D detectors. The set of strings that do not include any of the detectors in $\mathcal{K}$ is the intersection of the sets excluding each of the elements of $\mathcal{K}$: $\bigcap_{i \in \mathcal{K}} S_i$ and its cardinality is

$$\left| \bigcap_{i \in \mathcal{K}} S_i \right| = (D - k)^N \tag{A.3}$$

as we have N choices with repetition, from $(D-k)$ possible detectors. Of course, we are also counting strings that exclude *any other* detector, in addition to the ones in $\mathcal{K}$. To get around this problem, we use the inclusion-exclusion rule to count the elements in unions of sets S_i. In particular, we need the union of S_i for $i \in \{1, \ldots, D\}$, i.e. the set of all strings that exclude *at least* 1 detector, whose cardinality is

$$\left|\bigcup_{i=1}^{D} S_i\right| = \sum_{j=1}^{D} (-1)^{j+1} \binom{D}{j} (D-j)^N \tag{A.4}$$

The complement of this set is the set of strings that include all D detectors (if they missed any they would belong to $\bigcup_{i=1}^{D} S_i$), whose cardinality is

$$\left|\overline{\bigcup_{i=1}^{D} S_i}\right| = D^N - \left|\bigcup_{i=1}^{D} \overline{S_i}\right| = \sum_{j=0}^{D} (-1)^{j} \binom{D}{j} (D-j)^N \tag{A.5}$$

Finally, we can compute the number of strings that include precisely C out of D detectors: pick $D-C$ detectors to be excluded (there are $\binom{D}{C}$ ways of doing this) and compute the number of strings that include all of the remaining C detectors:

$$\begin{aligned}\binom{D}{C}\left|\overline{\bigcup_{i=1}^{C} S_i}\right| &= \binom{D}{C} \sum_{j=0}^{C} (-1)^{j} \binom{C}{j} (C-j)^N &\text{(A.6)}\\ &= \binom{D}{C} C!\, \mathcal{S}_N^C, &\text{(A.7)}\end{aligned}$$

where $\mathcal{S}_N^C$ is the Stirling number of the second kind. So the probability of ending up with exactly C clicks is the result above divided by the total number of possible strings D^N:

$$P_D(C|N) = \binom{D}{C} \frac{C!}{D^N} \mathcal{S}_N^C \tag{A.8}$$

and our proof is complete (see Eq. (14) in [186] for an implicit POVM representation). □

A.3.2 Nonideal detectors

Nonideal detectors are subject to mainly two effects: sub-unity quantum efficiency and noise, which can come from various sources. We model these as Bernoulli trials, where for each detector we have a probability η of missing the photon and a probability ε of a false count within the measurement window, in which case we are informed that the detector clicked regardless of a photon hitting it or not. Whether a detector detects an actual photon or gives a false count, we consider it unable to give further clicks until the electronics have enough time to reset (e.g. about 40 ns for avalanche photodiodes). In this section we take both of these effects into account.

Theorem (Noisy detection). *The probability of observing C clicks by distributing a Fock state of N photons evenly amongst D on/off detectors with quantum efficiency η and false count probability ε is given by*

$$P_{D,\eta,\varepsilon}(C|N) = \sum_{i=0}^{C} p_{\varepsilon}(i|D) \sum_{j=C-i}^{N} p_{\frac{D-i}{D}}(j|N) \sum_{k=C-i}^{j} p_{\eta}(k|j) P_{D-i}(C-i|k), \tag{A.9}$$

where $p_{\xi}(m|n) = \binom{n}{m}\xi^{m}(1-\xi)^{n-m}$ is the probability of having m successes out of n trials when the success probability of a single trial is ξ.

Proof. The proof comprises of 3 steps, each of which is of a similar nature: we consider all the ways in which an event can happen and we sum the relative probabilities. In the first step we split the observed number of clicks into spurious and real clicks. In the second step we split the initial photons into those that landed onto inactive detectors (the noisy ones) and those that landed onto active ones.

In the third step we split the photons that landed onto active detectors into those that were lost because of quantum efficiency and those that weren't. Finally, we use the ideal detection Lemma.

Step 1: We sum over the probability of obtaining C total clicks by having i of them come from noise and $C - i$ come from actual detections. We write the probability of i false events given D detectors as $p_\varepsilon(i|D) = \binom{D}{i}\varepsilon^i(1-\varepsilon)^{D-i}$.

Step 2: Now $C - i$ clicks must come from real detection events from the remaining $D - i$ active detectors. The probability that j out of N photons make it to the $D - i$ active detectors is $p_{\frac{D-i}{D}}(j|N)$.

Step 3: As our detectors have a quantum efficiency $\eta \leq 1$, the probability of remaining with k out of j photons is given by $p_\eta(k|j)$.

Now we can now apply the Lemma to write the probability of detecting $C - i$ out of k survivor photons with $D - i$ detectors and combine these steps in the final result. $\square$

There is a simple corollary of this theorem, which describes the case $\varepsilon = 0$. Such corollary can be used even for noisy detectors as long as the number of false positives is low enough ($D\varepsilon \ll N$):

Corollary (Noiseless detection). *The probability of observing C clicks by distributing a Fock state of N photons evenly amongst D noiseless on/off detectors with quantum efficiency η is given by*

$$P_{D,\eta}(C|N) = \sum_{k=C}^{N} p_\eta(k|N) P_D(C|k). \tag{A.10}$$

Proof. We use the identity $p_0(m|n) = \delta_{m,0}$ to replace every occurrence of i in the noisy detection Theorem by 0, and the identity $p_1(m|n) = \delta_{m,n}$ to replace every occurrence of j by N. This gets rid of the first two summations and the result follows. $\square$

Note that modeling the imperfect detectors by placing a beam splitter with transmissivity η in front of ideal detectors [189, 28] would be wrong in this context because quantum efficiency does not apply to false counts: first we exclude false counts and photons that landed on inactive detectors, only then we can factor in the quantum efficiency. Note that this result is different than what one would obtain when modeling the imperfect detector by placing a beamsplitter with transmissivity η in front of an ideal detector.

A.4 Retrodicting the photon number

To retrodict the photon number *given* an observed number of clicks, we have to invert the probability in the main theorem using Bayes' rule:

$$P_{D,\eta,\varepsilon}(N|C) = \frac{P_{D,\eta,\varepsilon}(C|N)Pr(N)}{\sum_k P_{D,\eta,\varepsilon}(C|k)Pr(k)} \tag{A.11}$$

This general formula is always valid, but it cannot be solved explicitly unless we specify the prior, which is what we will do next, for some special cases of particular relevance.

A.4.1 Poisson prior

In case of a Poissonian prior with mean photon number μ (which may occur when we deal with coherent states for instance) we have:

$$Pr(N) = \frac{\mu^N e^{-\mu}}{N!}, \tag{A.12}$$

and we can find an explicit expression for the ideal retrodiction probability:

$$P_D^{\text{Poisson}}(N|C) = \frac{C!\,\mathcal{S}_N^C}{N!\,\gamma^N}\frac{1}{(e^{1/\gamma}-1)^C} \tag{A.13}$$

where $\gamma = D/\mu$.

A.4.2 Thermal prior

In case of a thermal prior with mean photon number μ (which occurs for instance for two-mode squeezed vacuum states) we have:

$$Pr(N) = \frac{\mu^N}{(\mu+1)^{N+1}}, \tag{A.14}$$

and the ideal retrodiction probability can be written as:

$$P_D^{\text{Therm}}(N|C) = \frac{C!\,\mathcal{S}_N^C}{(D+\gamma)^N}\frac{\Gamma(D+\gamma)}{\Gamma(D+\gamma-C)!} \tag{A.15}$$

A.4.3 Considerations

When one moves away from the ideal case, quantum efficiency typically matters more than the number of detectors. The probability of detecting all the input photons with a noiseless apparatus saturates at a value lower than 1 even for an infinite number of detectors:

$$\lim_{D\to\infty} P_{D,\eta}(N|N) = \eta^N \tag{A.16}$$

The effect of noise in the detectors is tangible only when their number is sufficiently large, for instance, when the number of spurious counts is comparable with the actual number of photons hitting the detectors, i.e., when $D\varepsilon \approx N$. This fact makes the noiseless detection corollary a good tool even in the case of realistic detectors if we have a large enough number of them.

A.5 Applications

We now would like to give a few examples of how to apply our results. The examples will be about retrodicting the photon number in order to herald some desired quantum states and are based on our analytical results (not on Monte Carlo simulations).

A.5.1 Example 1: heralding of a NOON state

For this example we consider the following setup: we replace the two mirrors in the middle of a Mach-Zehnder (MZ) interferometer with 50:50 beam splitters and add detectors to measure the photons that leak. This configuration (if the phase difference between the two arms of the MZ is set to $\pi/2$) will output a $(|4,0\rangle + |0,4\rangle)/\sqrt{2}$ state if we start with the state $|3,3\rangle$ and if each of the two detectors measures exactly 1 photon.

Now the question is how well do we know that we had exactly 1 photon at the detectors? If we resort to demultiplexed detection, we first need to compute the prior joint probability $Pr(N_1, N_2)$ of having N_1 photons at detector 1 and N_2 photons at detector 2. This is achieved using simple input-output relations for 50:50 beam splitters; we report it in Table A.1.

Then, we apply Bayes' rule (assuming that the two sets of demultiplexed detectors are identical, but we could easily modify the equation below to account for

	0	1	2	3	4	5	6
0	$\frac{1}{64}$	$\frac{3}{64}$	$\frac{3}{32}$	$\frac{7}{64}$	$\frac{39}{512}$	$\frac{15}{512}$	$\frac{5}{1024}$
1	$\frac{3}{64}$	$\frac{3}{64}$	$\frac{3}{64}$	$\frac{3}{128}$	$\frac{3}{512}$	0	0
2	$\frac{3}{32}$	$\frac{3}{64}$	$\frac{9}{256}$	$\frac{3}{256}$	$\frac{3}{1024}$	0	0
3	$\frac{7}{64}$	$\frac{3}{128}$	$\frac{3}{256}$	0	0	0	0
4	$\frac{39}{512}$	$\frac{3}{512}$	$\frac{3}{1024}$	0	0	0	0
5	$\frac{15}{512}$	0	0	0	0	0	0
6	$\frac{5}{1024}$	0	0	0	0	0	0

TABLE A.1: Joint probabilities of having (i, j) photons (where i and j are listed in the headings on top and on the left) at the detectors in the modified MZ interferometer of the NOON state heralding example. These are computed assuming the input $|3, 3\rangle$.

different configurations) and find $P_{D,\eta,\varepsilon}(N_1, N_2|C_1, C_2)$ to be given by

$$\frac{P_{D,\eta,\varepsilon}(C_1|N_1)P_{D,\eta,\varepsilon}(C_2|N_2)Pr(N_1, N_2)}{\sum_{k_1,k_2} P_{D,\eta,\varepsilon}(C_1|k_1)P_{D,\eta,\varepsilon}(C_2|k_2)Pr(k_1, k_2)} \tag{A.17}$$

We finally use the quantity $P_{D,\eta,\varepsilon}(N_1, N_2|C_1, C_2)$ to infer the retrodictive power of our demultiplexed detectors. To complete the example, in Fig. A.1 we plot the retrodicted probabilities of four configurations: 4 and 64 detectors with 60% and 75% quantum efficiency (and 500 dark counts/sec, with 10 ns gated measurement window), given that they both reported a single click each.

For comparison, in Fig. A.2 we plot the retrodiction probabilities for a non-demultiplexed measurement.

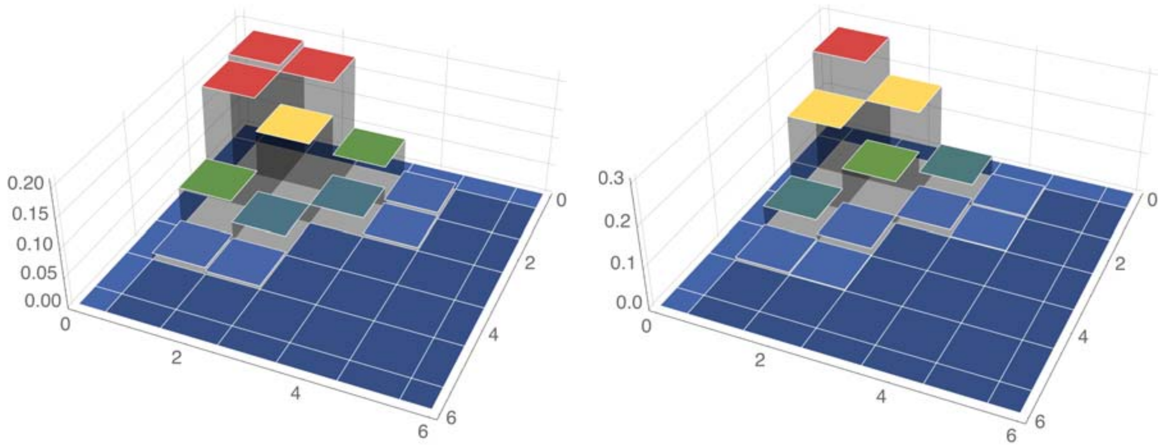

(A) 4 detectors per port, 60% QE

(B) 4 detectors per port, 75% QE

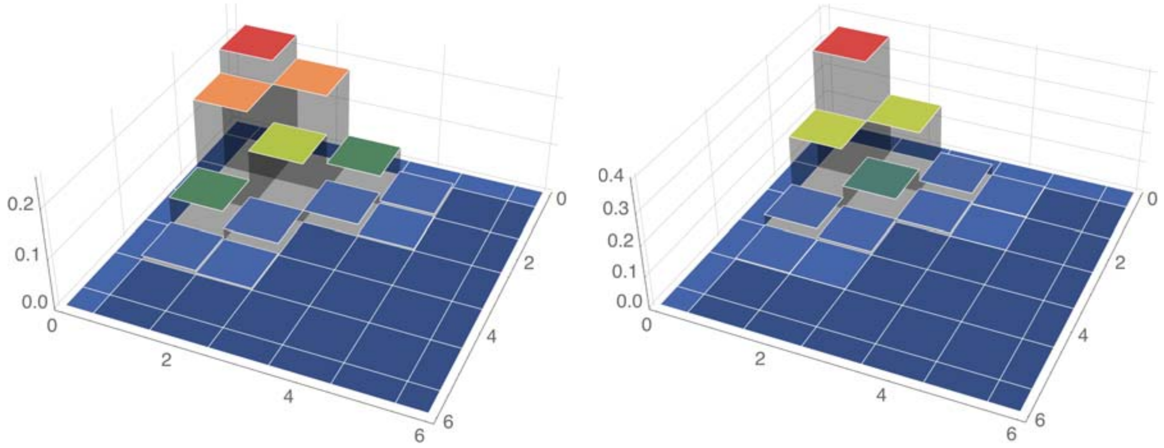

(C) 64 detectors per port, 60% QE

(D) 64 detectors per port, 75% QE

FIGURE A.1: Plots of the probability of retrodicted photon number for a NOON state heralding setup using demultiplexed detection. Although the most probable case is the desired $|1,1\rangle$, its individual probability can be quite low, which leads to a low fidelity with the desired NOON state. The bottleneck in this case is quantum efficiency: even increasing the number of detectors from 4 to 64 does not perform as well as increasing the quantum efficiency from 60% to 75%.

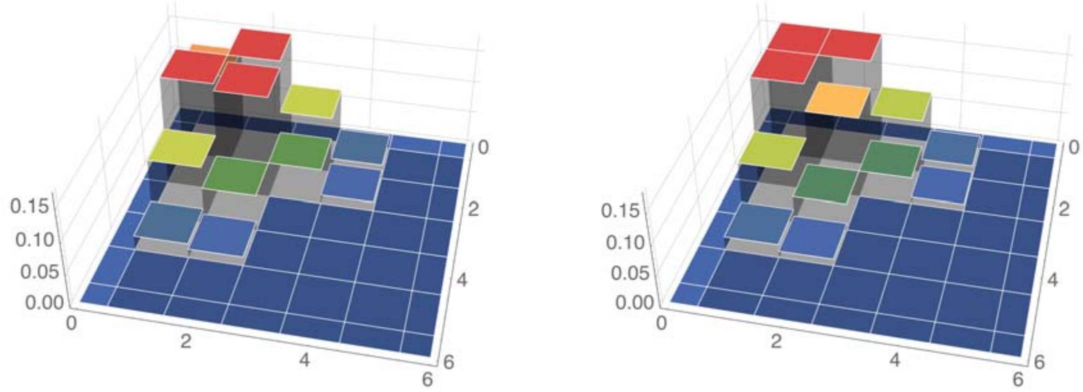

(A) 1 detector per port, 75% QE

(B) 1 detector per port, 100% QE

FIGURE A.2: (left) A pair of realistic detectors are likely to lie: if they report a single click each, the state was more likely to be $|1,2\rangle$ or $|2,1\rangle$ or even $|2,2\rangle$. (right) Even a pair of ideal (100% quantum efficiency) detectors assign equal probability to the states $|1,1\rangle$, $|1,2\rangle$ and $|2,1\rangle$.

A.5.2 Example 2: single photon heralding from squeezed vacuum

We now consider an example of single photon heralding from a two-mode squeezed vacuum, which is performed by producing photons in pairs and heralding one by detecting the other. Such two-mode state can be generated by pumping a nonlinear crystal with an intense coherent laser [190]. The output of the process is a state in the following form:

$$\hat{S}(\zeta)|0,0\rangle = \sum_{n=0}^{\infty} e^{in\phi} \frac{\sinh(g)^n}{\left(\sinh(g)^2+1\right)^{\frac{n+1}{2}}}|n,n\rangle, \tag{A.18}$$

where $\zeta = ge^{i\phi}$ is the squeezing parameter. For small enough values of the gain g one can indeed ignore components with photon number larger than 1, but if the gain is too large, the heralded state is likely to contain more than 1 photon. If such

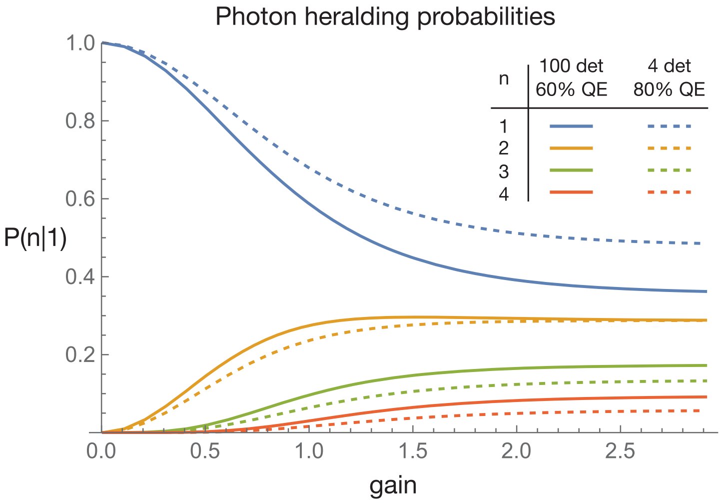

Figure A.3: Plots of the probability of retrodicted photon number for a squeezed vacuum state. Again, the bottleneck is quantum efficiency: four detectors with 80% QE are better at heralding a single photon than 100 detectors with 60% QE.

states were further used for crucial applications such as quantum cryptography, they would be vulnerable for example to the photon number splitting attack. Could a demultiplexed detection scheme make for a better heralded single-photon source? First note that the amplitudes of the two-mode squeezed vacuum follow a thermal distribution, if we recognize that $\sinh(g)^2$ is the mean photon number per mode. Then, we apply Eq. (A.11) (we could use Eq. (A.15) in case our quantum efficiency is high) to find the retrodicted photon number distribution, which we plot for a few examples in Fig. A.3. Note that as the gain increases, the probability of the various number states levels off and becomes constant, but recall that these probabilities are conditional on detecting a single photon, whose probability will decrease with gain.

A.6 conclusions and outlook

In conclusion, we have shown the most unbiased way of analyzing a detection event in a demultiplexed measurement scheme, taking noise and efficiency into account. The corollary of our theorem can apply even to realistic situations if some conditions on the noise are met, which can be very advantageous as it is computationally much simpler to implement than the full theorem.

Our results can be applied also to optical engineering issues, such as on-chip denoising in consumer imaging devices, where multiple pixels can fill an Airy disk and can be used to retrodict the intensity more accurately. There are still interesting questions to be asked, for instance, whether it is possible to find closed form solutions of Eq. (A.11) for useful priors when the quantum efficiency is not unity, or if there is a reasonable way of relaxing the assumption of uniform illumination. We leave these to a future work.

Bibliography

[1] L. V. Hau, S. E. Harris, Z. Dutton, and C. H. Behroozi. "Light speed reduction to 17 metres per second in an ultracold atomic gas". In: *Nature (London)* 397 (1999), p. 594. DOI: 10.1038/17561.

[2] M. M. Kash, V. A. Sautenkov, A. S. Zibrov, L. Hollberg, G. R. Welch, M. D. Lukin, Y. Rostovtsev, E. S. Fry, and M. O. Scully. "Ultraslow Group Velocity and Enhanced Nonlinear Optical Effects in a Coherently Driven Hot Atomic Gas". In: *Phys. Rev. Lett.* 82 (26 1999), pp. 5229–5232. DOI: 10.1103/PhysRevLett.82.5229.

[3] D. Budker, D. F. Kimball, S. M. Rochester, and V. V. Yashchuk. "Nonlinear Magneto-optics and Reduced Group Velocity of Light in Atomic Vapor with Slow Ground State Relaxation". In: *Phys. Rev. Lett.* 83 (9 1999), pp. 1767–1770. DOI: 10.1103/PhysRevLett.83.1767.

[4] P. W. Milonni. *Fast Light, Slow Light and Left-Handed Light.* CRC Press, 2004.

[5] L. J. Wang, A. Kuzmich, and A. Dogariu. "Gain-assisted superluminal light propagation". In: *Nature* 406 (2000), p. 277. DOI: 10.1038/35018520.

[6] E. E. Mikhailov, V. A. Sautenkov, I. Novikova, and G. R. Welch. "Large negative and positive delay of optical pulses in coherently prepared dense Rb vapor with buffer gas". In: *Phys. Rev. A* 69 (6 2004), p. 063808. DOI: 10.1103/PhysRevA.69.063808.

[7] U. Leonhardt. "A laboratory analogue of the event horizon using slow light in an atomic medium". In: *Nature* 415 (2002), p. 406. DOI: `10.1038/415406a`.

[8] U. Leonhardt and P. Piwnicki. "Relativistic Effects of Light in Moving Media with Extremely Low Group Velocity". In: *Phys. Rev. Lett.* 84 (5 2000), pp. 822–825. DOI: `10.1103/PhysRevLett.84.822`.

[9] J. M. Dudley, F. Dias, M. Erkintalo, and G. Genty. "Instabilities, breathers and rogue waves in optics". In: *Nature Photonics* 8 (2014), 755–764. DOI: `10.1038/nphoton.2014.220`.

[10] H. Raether. *Surface plasmons on smooth and rough surfaces and on gratings.* Springer, 1988.

[11] N. Ashcroft and N. Mermin. *Solid State Physics*. Brooks Cole, 1976.

[12] H. J. Metcalf and P. van der Straten. *Laser Cooling and Trapping*. Springer, 1999.

[13] M. Fleischhauer and M. D. Lukin. "Dark-State Polaritons in Electromagnetically Induced Transparency". In: *Phys. Rev. Lett.* 84 (22 2000), pp. 5094–5097. DOI: `10.1103/PhysRevLett.84.5094`.

[14] O. Kocharovskaya, Y. Rostovtsev, and M. O. Scully. "Stopping Light via Hot Atoms". In: *Phys. Rev. Lett.* 86 (4 2001), pp. 628–631. DOI: `10.1103/PhysRevLett.86.628`.

[15] B. Julsgaard, J. Sherson, J. I. Cirac, J. Fiurášek, and E. S. Polzik. "Experimental demonstration of quantum memory for light". In: *Nature* 432 (2004), p. 482. DOI: `10.1038/nature03064`.

[16] M. Fleischhauer, A. Imamoglu, and J. P. Marangos. "Electromagnetically induced transparency: Optics in coherent media". In: *Rev. Mod. Phys.* 77 (2 2005), pp. 633–673. DOI: `10.1103/RevModPhys.77.633`.

[17] R. W. Boyd and S. G. Lukishova. *Self-focusing: Past and Present*. Springer, 2009.

[18] R. Miles and S. Harris. “Optical third-harmonic generation in alkali metal vapors”. In: *IEEE Journal of Quantum Electronics* 9.4 (1973), pp. 470–484. ISSN: 0018-9197. DOI: 10.1109/JQE.1973.1077492.

[19] C. J. Foot. *Atomic Physics*. Oxford University Press, 2005.

[20] H. G. Kuhn. *Atomic Spectra*. Longmans, 1962.

[21] M. A. Zentile, J. Keaveney, L. Weller, D. J. Whiting, C. S. Adams, and I. G. Hughes. “ElecSus: A program to calculate the electric susceptibility of an atomic ensemble”. In: *Computer Physics Communications* 189 (2015), pp. 162 –174. ISSN: 0010-4655. DOI: https://doi.org/10.1016/j.cpc.2014.11.023.

[22] D. A. Steck. *Quantum and Atom Optics, available online at http://steck.us/teaching*. 2015.

[23] D. A. Steck. *Rubidium 85 D Line Data, available online at http://steck.us/alkalidata*. 2013.

[24] D. A. Steck. *Rubidium 87 D Line Data, available online at http://steck.us/alkalidata*. 2013.

[25] E. Arimondo, M. Inguscio, and P. Violino. “Experimental determinations of the hyperfine structure in the alkali atoms”. In: *Rev. Mod. Phys.* 49 (1 1977), pp. 31–75. DOI: 10.1103/RevModPhys.49.31.

[26] R. W. Boyd. *Nonlinear Optics*. Academic Press, 2008.

[27] J. J. Sakurai and J. J. Napolitano. *Modern Quantum Mechanics (2nd Edition)*. Pearson, 2010.

[28] R. Loudon. *The Quantum Theory of Light (3rd edition)*. Oxford University Press, 2000.

[29] J. H. Eberly P. W. Milonni. *Laser Physics*. Wiley, 2010.

[30] U. Volz and H. Schmoranzer. "Precision lifetime measurements on alkali atoms and on helium by beam–gas–laser spectroscopy". In: *Physica Scripta* 1996.T65 (1996), p. 48. URL: `http://stacks.iop.org/1402-4896/1996/i=T65/a=007`.

[31] A. Gallagher and E. L. Lewis. "Determination of the vapor pressure of rubidium by optical absorption". In: *J. Opt. Soc. Am.* 63.7 (1973), pp. 864–869. DOI: `10.1364/JOSA.63.000864`.

[32] P. Siddons, C. S. Adams, C. Ge, and I. G. Hughes. "Absolute absorption on rubidium D lines: comparison between theory and experiment". In: *Journal of Physics B: Atomic, Molecular and Optical Physics* 41.15 (2008), p. 155004. URL: `http://stacks.iop.org/0953-4075/41/i=15/a=155004`.

[33] D. A. Smith and I. G. Hughes. "The role of hyperfine pumping in multilevel systems exhibiting saturated absorption". In: *American Journal of Physics* 72.5 (2004), pp. 631–637. DOI: `10.1119/1.1652039`.

[34] M. Himsworth and T. Freegarde. "Rubidium pump-probe spectroscopy: Comparison between ab initio theory and experiment". In: *Phys. Rev. A* 81 (2 2010), p. 023423. DOI: `10.1103/PhysRevA.81.023423`.

[35] B. Gao. "Effects of Zeeman degeneracy on the steady-state properties of an atom interacting with a near-resonant laser field: Resonance flourescence". In: *Phys. Rev. A* 50 (5 1994), pp. 4139–4156. DOI: `10.1103/PhysRevA.50.4139`.

[36] A. Safari, I. De Leon, M. Mirhosseini, O. S. Magaña Loaiza, and R. W. Boyd. "Light-Drag Enhancement by a Highly Dispersive Rubidium Vapor". In: *Phys. Rev. Lett.* 116 (1 2016), p. 013601. DOI: `10.1103/PhysRevLett.116.013601`.

[37] A. J. Fresnel. In: *Ann. Chim. Phys.* 9(XLIX) (1818), pp. 57–66.

[38] A. H. L. Fizeau. In: *Comptes Rendus* 33 (1851), pp. 349–355.

[39] H. A. Lorentz. In: *Proc. R. Acad. Sci. Amsterdam* 6 (1904), p. 809.

[40] P. Zeeman. In: *KNAW, Proceedings, Amsterdam* 17 I (1914), pp. 445–451.

[41] P. Zeeman. In: *KNAW, Proceedings, Amsterdam* 18 I (1915), pp. 398–408.

[42] P. Zeeman. In: *Proc. R. Acad. Sci., Amsterdam* 18 (1916), pp. 398–408.

[43] P. Zeeman. In: *KNAW, Proceedings, Amsterdam* 22 I (1919), pp. 462–470.

[44] A. Snethlage and P. Zeeman. In: *KNAW, Proceedings, Amsterdam* 22 II (1920), pp. 512–522.

[45] A. Snethlage P. Zeeman W. de Groot and G. C. Diebetz. In: *KNAW, Proceedings, Amsterdam* 23 (1920), pp. 1402–1411.

[46] P. Zeeman. In: *Arch. Neerl. Sci. Exactes Nat. 3A* 10 (1927), p. 131.

[47] I. Lerche. "The Fizeau effect: Theory, experiment, and Zeeman's measurements". In: *American Journal of Physics* 45.12 (1977), pp. 1154–1163. DOI: `10.1119/1.10759`.

[48] H. R. Bilger and A. T. Zavodny. "Fresnel Drag in a Ring Laser: Measurement of the Dispersive Term". In: *Phys. Rev. A* 5 (2 1972), pp. 591–599. DOI: `10.1103/PhysRevA.5.591`.

[49] G. A. Sanders and S. Ezekiel. "Measurement of Fresnel drag in moving media using a ring-resonator technique". In: *J. Opt. Soc. Am. B* 5.3 (1988), pp. 674–678. DOI: `10.1364/JOSAB.5.000674`.

[50] E. J. Post. "Sagnac Effect". In: *Rev. Mod. Phys.* 39 (2 1967), pp. 475–493. DOI: `10.1103/RevModPhys.39.475`.

[51] G. E. Stedman. "Ring-laser tests of fundamental physics and geophysics". In: *Reports on Progress in Physics* 60.6 (1997), p. 615. URL: `http://stacks.iop.org/0034-4885/60/i=6/a=001`.

[52] A. G. Klein, G. I. Opat, A. Cimmino, A. Zeilinger, W. Treimer, and R. Gähler. "Neutron Propagation in Moving Matter: The Fizeau Experiment with Massive Particles". In: *Phys. Rev. Lett.* 46 (24 1981), pp. 1551–1554. DOI: `10.1103/PhysRevLett.46.1551`.

[53] R. W. Boyd and D. J. Gauthier. "Controlling the Velocity of Light Pulses". In: *Science* 326.5956 (2009), pp. 1074–1077. DOI: `10.1126/science.1170885`.

[54] D. Strekalov, A. B. Matsko, N. Yu, and L. Maleki. "Observation of Light Dragging in a Rubidium Vapor Cell". In: *Phys. Rev. Lett.* 93 (2 2004), p. 023601. DOI: `10.1103/PhysRevLett.93.023601`.

[55] S. Davuluri and Y. V. Rostovtsev. "Controllable enhanced dragging of light in ultradispersive media". In: *Phys. Rev. A* 86 (1 2012), p. 013806. DOI: `10.1103/PhysRevA.86.013806`.

[56] I. Carusotto, M. Artoni, G. C. La Rocca, and F. Bassani. "Transverse Fresnel-Fizeau drag effects in strongly dispersive media". In: *Phys. Rev. A* 68 (6 2003), p. 063819. DOI: `10.1103/PhysRevA.68.063819`.

[57] S. Franke-Arnold, G. Gibson, R. W. Boyd, and M. J. Padgett. "Rotary Photon Drag Enhanced by a Slow-Light Medium". In: *Science* 333.6038 (2011), pp. 65–67. DOI: `10.1126/science.1203984`.

[58] R. Resnick. *Introduction to Special Relativity.* Wiley, New York, 1968.

[59] J. Laub. "Zur Optik der bewegten Körper". In: *Annalen der Physik* 330.1 (1908), pp. 175–184. DOI: `10.1002/andp.19083300113`.

[60] R. M. Camacho, M. V. Pack, J. C. Howell, A. Schweinsberg, and R. W. Boyd. "Wide-Bandwidth, Tunable, Multiple-Pulse-Width Optical Delays Using Slow Light in Cesium Vapor". In: *Phys. Rev. Lett.* 98 (15 2007), p. 153601. DOI: `10.1103/PhysRevLett.98.153601`.

[61] B. E. Sherlock and I. G. Hughes. "How weak is a weak probe in laser spectroscopy?" In: *American Journal of Physics* 77.2 (2009), pp. 111–115. DOI: `10.1119/1.3013197`.

[62] A. Safari, R. Fickler, M. J. Padgett, and R. W. Boyd. "Generation of Caustics and Rogue Waves from Nonlinear Instability". In: *Phys. Rev. Lett.* 119 (20 2017), p. 203901. DOI: `10.1103/PhysRevLett.119.203901`.

[63] M. V. Berry and C. Upstill. "IV Catastrophe Optics: Morphologies of Caustics and Their Diffraction Patterns". In: *Progress in Optics* 18 (1980), pp. 257 –346. ISSN: 0079-6638. DOI: `http://dx.doi.org/10.1016/S0079-6638(08)70215-4`.

[64] M. A. Topinka, B. J. LeRoy, R. M. Westervelt, S. E. J. Shaw, R. Fleischmann, E. J. Heller, K. D. Maranowski, and A. C. Gossard. "Coherent branched flow in a two-dimensional electron gas". In: *Nature* 410 (6825 2001), p. 183. URL: `http://dx.doi.org/10.1038/35065553`.

[65] R. Höhmann, U. Kuhl, H.-J. Stöckmann, L. Kaplan, and E. J. Heller. “Freak Waves in the Linear Regime: A Microwave Study”. In: *Phys. Rev. Lett.* 104 (9 2010), p. 093901. DOI: `10.1103/PhysRevLett.104.093901`.

[66] M. V. Berry. “Focused tsunami waves”. In: *Proceedings of the Royal Society of London A: Mathematical, Physical and Engineering Sciences* 463.2087 (2007), pp. 3055–3071. DOI: `10.1098/rspa.2007.0051`.

[67] H. Degueldre, J. J. Metzger, T. Geisel, and R. Fleischmann. “Random focusing of tsunami waves”. In: *Nat Phys* 12 (3 2016), p. 259. URL: `http://dx.doi.org/10.1038/nphys3557`.

[68] C. Kharif and E. Pelinovsky. “Physical mechanisms of the rogue wave phenomenon”. In: *European Journal of Mechanics - B/Fluids* 22.6 (2003), pp. 603 –634. DOI: `http://dx.doi.org/10.1016/j.euromechflu.2003.09.002`.

[69] D. R. Solli, C. Ropers, P. Koonath, and B. Jalali. “Optical rogue waves”. In: *Nature* 450 (2007), pp. 1054–1057. DOI: `10.1038/nature06402`.

[70] C. Liu, R. E. C. van der Wel, N. Rotenberg, L. Kuipers, T. F. Krauss, A. Di Falco, and A. Fratalocchi. “Triggering extreme events at the nanoscale in photonic seas”. In: *Nature Physics* 11 (2015), 358–363. DOI: `10.1038/nphys3263`.

[71] S. Birkholz, E. T. J. Nibbering, C. Brée, S. Skupin, A. Demircan, G. Genty, and G. Steinmeyer. “Spatiotemporal Rogue Events in Optical Multiple Filamentation”. In: *Phys. Rev. Lett.* 111 (24 2013), p. 243903. DOI: `10.1103/PhysRevLett.111.243903`.

[72] M. G. Brown. “Space–time surface gravity wave caustics: structurally stable extreme wave events”. In: *Wave Motion* 33.2 (2001), pp. 117 –143. DOI: `http://dx.doi.org/10.1016/S0165-2125(00)00054-8`.

[73] C. Fochesato, S. Grilli, and F. Dias. "Numerical modeling of extreme rogue waves generated by directional energy focusing". In: *Wave Motion* 44.5 (2007), pp. 395 –416. DOI: `http://dx.doi.org/10.1016/j.wavemoti.2007.01.003`.

[74] E. J. Heller, L. Kaplan, and A. Dahlen. "Refraction of a Gaussian seaway". In: *J. Geophys. Res.* 113 (2008), p. C09023. DOI: `10.1029/2008JC004748`.

[75] D. H. Peregrine. "Wave jumps and caustics in the propagation of finite-amplitude water waves". In: *J. Fluid Mech* 136 (1983), p. 435. DOI: `10.1017/S0022112083002220`.

[76] A. Mathis, L. Froehly, S. Toenger, F. Dias, G. Genty, and J. M. Dudley. "Caustics and Rogue Waves in an Optical Sea". In: *Scientific Reports* 5 (2015), p. 12822. DOI: `10.1038/srep12822`.

[77] D. Pierangeli, F. Di Mei, C. Conti, A. J. Agranat, and E. DelRe. "Spatial Rogue Waves in Photorefractive Ferroelectrics". In: *Phys. Rev. Lett.* 115 (9 2015), p. 093901. DOI: `10.1103/PhysRevLett.115.093901`.

[78] M. Mattheakis, I. J. Pitsios, G. P. Tsironis, and S. Tzortzakis. "Extreme events in complex linear and nonlinear photonic media". In: *Chaos, Solitons and Fractals* 84 (2016), pp. 73 –80. ISSN: 0960-0779. DOI: `http://doi.org/10.1016/j.chaos.2016.01.008`.

[79] F. Fedele, J. Brennan, S. Ponce De León, J. Dudley, and F. Dias. "Real world ocean rogue waves explained without the modulational instability". In: *Scientific Reports* 6 (2016), p. 27715. DOI: `10.1038/srep27715`.

[80] S. Birkholz, C. Brée, I. Veselić, A. Demircan, and G. Steinmeyer. "Ocean rogue waves and their phase space dynamics in the limit of a linear interference model". In: *Scientific Reports* 6 (2016), p. 35207. DOI: `10.1038/srep35207`.

[81] D. H. Peregrine and R. Smith. "Nonlinear Effects upon Waves near Caustics". In: *Philosophical Transactions of the Royal Society of London. Series A, Mathematical and Physical Sciences* 292.1392 (1979), pp. 341–370. URL: `http://www.jstor.org/stable/75169`.

[82] S. Barkhofen, J. J. Metzger, R. Fleischmann, U. Kuhl, and H.-J. Stöckmann. "Experimental Observation of a Fundamental Length Scale of Waves in Random Media". In: *Phys. Rev. Lett.* 111 (18 2013), p. 183902. DOI: `10.1103/PhysRevLett.111.183902`.

[83] Y. A. Kravtsov and Y. I. Orlov. *Caustics, Catastrophes and Wave Fields.* Springer, 1993.

[84] R. P. Mercier. "Diffraction by a screen causing large random phase fluctuations". In: *Proc. Camb. Phil. Soc.* 58.5–6 (1962), pp. 382 –400. DOI: `10.1017/S0305004100036586`.

[85] J. F. Nye. *Natural focusing and fine structure of light: caustics and wave dislocations.* Bristol; Philadelphia: Institute of Physics Pub., 1999.

[86] D. A. Steck. *Quantum and Atom Optics.* http://steck.us/teaching, 2007.

[87] C. F. McCormick, D. R. Solli, R. Y. Chiao, and J. M. Hickmann. "Saturable nonlinear refraction in hot atomic vapor". In: *Phys. Rev. A* 69 (2 2004), p. 023804. DOI: `10.1103/PhysRevA.69.023804`.

[88] G. Agrawal. *Nonlinear Fiber Optics (Fifth Edition).* Academic Press, 2013. ISBN: 978-0-12-397023-7.

[89] G. B. Whitham. *Linear and Nonlinear Waves.* John Wiley and Sons, 1999.

[90] L. Pitaevskii and S. Stringari. *Bose-Einstein Condensation.* Oxford Science Publications, 2003.

[91] Y. V. Bludov, V. V. Konotop, and N. Akhmediev. “Matter rogue waves”. In: *Phys. Rev. A* 80 (3 2009), p. 033610. DOI: `10.1103/PhysRevA.80.033610`.

[92] O. S. Magaña Loaiza, I. De Leon, M. Mirhosseini, R. Fickler, A. Safari, U. Mick, B. McIntyre, P. Banzer, B. Rodenburg, G. Leuchs, and R. W. Boyd. “Exotic looped trajectories of photons in three-slit interference”. In: *Nature Communications* 7 (2016), p. 13987. DOI: `10.1038/ncomms13987`.

[93] L. Mandel. “Quantum effects in one-photon and two-photon interference”. In: *Rev. Mod. Phys.* 71.2 (1999), pp. 6861–6897. DOI: `10.1103/RevModPhys.71.S274`.

[94] D. M. Greenberger, M. A. Horne, and A. Zeilinger. “Multiparticle Interferometry and the Superposition Principle”. In: *Phys. Today* 46.8 (1993), pp. 22–34. DOI: `10.1063/1.881360`.

[95] P. Shadbolt, J. C. F. Mathews, A. Laing, and J. L. O’Brien. “Testing foundations of quantum mechanics with photons”. In: *Nat. Phys.* 10.4 (2014), pp. 278–286. DOI: `10.1038/nphys2931`.

[96] M. O. Scully, B. G. Englert, and H. Walther. “Quantum optical tests of complementarity”. In: *Nature* 351.6322 (1991), pp. 111–116. DOI: `10.1038/351111a0`.

[97] Y. H. Kim, R. Yu, S. P. Kulik, Y. Shih, and M. O. Scully. “Delayed "Choice" Quantum Eraser”. In: *Phys. Rev. Lett.* 84.1 (1999), pp. 0031–9007. DOI: `10.1103/PhysRevLett.84.1`.

[98] H. F. Schouten, N. Kuzmin, G. Dubois, T. D. Visser, G. Gbur, P. F. A. Alkemade, H. Blok, G. W. t. Hooft, D. Lenstra, and E. R. Eliel. “Plasmon-Assisted Two-Slit Transmission: Young’s Experiment Revisited”. In: *Phys. Rev. Lett.* 94.5 (2005), p. 053901. DOI: `10.1103/PhysRevLett.94.053901`.

[99] S. Kocsis, B. Braverman, S. Ravets, M. J. Stevens, R. P. Mirin, L. K. Shalm, and A. M. Steinberg. “Observing the Average Trajectories of Single Photons in a Two-Slit Interferometer”. In: *Science* 332.6034 (2011), pp. 1170–1173. DOI: `10.1126/science.1202218`.

[100] R. Menzel, D. Puhlmann, A. Heuer, and W. P. Schleich. “Wave-particle dualism and complementarity unraveled by a different mode”. In: *PNAS* 109.24 (2012), pp. 9314–9319. DOI: `10.1073/pnas.1201271109`.

[101] E. Bolduc, J. Leach, F. M. Miatto, G. Leuchs, and R. W. Boyd. “Fair sampling perspective on an apparent violation of duality”. In: *PNAS* 111.34 (2014), pp. 9314–9319. DOI: `10.1073/pnas.1400106111`.

[102] D. H. Mahler, L. Rosema, K. Fisher, L. Vermeyden, K. J. Kevin, H. M. Wiseman, and A. Steinberg. “Experimental nonlocal and surreal Bohmian trajectories”. In: *Science Advances* 2.12 (2016), e11501466. DOI: `10.1126/sciadv.1501466`.

[103] R. D. Sorkin. “Quantum Mechanics as Quantum Measure Theory”. In: *Mod. Phys. Lett. A* 09.33 (1994), pp. 3119–3127. DOI: `10.1142/S021773239400294X`.

[104] U. Sinha, C. Couteau, T. Jennewein, R. Laflamme, and G. Weihs. “Ruling Out Multi-Order Interference in Quantum Mechanics”. In: *Science* 329.5990 (2010), pp. 418–421. DOI: `10.1126/science.1190545`.

[105] H. De Raedt and K. Hess. "Analysis of multipath interference in three-slit experiments". In: *Phys. Rev. A* 85.1 (2012), p. 012101. DOI: `10.1103/PhysRevA.85.012101`.

[106] R. Sawant, J. Samuel, A. Sinha, A. Sinha, and U. Sinha. "Nonclassical Paths in Quantum Interference Experiments". In: *Phys. Rev. Lett.* 113.12 (2014), p. 120406. DOI: `10.1103/PhysRevLett.113.120406`.

[107] A. Sinha, A. Vijay, and U. Sinha. "On the superposition principle in interference experiments". In: *Scientific Reports* 5 (2015), p. 10304. DOI: `10.1038/srep10304`.

[108] J. W. Goodman. *Introduction to Fourier Optics*. McGraw-Hill, New York, 1968.

[109] R. P. Feynman and A. R. Hibbs. *Quantum Mechanics and Path Integrals*. 3rd Ed. McGraw-Hill, New York, 1965.

[110] M. W. Kowarz. "Homogeneous and evanescent contributions in scalar near-field diffraction". In: *Appl. Opt.* 34.17 (1995), pp. 3055–3063. ISSN: 0003-6935. DOI: `10.1364/AO.34.003055`.

[111] W. L. Barnes, A. Dereux, and T. W. Ebbesen. "Surface plasmon subwavelength optics". In: *Nature* 424 (2003), pp. 824–830. DOI: `10.1038/nature01937`.

[112] G. Gay, O. Alloschery, B. Viaris de Lesegno, C. O'Dwyer, J. Weiner, and H. J. Lezec. "The optical response of nanostructured surfaces and the composite diffracted evanescent wave model". In: *Nat. Phys.* 2.4 (2006), pp. 262–267. DOI: `10.1038/nphys264`.

[113] R. Fickler, M. Krenn, R. Lapkiewicz, S. Ramelow, and A. Zeilinger. "Real-time imaging of quantum entanglement". In: *Sci. Rep.* 3 (2013), p. 1914. DOI: 10.1038/srep01914.

[114] P. Johnson and R. Christy. "Optical Constants of the Noble Metals". In: *Phys. Rev. B* 6 (1972), pp. 4370–4379. DOI: 10.1103/PhysRevB.6.4370.

[115] A. Aspuru-Guzik and P. Walther. "Photonic quantum Simulators". In: *Nature Physics* 8 (2012), pp. 285–291. DOI: 10.1038/nphys2253.

[116] W. L. Barnes, A. Dereux, and T. W. Ebbesen. "Surface plasmon subwavelength optics". In: *Nature* 424 (2003), pp. 824 –830. DOI: 10.1038/nature01937.

[117] J. A. Schuller, E. S. Barnard, W. Cai, Y. C. Jun, J. S. White, and M. L. Brongersma. "Plasmonics for extreme light concentration and manipulation". In: *Nature Materials* 9 (2010), p. 193. DOI: 10.1038/nmat2630.

[118] I. De Leon, Z. Shi, A. C. Liapis, and R. W. Boyd. "Measurement of the complex nonlinear optical response of a surface plasmon-polariton". In: *Opt. Lett.* 39.8 (2014), pp. 2274–2277. DOI: 10.1364/OL.39.002274.

[119] J. Homola. "Present and future of surface plasmon resonance biosensors". In: *Analytical and Bioanalytical Chemistry* 377.3 (2003), pp. 528–539. ISSN: 1618-2650. DOI: 10.1007/s00216-003-2101-0.

[120] S. Lal, S. Link, and N. J. Halas. "Nano-optics from sensing to waveguiding". In: *Nature Photonics* 1 (2007), pp. 641–648. DOI: 10.1038/nphoton.2007.223.

[121] M. S. Tame, K. R. McEnery, Ş. K. Özdemir, J. Lee, S. A. Maier, and M. S. Kim. "Quantum plasmonics". In: *Nature Physics* 9 (2013), p. 329. DOI: 10.1038/nphys2615.

[122] A. V. Akimov, A. Mukherjee, C. L. Yu, D. E. Chang, A. S. Zibrov, P. R. Hemmer, H. Park, and M. D. Lukin. “Generation of single optical plasmons in metallic nanowires coupled to quantum dots”. In: *Nature* 450 (2007), p. 402. DOI: `10.1038/nature06230`.

[123] R. Kolesov, B. Grotz, G. Balasubramanian, R. J. Stöhr, A. A. L. Nicolet, P. R. Hemmer, F. Jelezko, and J. Wrachtrup. “Wave–particle duality of single surface plasmon polaritons”. In: *Nature Physics* 5 (2009), p. 470. DOI: `10.1038/nphys1278`.

[124] E. Altewischer, M. P. van Exter, and J. P. Woerdman. “Plasmon-assisted transmission of entangled photons”. In: *Nature* 418 (2002), p. 304. DOI: `10.1038/nature00869`.

[125] D. Pines. *Elementary Excitations in Solids: Lectures on Phonons, Electrons, and Plasmons*. W. A. Benjamin, 1963.

[126] M.-C. Dheur, E. Devaux, T. W. Ebbesen, A. Baron, J.-C. Rodier, J.-P. Hugonin, P. Lalanne, J.-J. Greffet, G. Messin, and F. Marquier. “Single-plasmon interferences”. In: *Science Advances* 2.3 (2016). DOI: `10.1126/sciadv.1501574`.

[127] G. Di Martino, Y. Sonnefraud, M. S. Tame, S. Kéna-Cohen, F. Dieleman, Ş. K. Özdemir, M. S. Kim, and S. A. Maier. “Observation of Quantum Interference in the Plasmonic Hong-Ou-Mandel Effect”. In: *Phys. Rev. Applied* 1 (3 2014), p. 034004. DOI: `10.1103/PhysRevApplied.1.034004`.

[128] B. Vest, M.-C. Dheur, É. Devaux, A. Baron, E. Rousseau, J.-P. Hugonin, J.-J. Greffet, G. Messin, and F. Marquier. “Anti-coalescence of bosons on a lossy beam splitter”. In: *Science* 356.6345 (2017), pp. 1373–1376. ISSN: 0036-8075. DOI: `10.1126/science.aam9353`.

[129] E. P. Wigner. “Lower Limit for the Energy Derivative of the Scattering Phase Shift”. In: *Phys. Rev.* 98 (1 1955), pp. 145–147. DOI: `10.1103/PhysRev.98.145`.

[130] A. Lagendijk and B. A. van Tiggelen. “Resonant multiple scattering of light”. In: *Physics Reports* 270.3 (1996), pp. 143 –215. ISSN: 0370-1573. DOI: `https://doi.org/10.1016/0370-1573(95)00065-8`.

[131] R. Bourgain, J. Pellegrino, S. Jennewein, Y. R. P. Sortais, and A. Browaeys. “Direct measurement of the Wigner time delay for the scattering of light by a single atom”. In: *Opt. Lett.* 38.11 (2013), pp. 1963–1965. DOI: `10.1364/OL.38.001963`.

[132] L. Zhang, A. Kubo, L. Wang, H. Petek, and T. Seideman. “Imaging of surface plasmon polariton fields excited at a nanometer-scale slit”. In: *Phys. Rev. B* 84 (24 2011), p. 245442. DOI: `10.1103/PhysRevB.84.245442`.

[133] C. Lemke, C. Schneider, T. Leißner, D. Bayer, J. W. Radke, A. Fischer, P. Melchior, A. B. Evlyukhin, B. N. Chichkov, C. Reinhardt, M. Bauer, and M. Aeschlimann. “Spatiotemporal Characterization of SPP Pulse Propagation in Two-Dimensional Plasmonic Focusing Devices”. In: *Nano Letters* 13.3 (2013), pp. 1053 –1058. DOI: `10.1021/nl3042849`.

[134] G. Gay, O. Alloschery, B. Viaris de Lesegno, J. Weiner, and H. J. Lezec. “Surface Wave Generation and Propagation on Metallic Subwavelength Structures Measured by Far-Field Interferometry”. In: *Phys. Rev. Lett.* 96 (21 2006), p. 213901. DOI: `10.1103/PhysRevLett.96.213901`.

[135] Henri J. Lezec and Tineke Thio. “Diffracted evanescent wave model for enhanced and suppressed optical transmission through subwavelength hole arrays”. In: *Opt. Express* 12.16 (2004), pp. 3629–3651. DOI: `10.1364/OPEX.`

12.003629. URL: http://www.opticsexpress.org/abstract.cfm?URI=oe-12-16-3629.

[136] J. Weiner. “Phase shifts and interference in surface plasmon polariton waves”. In: *Opt. Express* 16.2 (2008), pp. 950 –956. DOI: 10.1364/OE.16.000950.

[137] O. T. A. Janssen, H. P. Urbach, and G. W. ’t Hooft. “On the phase of plasmons excited by slits in a metal film”. In: *Opt. Express* 14.24 (2006), pp. 11823 –11832. DOI: 10.1364/OE.14.011823.

[138] G. Lévêque, O. J. F. Martin, and J. Weiner. “Transient behavior of surface plasmon polaritons scattered at a subwavelength groove”. In: *Phys. Rev. B* 76 (15 2007), p. 155418. DOI: 10.1103/PhysRevB.76.155418.

[139] A. Klick, S. de la Cruz, C. Lemke, M. Großmann, H. Beyer, J. Fiutowski, H.-G. Rubahn, E. R. Méndez, and M. Bauer. “Amplitude and phase of surface plasmon polaritons excited at a step edge”. In: *Applied Physics B* 122.4 (2016), p. 79. ISSN: 1432-0649. DOI: 10.1007/s00340-016-6350-y.

[140] Matthew S. Davis, Wenqi Zhu, Ting Xu, Jay K. Lee, Henri J. Lezec, and Amit Agrawal. “Aperiodic nanoplasmonic devices for directional colour filtering and sensing”. In: *Nature Communications* 8.1347 (2017), p. 1347. URL: https://doi.org/10.1038/s41467-017-01268-y.

[141] R. P. Feynman, R. B. Leighton, and M. Sands. *The Feynman Lectures on Physics: Volume 3: Quantum Mechanics*. Addison-Wesley, Inc., 1964.

[142] U. Sinha, C. Couteau, T. Jennewein, R. Laflamme, and G. Weihs. “Ruling Out Multi-Order Interference in Quantum Mechanics”. In: *Science* 329.5990 (2010), pp. 418–421. ISSN: 0036-8075. DOI: 10.1126/science.1190545.

[143] A. Sinha, A. H. Vijay, and U. Sinha. "On the superposition principle in interference experiments". In: *Scientific Reports* 5 (2015), p. 10304. DOI: `10.1038/srep10304`.

[144] H. De Raedt, K. Michielsen, and K. Hess. "Analysis of multipath interference in three-slit experiments". In: *Phys. Rev. A* 85 (1 2012), p. 012101. DOI: `10.1103/PhysRevA.85.012101`.

[145] R. Sawant, J. Samuel, A. Sinha, S. Sinha, and U. Sinha. "Nonclassical Paths in Quantum Interference Experiments". In: *Phys. Rev. Lett.* 113 (12 2014), p. 120406. DOI: `10.1103/PhysRevLett.113.120406`.

[146] Y. Gorodetski, K. Y. Bliokh, B. Stein, C. Genet, N. Shitrit, V. Kleiner, E. Hasman, and T. W. Ebbesen. "Weak Measurements of Light Chirality with a Plasmonic Slit". In: *Phys. Rev. Lett.* 109 (1 2012), p. 013901. DOI: `10.1103/PhysRevLett.109.013901`.

[147] C. H. Gan, G. Gbur, and T. D. Visser. "Surface Plasmons Modulate the Spatial Coherence of Light in Young's Interference Experiment". In: *Phys. Rev. Lett.* 98 (4 2007), p. 043908. DOI: `10.1103/PhysRevLett.98.043908`.

[148] N. Kuzmin, G. W. 't Hooft, E. R. Eliel, G. Gbur, H. F. Schouten, and T. D. Visser. "Enhancement of spatial coherence by surface plasmons". In: *Opt. Lett.* 32.5 (2007), pp. 445–447. DOI: `10.1364/OL.32.000445`.

[149] S. Divitt, M. Frimmer, T. D. Visser, and L. Novotny. "Modulation of optical spatial coherence by surface plasmon polaritons". In: *Opt. Lett.* 41.13 (2016), pp. 3094–3097. DOI: `10.1364/OL.41.003094`.

[150] D. Li and D. Pacifici. "Strong amplitude and phase modulation of optical spatial coherence with surface plasmon polaritons". In: *Science Advances* 3.10 (2017). DOI: `10.1126/sciadv.1700133`.

[151] G. Weihs, M. Reck, H. Weinfurter, and A. Zeilinger. “All-fiber three-path Mach-Zehnder interferometer”. In: *Opt. Lett.* 21.4 (1996), pp. 302–304. DOI: 10.1364/OL.21.000302.

[152] M. Żukowski, A. Zeilinger, and M. A. Horne. “Realizable higher-dimensional two-particle entanglements via multiport beam splitters”. In: *Phys. Rev. A* 55 (4 1997), pp. 2564–2579. DOI: 10.1103/PhysRevA.55.2564.

[153] R. Schnabel, A. Bunkowski, O. Burmeister, and K. Danzmann. “Three-port beam splitters-combiners for interferometer applications”. In: *Opt. Lett.* 31.5 (2006), pp. 658–660. DOI: 10.1364/OL.31.000658.

[154] A. J. Menssen, A. E. Jones, B. J. Metcalf, M. C. Tichy, S. Barz, W. S. Kolthammer, and I. A. Walmsley. “Distinguishability and Many-Particle Interference”. In: *Phys. Rev. Lett.* 118 (15 2017), p. 153603. DOI: 10.1103/PhysRevLett.118.153603.

[155] N. Spagnolo, C. Vitelli, L. Aparo, P. Mataloni, F. Sciarrino, A. Crespi, R. Ramponi, and R. Osellame. “Three-photon bosonic coalescence in an integrated tritter”. In: *Nature Communications* 4 (2013), p. 1606. DOI: 10.1038/ncomms2616.

[156] C. Schaeff, R. Polster, M. Huber, S. Ramelow, and A. Zeilinger. “Experimental access to higher-dimensional entangled quantum systems using integrated optics”. In: *Optica* 2.6 (2015), pp. 523–529. DOI: 10.1364/OPTICA.2.000523.

[157] T. Meany, M. Delanty, S. Gross, G. D. Marshall, M. J. Steel, and M. J. Withford. “Non-classical interference in integrated 3D multiports”. In: *Opt. Express* 20.24 (2012), pp. 26895–26905. DOI: 10.1364/OE.20.026895.

[158] Edited by E. D. Palik. *Handbook of Optical Constants of Solids*. Academic Press, Boston, 1985.

[159] S. Ravets, J. C. Rodier, B. Ea Kim, J. P. Hugonin, L. Jacubowiez, and P. Lalanne. "Surface plasmons in the Young slit doublet experiment". In: *J. Opt. Soc. Am. B* 26.12 (2009), B28–B33. DOI: `10.1364/JOSAB.26.000B28`.

[160] S. Mori, K. Hasegawa, T. Segawa, Y. Takahashi, and S. Inoue. "Interference of Photon Emitted by a Slit–Groove Structure after the Conversion of Photon to Surface Plasmons". In: *Japanese Journal of Applied Physics* 48.6R (2009), p. 062001. URL: `http://stacks.iop.org/1347-4065/48/i=6R/a=062001`.

[161] T. Wang, G. Comtet, E. Le Moal, G. Dujardin, A. Drezet, S. Huant, and E. Boer-Duchemin. "Temporal coherence of propagating surface plasmons". In: *Opt. Lett.* 39.23 (2014), pp. 6679–6682. DOI: `10.1364/OL.39.006679`.

[162] P. Lalanne and J. P. Hugonin. "Interaction between optical nano-objects at metallo-dielectric interfaces". In: *Nature Physics* 2 (July 2006), p. 551. DOI: `10.1038/nphys364`. URL: `https://doi.org/10.1038/nphys364`.

[163] Yong-Jun Bao, Ru-Wen Peng, Da-Jun Shu, Mu Wang, Xiang Lu, Jun Shao, Wei Lu, and Nai-Ben Ming. "Role of Interference between Localized and Propagating Surface Waves on the Extraordinary Optical Transmission Through a Subwavelength-Aperture Array". In: *Phys. Rev. Lett.* 101 (8 2008), p. 087401. DOI: `10.1103/PhysRevLett.101.087401`. URL: `https://link.aps.org/doi/10.1103/PhysRevLett.101.087401`.

[164] N. Rotenberg, M. Spasenović, T. L. Krijger, B. le Feber, F. J. García de Abajo, and L. Kuipers. "Plasmon Scattering from Single Subwavelength Holes". In: *Phys. Rev. Lett.* 108 (12 2012), p. 127402. DOI: `10.1103/`

PhysRevLett.108.127402. URL: https://link.aps.org/doi/10.1103/PhysRevLett.108.127402.

[165] Haitao Liu and Philippe Lalanne. “Microscopic theory of the extraordinary optical transmission”. In: *Nature* 452 (2008), p. 728. DOI: 10.1038/nature06762. URL: https://doi.org/10.1038/nature06762.

[166] P. Kuan, C. Huang, W. S. Chan, S. Kosen, and S. Lan. “Large Fizeau’s light-dragging effect in a moving electromagnetically induced transparent medium”. In: *Nature Communications* 7 (2016), p. 13030. DOI: 10.1038/ncomms13030.

[167] R. Thom. “Stabilité structurelle et morphogenèse”. In: *Poetics* 3.2 (1974), pp. 7 –19. ISSN: 0304-422X. DOI: https://doi.org/10.1016/0304-422X(74)90010-2.

[168] V. I. Arnol’d. “Critical points of smooth functions and their normal forms”. In: *Russian Math. Surveys* 30.5 (1975), pp. 1 –75. URL: https://doi.org/10.1070/RM1975v030n05ABEH001521.

[169] F. M. Miatto, A. Safari, and R. W. Boyd. “Explicit formulas for photon number discrimination with on/off detectors”. In: *Appl. Opt.* 57.23 (2018), pp. 6750–6754. DOI: 10.1364/AO.57.006750.

[170] C. Silberhorn. “Detecting quantum light”. In: *Contemporary Physics* 48.3 (2007), pp. 143–156. DOI: 10.1080/00107510701662538.

[171] P. Kok and S. L. Braunstein. “Detection devices in entanglement-based optical state preparation”. In: *Phys. Rev. A* 63 (3 2001), p. 033812. DOI: 10.1103/PhysRevA.63.033812.

[172] A. J. Miller, S. W. Nam, J. M. Martinis, and A. V. Sergienko. "Demonstration of a low-noise near-infrared photon counter with multiphoton discrimination". In: *Applied Physics Letters* 83.4 (2003), pp. 791–793. DOI: 10.1063/1.1596723.

[173] M. Fujiwara and M. Sasaki. "Multiphoton discrimination at telecom wavelength with charge integration photon detector". In: *Applied Physics Letters* 86.11 (2005), p. 111119. DOI: 10.1063/1.1886903.

[174] E. J. Gansen, M. A. Rowe, M. B. Greene, D. Rosenberg, T. E. Harvey, M. Y. Su, R. H. Hadfield, S. W. Nam, and R. P. Mirin. "Photon-number-discriminating detection using a quantum-dot, optically gated, field-effect transistor". In: *Nature Photonics* 1.10 (2007), pp. 585–588. DOI: 10.1038/nphoton.2007.173.

[175] B. E. Kardynal, S. S. Hees, A. J. Shields, C. Nicoll, I. Farrer, and D. A. Ritchie. "Photon number resolving detector based on a quantum dot field effect transistor". In: *Applied physics letters* 90.18 (2007), p. 1114. DOI: 10.1063/1.2735281.

[176] N. Namekata, Y. Takahashi, G. Fujii, D. Fukuda, S. Kurimura, and S. Inoue. "Non-Gaussian operation based on photon subtraction using a photon-number-resolving detector at a telecommunications wavelength". In: *Nature Photonics* 4.9 (2010), pp. 655–660. DOI: 10.1038/nphoton.2010.158.

[177] J. Kim, S. Takeuchi, Y. Yamamoto, and H. H. Hogue. "Multiphoton detection using visible light photon counter". In: *Applied Physics Letters* 74.7 (1999), pp. 902–904. DOI: 10.1063/1.123404.

[178] B. E. Kardynał, Z. L. Yuan, and A. J. Shields. "An avalanche-photodiode-based photon-number-resolving detector". In: *Nature photonics* 2.7 (2008), pp. 425–428. DOI: 10.1038/nphoton.2008.101.

[179] D. Achilles, C. Silberhorn, C. Śliwa, K. Banaszek, and I. A. Walmsley. "Fiber-assisted detection with photon number resolution". In: *Optics letters* 28.23 (2003), pp. 2387–2389. DOI: 10.1364/OL.28.002387.

[180] M. J. Fitch, B. C. Jacobs, T. B. Pittman, and J. D. Franson. "Photon-number resolution using time-multiplexed single-photon detectors". In: *Physical Review A* 68.4 (2003), p. 043814. DOI: 10.1103/PhysRevA.68.043814.

[181] D. Achilles, C. Silberhorn, C. Sliwa, K. Banaszek, I. A. Walmsley, M. J. Fitch, B. C. Jacobs, T. B. Pittman, and J. D. Franson. "Photon-number-resolving detection using time-multiplexing". In: *Journal of Modern Optics* 51.9-10 (2004), pp. 1499–1515.

[182] L. A. Jiang, E. A. Dauler, and J. T. Chang. "Photon-number-resolving detector with 10 bits of resolution". In: *Physical Review A* 75.6 (2007), p. 062325. DOI: 10.1103/PhysRevA.75.062325.

[183] E. Lantz, J.-L. Blanchet, L. Furfaro, and F. Devaux. "Multi-imaging and Bayesian estimation for photon counting with EMCCDs". In: *Monthly Notices of the Royal Astronomical Society* 386.4 (2008), pp. 2262–2270. DOI: 10.1111/j.1365-2966.2008.13200.x.

[184] M. Avenhaus, K. Laiho, M. V. Chekhova, and C. Silberhorn. "Accessing higher order correlations in quantum optical states by time multiplexing". In: *Physical review letters* 104.6 (2010), p. 063602. DOI: 10.1103/PhysRevLett.104.063602.

[185] O. Thomas, Z. .L Yuan, and A. J. Shields. "Practical photon number detection with electric field-modulated silicon avalanche photodiodes". In: *Nature communications* 3 (2012), p. 644. DOI: 10.1038/ncomms1641.

[186] J. Sperling, W. Vogel, and G. S. Agarwal. "True photocounting statistics of multiple on-off detectors". In: *Phys. Rev. A* 85 (2 2012), p. 023820. DOI: `10.1103/PhysRevA.85.023820`.

[187] R. H. Hadfield. "Single-photon detectors for optical quantum information applications". In: *Nature Photonics* 3.12 (2009), pp. 696–705. DOI: `10.1038/nphoton.2009.230`.

[188] X. Gu, W. Mohammed, L. Qian, and P. W. E. Smith. "All-Fiber Laser Beam Shaping Using a Long-Period Grating". In: *IEEE Photonics Technology Letters* 20.13 (2008), pp. 1130–1132. ISSN: 1041-1135. DOI: `10.1109/LPT.2008.924640`.

[189] S. M. Barnett and P. M. Radmore. *Methods in Theoretical Quantum Optics*. Oxford University Press, 2002.

[190] A. M. Pérez, P. R. Sharapova, S. S. Straupe, F. M. Miatto, O. V. Tikhonova, G. Leuchs, and M. V. Chekhova. "Projective filtering of the fundamental eigenmode from spatially multimode radiation". In: *Phys. Rev. A* 92 (5 2015), p. 053861. DOI: `10.1103/PhysRevA.92.053861`.